Gold Nanostars For Cancer Molecular Imaging and Therapy

By

Yu-Chuan Ou

Dissertation

Submitted to the Faculty of the

Graduate School of Vanderbilt Engineering

in partial fulfillment of the requirements

for the degree of

DOCTOR OF PHILOSOPHY

in

Chemical Engineering

May 10, 2019

Nashville, Tennessee

Approved:

Rizia Bardhan, Ph.D.

Leon M. Bellan, Ph.D.

Ethan S. Lippmann, Ph.D.

Matthew J. Lang, Ph.D.

John T. Wilson, Ph.D.

To my mother, for her courage to beat cancer twice. Thank you for your never-ending unconditional love and support. You have taught me what perseverance truly means.

ACKNOWLEDGEMENT

The last five years at Vanderbilt have been an amazing and exciting period of growth and I owe my success to the support of countless people. I would like to express my deepest appreciation to my PhD advisor, Dr. Rizia Bardhan for her mentorship and guidance in my professional and personal development. She has always advocated for her students and provided unparalleled help and guidance. I would also like to thank the other members of my committee Dr. Matthew Lang, Dr. John Wilson, Dr. Ethan Lippmann, and Dr. Leon Bellon for their continued support over the years of my dissertation projects. Their unique sets of expertise guided my ever-evolving projects and ultimately led to the completion of this dissertation.

I would like to thank my previous and current labmates. Dr. Holly Zarick, Dr. Will Erwin, Dr. Naiya Soetan, Dr. Joseph Webb, Eric Talbert, and Xiaona Wen who have all been amazing friends to me and provided tremendous guidance to my career. It has been a great honor to work with them in the same lab.

I am also thankful for my collaborators, Dr. Dan Shae, Dr. Christine O'Brien, Dr. Oscar Ayala, Dr. Isaac Pence, Dr. Shannon Faley, Dr. Eugene Lin, Dr. Singh Bhuminder, Dr. Noor Tantawy, Dr. Michael Nickels, Dr. Anita Mahadevan-Jansen, Dr. Anna Vilgelm, Dr. Marjan Rafat, Dr. Rossane Delapp, Dr. Kelli Boyd, Andrew Johnson, Jen Bateman, and Galina Bogatcheva for providing the expertise and training to move my projects forward. They each provided vital supporting work and brainstorming help throughout my Ph.D. career at Vanderbilt. In addition, I would like to thank Vanderbilt University Institute of Imaging Science (VUIIS), VUMC Translational Pathology Shared Resources (TPSR), VU Cell Imaging Shared Resources (CISR), and Vanderbilt Institute of Nanoscale Science and Engineering (VINSE) for help on my projects.

I am deeply grateful for all the friendships I have made during my time living in Nashville - Mengya Li, Anna Douglas, Rachel Carter, Chris Reynold, Chiachi Liao, Lisa Lin, Tony Wu, BT Lin, Emma Hollmann, Ali Pereira, Sonia Brady, Nikki Reinemann, Krysta Waldrop, and Becca Creed along with many others in the Vanderbilt ChBE department and community for their friendship and support. I am also deeply thankful for my friends outside of Nashville- Ming Liang, Lily Chiu, Elly Liou, Shannon Chen, Amanda Wang, Wendy Chen, Shiori Ito, Michelle Makiro, and Cherry Wang.

I am also very thankful to have the best dog in the world. Pickle has brought so much joy, warmth, and laughter to my life. He is my companion for life. I am very lucky to be his pawmom.

Finally, I would like to express my most sincere and deepest appreciation to my parents and my brother, Ben, who have always been there for me. Their unconditional love and support have allowed me to become the person I have always aspired to be.

TABLE OF CONTENTS

Page

LIST OF TABLES

Table Page

LIST OF FIGURES

Chapter 1

INTRODUCTION

1.1 Motivation

According to the World Health Organization (WHO), cancer has been the second leading cause of death globally for many years. The idea of a "magic bullet" to deliver therapeutic agents to a targeted site was first introduced by Paul Ehrlilch more than a century ago.[1] Inspired by his ideas, countless different drug delivery platforms have been explored to transform anti-cancer treatment, starting an era of nanoparticle-mediated drug delivery and imaging. One of the most well-known nanorugs is Doxorubicin HCl liposomal formula, Doxil, which was first approved by the FDA in 1999 to treat ovarian cancer. Clinical results have shown improved drug bioavailability and a decrease in cardiotoxicity. Nanoparticle albumin-bound paclitaxel, Abraxane, a therapeutic that can decrease immunotoxicity was approved in 2005. Following these initial successes, a second generation of nanoparticles, polymeric nanoparticles, and a third generation, inorganic nanoparticles were then engineered for cancer therapy and contrast imaging. For example, FDA-approved ultra-small superparamagnetic iron oxide (USPIO) nanoparticles are currently used for magmatic resonance imaging (MRI).[2] However, few FDA-approved nanomedicine product are currently used in standard clinical settings despite all the progress that has been made.

Among the many nanoparticles that are being investigated, gold nanoparticles have shown tremendous promise. In fact, silica-gold nanoshells coated with polyethylene glycol (PEG) (AuroLase) are currently under clinical trials to thermally ablate prostate, head and neck, and lung cancers.[3] Gold nanoparticles are inert nanomaterials that are non-toxic. Their surface can be easily modified with polymers to provide biocompatibility or active targeting entities to target tumor cells. Moreover, the optical characteristics, size, and shape of gold nanoparticles can be easily

tuned for desired application. The plasmonic property of gold nanoparticles can be utilized for light-to-heat conversion (photothermal therapy) and surface enhanced Raman scattering (SERS). Overall, gold nanoparticles provide endless opportunities to be exploited for cancer therapy and imaging.

Cancer is an evolving and complex disease. A single modality of treatment is generally not sufficient to achieve remission-free outcome. Thus, we are inspired to combine gold nanoparticle mediated hyperthermia/photothermal therapy with a second therapy modality for synergistic therapeutic effects. These gold nanoparticles can also be utilized as an imaging contrast agent. Cancer immunotherapy has shown recent success, but also face limitations. To address these challenges, we are motivated to design a gold nanoparticle based molecular imaging platform to provide information for accurate immunotherapy patient selection. In addition, the ease of surface conjugation of gold nanoparticles allows us to further engineer gold particles for multimodal imaging by utilizing imaging techniques that complement one another.

1.2 Hallmarks of Cancer

Cancer is an extremely complex neoplastic disease that despite devoted effort and research, remains one of the leading causes of death in most developed countries. Many targeted therapies have been developed to specifically tackle each hallmark capability of cancer. The idea of hallmarks of cancer was first proposed in 2000 by Hanahan and Weinberg and the hallmarks provide a logical framework for understanding of the progression of normal cells to a neoplastic state. As more shared traits between different cancers were discovered, Hanahan and Weinberg added four additional hallmarks to rationalize the progression of such complex disease (Figure 1.1).[4]

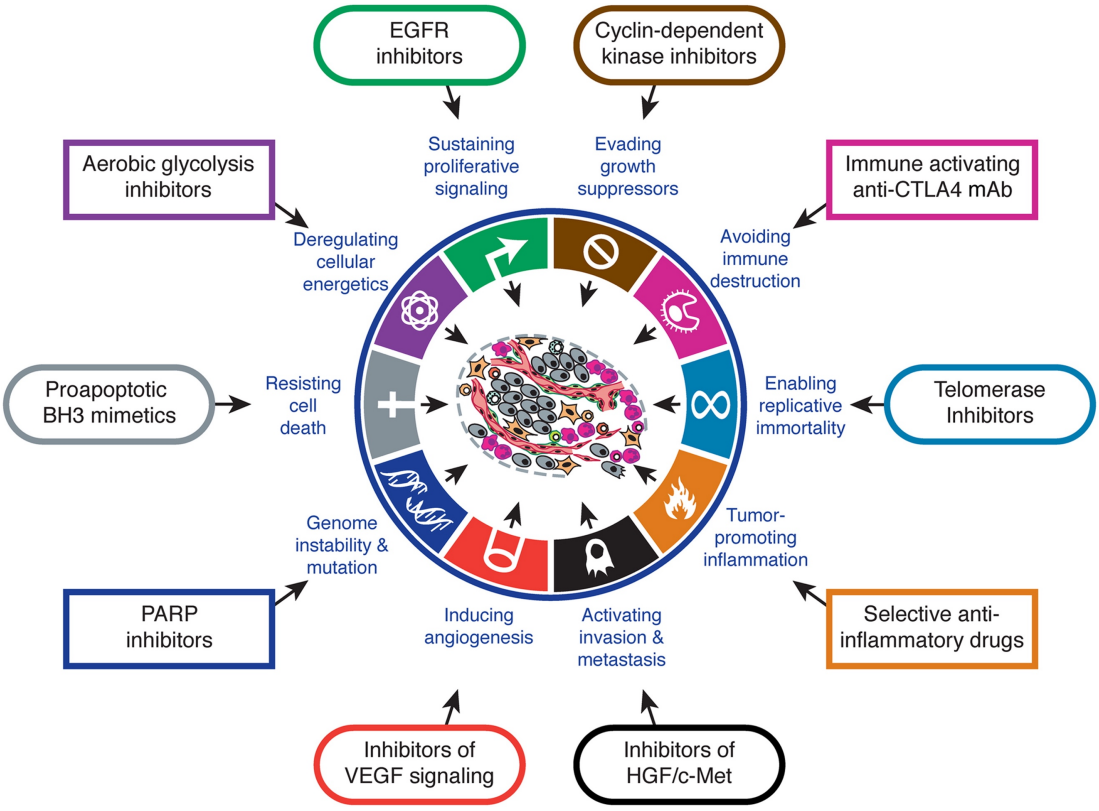

Figure 1.1 Ten hallmark capabilities of cancer in order evolve and progress to a complex neoplastic disease. Targeted therapies have been developed to interfere each acquired hallmark (examples are shown in the figure). Image produced from Hanahan *et al.*[4] with permission from the Cell publish group.

The first hallmark of cancer is *sustaining proliferative signaling*. As normal cells carefully control the production and release of growth-promoting signals to maintain homeostasis, cancer cells generally deregulate such signals to increase both cell size and rate of cell division. Cancer cells also go through somatic mutation to activate additional downstream pathways that constitutively activate growth factor receptors.[5] Next, cancer cells acquire the ability to *evade growth suppressors* that negatively regulate cell proliferation. Tumor suppressor genes that are involved in decisions between cell growth or cell death (activation of senescence or apoptosis) are generally dysfunctional or lost in many cancers. Tumorous cells are also capable of *resisting cell death* by altering damage sensors that lead to apoptosis. P53 is one of the most important tumor

suppressor genes that initiates repair mechanism when DNA is damaged and chromosomes abnormalities are detected. P53 also controls and arrest cell cycle and when necessary, induce apoptosis. This "guardian of the genome" is either mutated or completely lost in half of human cancers.[6] Further, cancer cells acquire *replicative immortality* through expressing a significant level of telomerase. The function of this specialized DNA polymerase is to add telomere segments to the ends of DNA, allowing unlimited cycles of growth-and-division. To supply enough nutrients and oxygen to the tumor microenvironment to facilitate rapid growth, tumor-associated neovasulatures are generated. Tumor cells *induce angiogenesis* often by upregulate angiogenesis inducers, vascular endothelial growth factor-A (VEGF-A) or downregulating inhibitor, thrombospondin-1 (TSP-1). The last hallmark of cancer of the original six is *activating invasion and metastasis*. The ability for cancer cells to invade local tissues and achieve distant metastasis is supported by "epithelial-mesenchymal transition" (EMT) and the degradation of the extracellular matrix (ECM). After initial invasion, metastatic dissemination of cancer cells is achieved by the reverse process, "mesenchymal-epithelial transition" (MET), allowing formation of new colonies.

In 2011, Hanahan and Weinberg added the following four hallmarks, *genome instability and mutation, tumor-promoting inflammation, deregulating cellular energetics, and evading immune responses* to the original six. Genome instability and mutation describes the defective DNA/chromosome maintenance and repair mechanism of cancer cells in order to accumulate favorable genotypes that are advantageous for tumor progression. Next, tumor cells are found to transition their metabolism pathway largely to glycolysis (aerobic glycolysis). Cancer cells also can promote favorable inflammation and evade immune responses to orchestra a growth-promoting tumor microenvironment (TME). Tumor-associated macrophages have found to

facilitate tumor growth, angiogenesis and ECM degradation. Tumor cells also over-expressed immune checkpoint receptors, CTLA-4 and PD-L1 that inhibit T cell activation.

Research and understanding of cancer progression provide a valuable tool box for engineers to rationalize more efficient cancer therapeutics and design imaging/detection platforms that can provide further insight to tumor progression and treatment responses of the disease. In this PhD. dissertation, nanomaterial, gold nanostars, are utilized to improve anti-cancer therapeutic outcomes and to image cancer cells at the molecular level.

1.3 Plasmonic Nanoparticles

1.3.1 Fundamentals of Plasmonics

Localized surface plasmon resonance, or LSPR is the collective oscillation of the conductive electron cloud upon light stimulation. LSPR can generate strong electromagnetic enhancement. Following light absorption, the plasmon energy must decay through a series of relaxation events and eventually release the energy as either light scattering (radiative relaxation) or heat transfer (non-radiative relaxation) to its surroundings. By modulating the size of gold nanoparticles (AuNPs) the relative contribution of radiative and non-radiative decay to the total extinction can be controlled. Smaller nanoparticles ($\leq$40 nm) mainly absorb light while larger nanoparticles (t$\geq$80) predominately scatter light. But in complexed anisotropic nanostructures, geometry generally contributes to the absorption and scattering properties of particles rather than overall size. High scattering nanoparticles are an excellent contrast agent for optical imaging and sensing. Plasmonic nanoparticles with high polarizability and large scattering cross-section can significantly enhance Raman scattering of molecules. Surface-enhanced Raman scattering (SERS) based imaging platforms have been widely studied in preclinical setting for various biological applications (see more details in

chapter 1.5.3). For biological applications, the plasmon resonance of gold nanostructures are often designed and tuned to the near-infrared (NIR) region, or "biological window" (680–900 nm) of light, where both protein scattering and water absorption are minimized. As a result, deep tissue light penetration can be achieved for both imaging and treatment purposes without damaging tissues.[7]

As the size of AuNPs increase, a corresponding increase in the LSPR is observed due to phase retardation effects. Red-shift in plasmon resonance is attributed to the increase in plasmon lifetime and a decrease in wave frequency, which inversely increases the wavelength of the plasmon. LPSR wavelength can also be altered by changing the geometry of gold nanostructures. For example, by increasing the number of arms/protrusions of gold nanostars, a significant red-shift in the plasmon resonances can be achieved. Additionally, assembling more than one gold nanoparticles (dimer, trimer or higher order) red-shifts LPSR due to plasmon hybridization models. Formation of gold nanoparticle clusters, whether ordered or disordered results in intense electromagnetic fields, also known as "hot-spots" within the junctions of interacting gold nanoparticles in the vicinity. The hot spots substantially enhance SERS and the light-to-heat conversion ability of gold nanoparticles, enabling sensitive detection and effective treatment of cancer.[8-9]

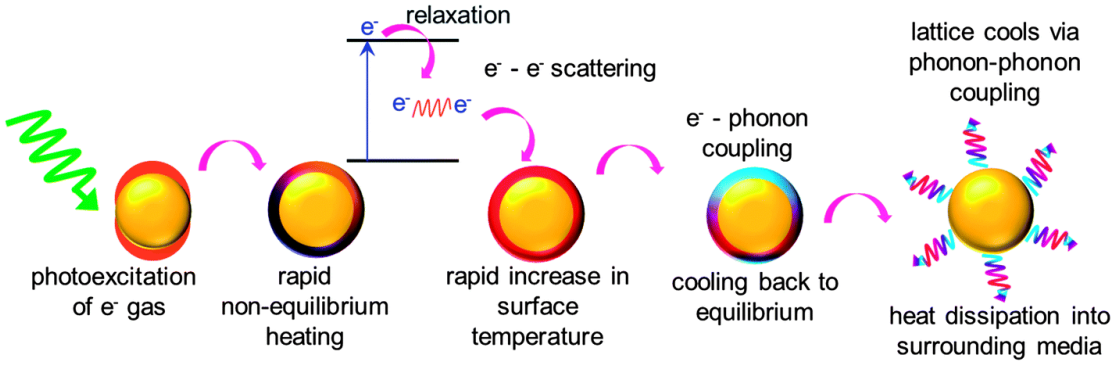

Figure 1.2 Schematic describing the mechanism of light to heat conversation by plasmonic nanostructures. Image produced from Webb *et al.*[10] with permission from the Royal Society of Chemistry publishing group.

In addition to radiative decay, strong electromagnetic fields generated from plasmon can also relax nonradiatively, which can be harvested for light-to-heat conversion to induce photothermal therapy to treat various diseases. To understand the fundamentals of the photothermal process, Ultrafast dynamics systems were used as many events happen in femto-seconds to picoseconds. Rapid and non-equilibrium heating first occurs as the plasmonic nanostructures are excited with resonant photons (Figure 1.2). The initial intense plasmon energy is first relaxed through electron-electron scattering, generating a rapid increase in the surface temperature of the metal. The heat then cools off to equilibrium by transferring the energy from the hot electrons to the lattice phonons (electron-phonon relaxation). Eventually, the lattice cools off via phonon-phonon coupling and the resulting heat is transferred to the surrounding medium. The heat dissipated from gold nanoparticles is then harnessed to ablate cancer cells.[11]

1.3.2 Biological Applications

Gold nanoparticles (AuNPs) are inert and non-toxic nanomaterials that have tremendous therapeutic potential in cancer detection and treatment. AuNPs shape and size are both tunable for desired applications by adjusting the facile synthesis method, making them versatile in theraputic and imaging applications. Bioconjugations of AuNPs surface can be achieved though thiol-gold and amine-gold interactions. Various designs of AuNPs have been developed to improve the limits of cancer detection and therapeutic outcomes of cancer treatments.

AuNPs have been engineered as contrast agents for different clinical and pre-clinical imaging techniques. First, AuNPs were used extensively for emission enhancement of fluorophores for both one-photon and two-photon fluorescence imaging. FDA-approved near-infrared fluorophores, indocyanine green (ICG) was incorporated with gold nanoshells for *in vivo* imaging in breast cancer tumors.[12] AuNPs also exhibit high x-ray attenuation, allowing better

contrast for both x-ray imaging and Computed Tomography (CT). Compared to traditional iodine-based or barium sulfate-based CT contrast molecules, AuNPs have longer vascular retention time, which increase available imaging windows.[13] Meir *et al.* designed 20 nm gold nanoparticles conjugated with anti-PD-L1antibodies (αPDL1-GNPs) for CT imaging of tumors and detection of immune checkpoint receptors.[14] Cancer specific T cells were also labelled with gold nanoparticles for longitudinal CT imaging and quantitative tracking of T cell migration and accumulation in tumors.[15] Positron emission tomography (PET) imaging requires the use of radioactive isotopes. Due to their small size, radiolabeles experience rapid renal clearance and uptake by the mononuclear phagocytes system (liver and spleen), resulting in short plasma half time. Radiolabelling AuNPs allowed the PET contrast agent to remain longer in the bloodstream to achieve time course imaging up to several days. Several studies have shown time-course *in vivo* PET imaging with ^{64}Cu labelled gold nanoparticles to image tumor xenograft.[16-17] AuNPs incorporated with positron-emitting radionuclides have recently been studied to label both T cells and dendritic cells (DC) for immuno-PET imaging.[18-19] Gold nanoparticles can also enhance contrast for dark field confocal imaging, optical coherence tomography (OCT), and photoacoustic imaging. In addition, the strong electromagnetic field generated from gold nanoparticles can be harvested to enhance Raman scattering for surface enhanced Raman spectroscopy (SERS).

AuNPs are also widely used in cancer therapy for drug and gene delivery, or to ablate tumor directly using heat. Photothermal therapy with gold nanoshells is currently under FDA trials to treat prostate cancer. Gold nanoshell-mediated *in vivo* PTT in glioma tumor models demonstrated a 3-month survival rate in mice compared to a 3-week survival rate of control mice.[20] Shao et al. designed gold nanospheres coated with thermosensitizing cytokine, tumor necrosis factor-alpha (TNF alpha) for PTT in mice bearing mammary tumor cells. Complete tumor regression was

achieved 9 days after treatment and no visible tumor mass was observable after 2 weeks.[21] AuNPs have also been investigated to deliver drugs such as oxaliplatin to lung cancer by 30 nm AuNP or doxorubicin in mesoporous silica encapsulated gold nanoraods.[22-23] Therapeutic oligonucleotides (siRNA , shRNA, pDNA and ssDNA) generally undergo fast intracellular degradation and rapid uptake by lysozymes. Lee *et al.* designed multicomponent AuNPs that can facilitate cellular uptake and endosomal escape to deliver siRNA.[24] Overall AuNPs have shown promising capability for both cancer therapeutics and imaging/detection.

1.3.3 Gold Nanostars

While the optical resonance of simple isotropic shaped nanostructures can be easily manipulated through size, the resonances for anistropic nanostrucutres are functions of their geometry. By tuning the morphologies of complex anistropic nanostrucutures, the optical characteristics can be designed and controlled to achieved desired properties. The plasma resonance of branched nanoparticles such as gold nanostars are easily tunable by modulating the length and density of protrusion without relying on overall dimension. Gold nanostars have spherical cores that function as efficient antennas. The absorbed incident light by the cores can then be routed to the protrusions, intensifying at the tips of each branch and directing to different directions. This intense nanoantenna effect results in strong electronmagnetic near-fields at the end of sharp protrusions which can be utilized for both surface enhanced spectroscopies and photothermal applications.[25]

The synthesis process of gold nanostars is a straightforward one-step approach without the need of using gold seed precursors. Biological buffer, HEPES (4-(2-hydroxyethyl)-1-piperazineethanesulfonic acid) acts as both capping and reducing agent. HESPS-mediated gold nanostar fabrication has several advantages. First, the length of protrusions on gold nanostars can

be easily manipulated by changing the HEPES concentration during the synthesis process. Therefore, geometry-dependent optical properties of gold nanostars can be altered to achieve a desired goal. Second, without the need of gold seed precursors, the synthesis process of gold nanstars can be easily scaled up. Lastly, gold nanostars synthesized in HEPES buffer have shown high biocompatibly. The surface of gold nanostars allows bioconjugation without the need for tedious ligand or solvent exchange.

Gold nanostars are promising nanomaterials for both cancer imaging and therapy. The plasmon resonance of gold nanostars can be adapted to the near-infrared region of light without increasing their overall size. Gold nanostars have excellent photothermal ability that can be utilized for both direct tumor ablation using heat and controlled drug delivery. Gold nanostars can generate strong EM field and "hot spots" that can enhance Raman scattering to several orders of magnitude, which allows sensitive detection for both in vivo studies and biosensing applications.

1.4 Nanoparticles for Cancer Medicine

1.4.1 Hyperthermia and Photothermal Therapy in Cancer

Hyperthermia which exposes a targeted area (local, regional or whole body) to approximately 42 °C has been shown to facilitate chemotherapy drug delivery, radiation therapy and immunotherapy in clinical trials (Figure 1.3). Methods used to deliver the heat included the use of high-intensity focused ultrasound, radiofrequency ablation, regional perfusion, and isolation perfusion. Hyperthermia can also be achieved through photothermal therapy with plasmonic nanostructures and near-infrared laser. The use of nanostructures and light activation can deliver heat to the tumor microenvironment without harming healthy tissues.

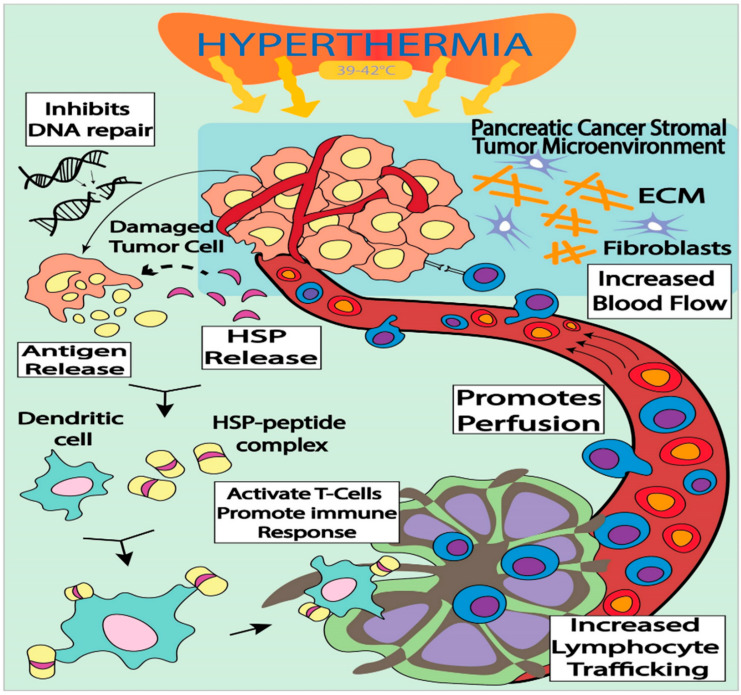

Figure 1.3 Hyperthermia and its impact in cancer therapy. Image produced from Mahmood *et al.*[26] with permission from the MDPI publishing group.

Hyperthermia can influence physical properties of cell membranes, especially their permeability and fluidity. Hyperthermia can block DNA and RNA synthesis by influencing DNA polymerase and ligation enzymes. The heat can also cause damage to lysosomal membranes and result in autolysis of the cell. Hyperthermia, combined with anti-cancer drugs has demonstrated synergistic effects. Adriamycin, bleomycin, carboplatin, mitomycin C, fluorouracil, and cisplatin have all been evaluated in conjunction with hyperthermia and the combination of the two have shown better outcomes than a drug-only approach. Hyperthermia can enhance chemotherapy drug uptake, improve cellular membrane permeability, and alter physiological behavior of cells, making them more susceptible to apoptosis. Furthermore, hyperthermia can amplify enhanced permeability and retention (EPR) effects by increasing blood flow and pore size of tumor vasculatures even in impermeable vessels.[27-29] Hyperthermia combined with radiotherapy has demonstrated better outcomes for breast, head and neck, cervical, and esophagus cancer.[30]

Hypothermia acts as sensitizer of tumor ablation through ionizing radiation (IR). Since heat can alter protein structure and folding, the treatment can be used to influence DNA damage responses.[31]

Recently, hyperthermia combined with radiotherapy has shown to alter tumor immunity by activating both innate and adoptive immune responses. Local irradiation in association with mild hyperthermia results in upregulation of heat shock protein (HSP70). HSPs are stress proteins that play an important role in folding/unfolding, sorting and transporting of proteins, singling pathways and protection of cells against stress. HSPs can influence and modulate tumor immunogenicity by inducing Major Histocompatibility Complex (MHC) class I expression and acting as inflammatory signals that facilitate the production of cytokines. HSPs can also activate antigen-presenting cells, such as dendritic cells by delivery HSPs-peptide complex. As a result, hyperthermia is now being studied to aid immunotherapies.[32-33] Liu et al. has shown to successfully induce long-lasting immunity against unresectable and metastatic cancer by combining photothermal therapy and checkpoint blockage therapy (anti-PD-L1 therapy).[34]

1.4.2 Low Temperature Sensitive Liposomes

Drug encapsulated Low Temperature Sensitive Liposomes (LTSLs) have gained interest from researchers due to their clinically relevant phase transition temperature (T_m) at 41.7 $^{\circ}$C. T_m is defined as the temperature required for the well-packed and fully extended hydrocarbon chains to transform to a non-ordered liquid crystalline phase. When the hydrophobic tails of the phospholipids become randomly oriented, the drug contents inside the liposomes can diffuse freely out of the bilayer membrane. T_m of LTSLs is only a few degrees higher than the human body temperature (5 $^{\circ}$C). Thus, LTSLs have been used as temperature-activated drug carriers. Doxorubicin (DOX), a widely used chemotherapy drug, has been demonstrated as a model drug

in many LTSLs delivery studies. LTSLs has demonstrated superior drug delivery capability. Studies have shown a LTSLs delivery system results in 25 times great tumor drug concentration than using free drug dispersal, and 5 times greater than traditional non-thermal sensitive liposomes.[35] These promising results are attributed to the intravascular release of small molecule drug, which can accumulate in tumor mass simply through diffusion. Doxorubicin-encapsulated LTSLs (ThermoDOX) combined with local mild hyperthermia is currently undergoing phase III clinical trials.[36]

1.5 Raman Spectroscopy

1.5.1 Basics of Raman Spectroscopy

Raman scattering is the inelastic scattering of photons from chemical or biological samples. The excitation of photons to the virtual energy state can relax and result in either a loss (stoke) or gain (anti-stocke) of energy that occurs from the interaction between light and *the* vibrational modes of the chemical bonds of polarizable molecules. Measuring the shift in energy or Raman scatterinsg reveals the vibration phenomonon, which further reveals different vibrational, bending and streching modes of the molecule. Detecting Raman scattereing provides information such as chemical composition and strctural conformation of molecules. As a result, Raman spectroscopy was first introduced as material identification and analysis tool.

Recently, Raman spectroscopy has been used in variety of biological applications through either label-free, or labeled Raman. NIR lasers, either at 785 nm or 1064 nm are commonly utilized for biological samples to minimize biological fluoresence background. A typical Raman study can accumulate a large number of spectra data sets, which makes extracting useful data challenging.

As a result, multivariate analysis approaches (principle component analysis, k-mean clustering etc) is generally required to effectively rationalized the obtained data.

1.5.2 Surface Enhanced Raman Scattering (SERS)

Raman spectroscopy has been widely investigated for biological sample detection and *in vivo* biomedical applications. However, Raman scattering is a rare phenomenon that occurs only ~ 1 in 10 million scattered photos, thus it is quite weak compared to Rayleigh scattering. To further enhance Raman scattering, and improve signal-to-noise and spectral resolution, surface enhanced Raman scattering is introduced. Samples are usually placed on or in the vicinity of plasmonic nanoparticles or substrates, where the enhancement occur. Gold and silver nanostructures are commonly used as SERS substrate since they do not have intrinsic Raman active modes.

Two common theories have been proposed to explain surface enhanced Raman scattering, electromagnetic (EM) enhancement and chemical enhancement. EM enhancement is the dominant effect of SERS, where the enhancement can be in the order of 10^8–10^{12}. EM occurs when incident light polarizes the electron of plasmonic nanoparticles, their localized surface plasmon resonance then generates a strong EM field and excites the molecule of interest. The strength of induced dipole is a function of both the incident electric field strength and the polarizability of the SERS nanostructure. Next, the emitted Raman scattering of the molecule of interest is further enhanced by the localized electric field of the gold nanoparticles. Chemical Enhancement involves a charge transfer mechanism between the SERS substrate and detecting molecule. Chemical Enhancement contributes to SERS at a lower extent with an enactment factor in the order of 10^3–10^5.

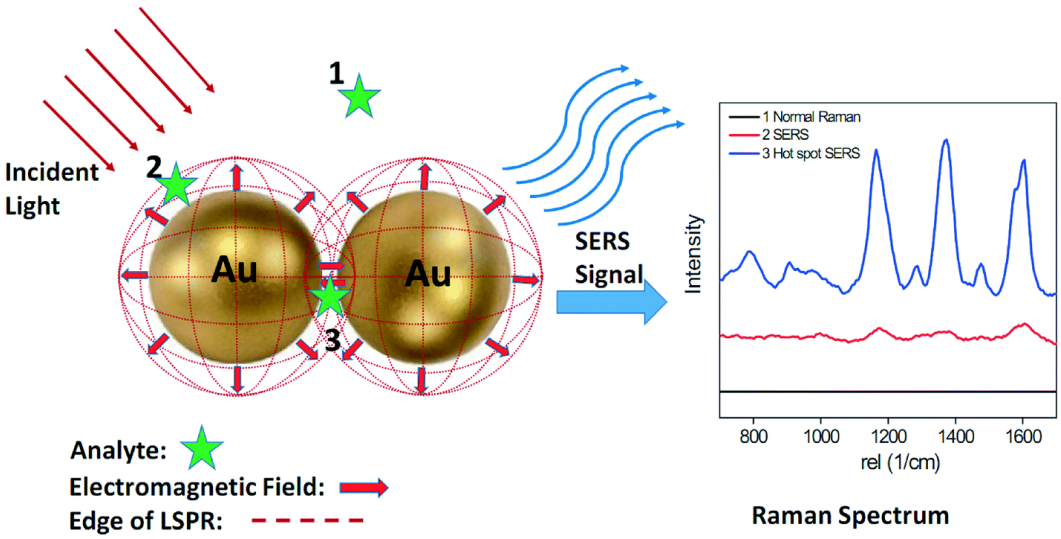

Figure 1.4 Surface enhanced Raman Scattering (SERS) with electron hot spots to further enhance Raman intensity. Figure adopted from Wei *et al.* with permission from the Royal Society of Chemistry publishing group.[37]

Anisotropic nanostructures such as gold nanostars with sharp tips have shown high sensitivities and strong SERS capability. Multiple pointed tips can generate junctions with neighboring nanostars, providing electron hot spots that result in ultra-strong near-field (Figure 1.4). The resulting enhancement can be utilized for SERS detection in cells, tissues and *in vivo* animal studies (see Chapter 3 and 4).

1.5.3 SERS in Biological Application

SERS for biological and medical applications is achieved through either label-free detection, or indirect approaches by applying SERS tags. Label-free detection can be used to detect biomolecules through direct interaction between the SERS substrate and the target of interest. Thus, intrinsic biological fingerprints of the samples can be obtained with enhanced intensity. For labelled-SERS, the bare nanostructures are generally conjugated with Raman reporters, coated with a layer of polymer for biocompatibility and stability. SERS nanostructures can also be further functionalized with targeting entities such as antibodies, peptides or aptamers. The Raman reporter

molecules usually have strong and distinct Raman peaks, which are further enhanced by plasmonic nanostructures. As a result, ultra-sensitive *in vivo* imaging, SERS-based diagnostic/detection, or sensing of biological samples can be achieved. SERS has been utilized for multiplexed detection of more than one target due to the narrow bandwidth of Raman peaks, which minimizes cross-talks between Raman tags.

SERS has been studied extensively for detection, identification and investigation of biological processes at the cellular level. Xie *et al*. incubated common food pathogens with gold colloids for rapid and sensitive (10^{14} to 10^{15} enhancement factor) label-free SERS detection. They employed cluster analysis (principal component analysis, PCA) and dendrogram construction (hierarchical cluster analysis, HCA) to classify bacteria.[38] Jiang *et al.* grew cells on silver nanoparticles-decorated silicon wafers to observe apoptosis at single cell resolution by performing SERS mapping.[39] Gold nanoparticles modified with pH sensitive Raman tag, 4-MPy (4-mercaptopyridine) were used to detect extracellular pH (pHe) of cells. Xu and coworkers showed the capability of SERS imaging to monitor live cell pHe changes due to apoptosis.[40] Similarly, a SERS-based technique was also designed for carbon monoxide (CO) sensing by observing the reaction of palladacycle carboxylation of gold nanoparticles.[41] SERS or Raman imaging in live cell and at single cell resolution is of great value as one can observe the real-time dynamic of cellular processes upon external stimulation.[42]

In vivo SERS detection has been applied to various applications and has shown tremendous potential as a pre-clinical imaging technique. Nima *et al.* constructed silver-gold nanorod hybrids that were modified with four different Raman-active molecules and their corresponding four breast cancer-specific antibodies to detect circulating tumor cells (CTC). The concentration of CTC in blood is extremely low, but with SERS detection, individual breast cancers cells in unprocessed blood can be

identified with high specificity (a single cell within 7 million of blood cells).[43] Another *in vivo* example utilizes SERS and hand-held Raman spectroscopy to delineate tumor margins during real time tumor resection surgery. By using gold–silica SERS nanoparticles, image-guided, near real-time craniotomy surgery on brain tumors was performed at high precision.[44] Ovarian tumors were also identified using folate receptor targeting SERS gold nanoparticles combined with Raman spectroscopy and bioluminescence imaging (BLI). Whole abdomen imaging was first acquired with BLI then regions of interest were scanned with Raman spectroscopy. The multimodal imaging platform is extremely sensitive; as a result, tumor as small as 370 μm can still be detected.[44]

In this dissertation, labelled-SERS with gold nanostars is exploited for multiplexed Raman imaging to detect both cancer specific biomarker, epidermal growth factor receptor (EGFR), and checkpoint receptor, programmed death-ligand 1 (PD-L1) (Chapter 3). SERS is then combined with a second imaging modality, positron emission tomography (PET) to achieve 3-dimeensional, sensitive, quantified, and time-resolved detection of both PD-L1 and CD8+ T cells in melanoma tumors.

1.6 Molecular Imaging

1.6.1 Cancer Biomarkers and Immuno-imaging

Immunotherapies including checkpoint blockage therapy, adoptive cell therapy, and cancer vaccines have recently driven a paradigm shift in the treatment in a broad array of cancers. Immune checkpoints are essential for the maintenance of self-tolerance and protection of healthy tissue from inflammatory responses during pathogenic infection. The expression of immune-checkpoint proteins is upregulated by many kinds of tumors to evade immune surveillance. Checkpoint blockage therapy has been utilized in melanoma, lymphoma, ovarian cancers and more.

T cell based immunotherapy has shown tremendous results in clinical trials to combat cancer and prevent metastasis. Dendritic Cells (DC) are antigen presenting cells that activate the body's adoptive immune system. Successful DC vaccines have been shown to increase tumor infiltrating T cells within a tumor and induce an immunologic response, which improves overall survival outcome.[45] However, despite the clinical benefits of these approaches, only a fraction of patients respond to these treatments across most tumor types and identifying patients likely to benefit from these therapies remains challenging. Moreover, treatment optimization can be difficult partly due to the lack of real time imaging techniques to track the migration of T cells and DC. Therefore, immuno-imaging is critical to the immunotherapy drug development pipeline to select patients who will respond to immunotherapies even before treatment begins, to monitor treatment response and to reflect the dynamic changes in immuno-markers localization during therapeutic intervention.

1.6.2 Multimodal Imaging

This dissertation focuses on diagnoses and detection of biomarkers/immuno-markers for patient selection for immune checkpoint blockage therapy. Tumor heterogeneity is one of the biggest challenges in combating cancer. Among individuals, even with the same kind of cancer, tumor pathology and the biomarkers present on the tumors may vary significantly. The causes of cancer, age, gender, individual metabolisms, and genetic history can all give rise to the heterogeneity of tumors. As a result, the same anti-cancer therapy might have different levels of therapeutic outcomes among different patients. For oncologists to provide the most suitable treatments, understanding a specific cancer case at the molecular level (i.e. cancer specific receptors and biomarkers) is the first step to providing proper therapy. The diagnostic information obtained from cancer molecular imaging can greatly improve both the prognosis of the disease and

the positive responses of the treatments (Figure 1.5). Here, two imaging modalities that complement one another are introduced for cancer multimodal molecular imaging.

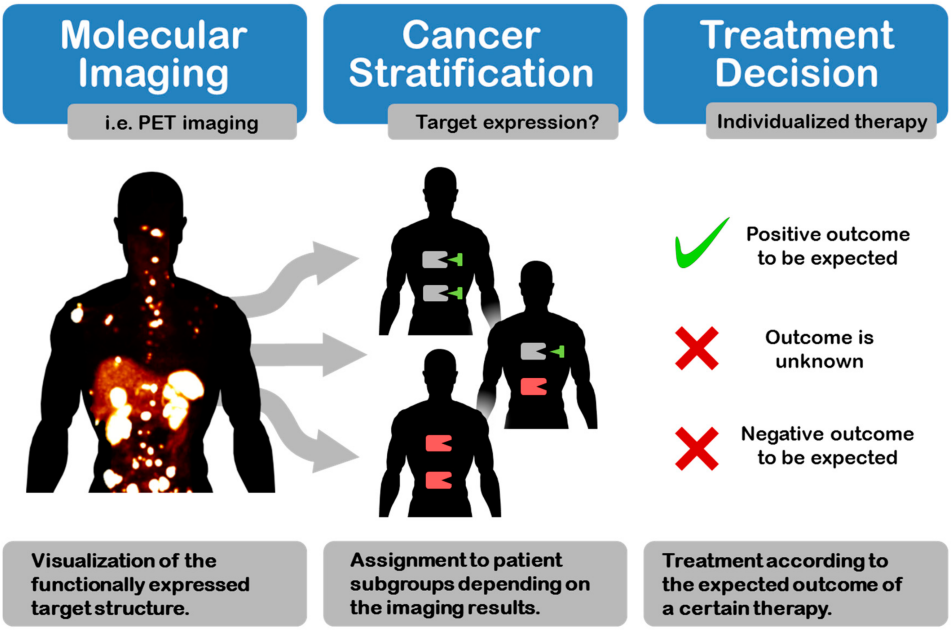

Figure 1.5 Molecular imaging of cancer specific biomarkers for cancer treatment patient stratification. Imaged adopted from Webar et al. with permission from MDPI publishing group.[46]

The first imaging modality is surface enhanced Raman spectroscopy mediated with functionalized, active-targeting gold nanostars. SERS provides spatial and temporal resolution and allows multiplexed detection with more than one biomarker. However, the penetration depth of SERS is limited and the sensitivity of the signals may not be up to the clinical standards. To overcome these shortcomings, a second imaging technique can be synergistically combined with SERS molecular imaging. Comparing different imaging methods that are currently used in clinical settings, we found that positron emission tomography (PET) in combination with SERS imaging can provide the most sensitive, accurate, and informative diagnostic results (Table 1.1, red box).

Table 1.1 Characteristics of standard imaging methods for diagnosis of biomarkers of cancer. MRI: magnetic resonance imaging. BI: bioluminescence imaging. Fluorescence (FL). OCT: optical coherence tomography. PET: positron emission tomography

Technique	3D	Spatial Resolution	Temporal Resolution	Sensitivity	Deep Tissue Imaging	Multiplexing
MRI	X	X			X	
BI			X	X	X	
FL			X	X		
OCT	X			X		
PET	**X**			**X**	**X**	
Raman		**X**	**X**			**X**

PET is a nuclear medicine technique that has been widely used in clinical settings to detect and stage cancer, evaluate brain abnormalities, and in cardiology to observe the perfusion to the myocardium. Various positron emitting radionuclides have been tailored to optimize PET contrast, although approximately 90 percent of PET imaging in the U.S. utilize flurodeoxyglucose (F-18 FDG) to observe metabolism processes. PET has already demonstrated its high sensitivity, wide field of view, and the capability of whole-body 3D imaging in clinical settings.[47] Therefore, combining the strengths of both techniques, integrated PET/Raman is ideal for cancer molecular imaging.

1.7 Organization of Dissertation

This dissertation contains 5 main chapters.

Chapter 2 demonstrates the synergistic therapeutic effects of photothermal hyperthermia of gold nanostars with drug delivery from low temperature sensitive liposomes (LTSLs). This combination therapy can successfully induce cell death in aggressive breast cancer cells with

higher efficacy than free drug delivery by providing a controlled light-activated approach and minimal off-target toxicities.

Chapter 3 evaluates the use of gold nanostars conjugated with Raman tags for multiplexed surface enhanced Raman spectroscopy (SERS) and simultaneous diagnosis of programmed death-ligand 1(PD-L1) and epidermal growth factor receptor (EGFR). Longitudinal SERS showed high sensitivity and specificity of the platform to detect both PD-L1 and EGFR levels in breast tumor. Furthermore, *ex-vivo* Raman maps provided assessment of biomarker status with cellular-resolution.

Chapter 4 utilizes gold nanostars for multimodal imaging platform to simultaneously detect PD-L1 on melanoma tumor cells and CD8 on T cells. By combining positron emission tomography (PET) with SERS using gold nanostars, quantitative, sensitive, and depth-resolved whole-body imaging can be achieved. Furthermore, responses to immunotherapy can be monitored by AuNS-mediated PET/SERS imaging to track changes in PD-L1 and CD8 levels.

Chapter 5 explores the use of Raman spectroscopy to monitor metabolic changes in breast cancer cells treated with small molecular inhibitors.

Chapter 2

DESIGN, SYNTHESIS, CHARACTERIZATION OF GOLD NANOSTARS FOR CANCER THERAPEUTICS

Adopted from: Ou, Y. C.; Webb, J. A.; Faley, S.; Shae, D.; Talbert, E. M.; Lin, S.; Cutright, C. C.; Wilson, J. T.; Bellan, L. M.; Bardhan, R., Gold nanoantenna-mediated photothermal drug delivery from thermosensitive liposomes in breast cancer. ACS Omega 2016, 1 (2), 234-243 *with permission from the American Chemical Society.*

2.1 Summary

In this work, we demonstrate controlled drug delivery from low temperature sensitive liposomes (LTSLs) mediated by photothermal heating from gold nanostars (AuNS) in triple negative breast cancer cells *in vitro*. The unique geometry of AuNS enables the generation of mild hyperthermia (~42 °C) by converting near-infrared light to heat and effectively deliver doxorubicin (DOX) from LTSLs in breast cancer cells. We confirmed cellular uptake of AuNS by both fluorescence confocal Z-stack imaging and TEM imaging. We performed cellular viability assay, and live/dead cell fluorescence imaging of the combined therapeutic effects of AuNS with DOX-loaded LTSLs, and compared them with free DOX, and DOX-loaded non-temperature sensitive liposomes (NTSLs). Imaging of fluorescent live/dead cell indicators and MTT assay outcomes both demonstrated significant decreases in cellular viability when cells were treated with the combination therapy. Due to the high phase transition temperature of NTSLs, no drug delivery was observed from DOX-loaded NTSLs. Notably, even at low DOX concentration of 0.5 μg/ml, the combination treatment resulted in a higher (33 %) cell death, relative to free DOX (17% cell death). The results of our work demonstrate that the synergistic therapeutic effect of photothermal hyperthermia of AuNS with drug delivery from LTSLs can successfully treat aggressive breast

cancer cells with higher efficacy than free DOX by providing a controlled light-activated approach and minimum off-target toxicities.

2.2 Introduction

Nanostructures have been used as carriers for transporting cargo where drug delivery is controlled endogenously by biological cues, such as pH or ions,[48-51] or exogenously by plasmonic photothermal materials with near-infrared light-triggered release. Plasmonic gold nanostructure-mediated drug delivery has been extensively studied in the past decade to combat cancer and other inflammatory diseases.[22, 52-57] There are several advantages to exploiting the light-to-heat conversion abilities of gold nanostructures for exogenous control of drug delivery. First, by tuning the laser flux density and nanostructure concentration, the light-triggered approach generates mild hyperthermia (40–43 °C) that is sufficient for drug release with minimal damage to healthy tissue.[58-60] Second, light activation enables controlled drug delivery at the tumor site while minimizing off-target toxicity. Third, photothermal hyperthermia is highly localized and non-invasive, thus eliminating the need for whole-body heating or invasive heating probes used in current clinical hyperthermia. Finally, hyperthermia improves both vascular permeability and increases blood perfusion in the hypoxic tumor areas, enhancing drug uptake and therapeutic efficacy.[27-29] For example, plasmonic nanostructures have been combined with thermo-responsive polymers for controlled delivery.[61-62] In this work, we demonstrate the use of Gold nanostars (AuNS) as photothermal actuators to induce delivery of the anticancer drug doxorubicin (DOX) from low-temperature sensitive liposomes. The intense photothermal properties of AuNS are attributed to their unique geometry where the spherical core behaves as an antenna absorbing near-infrared light, and the protrusions act as emitters localizing the absorbed light at the tips, thus

efficiently converting light to heat.[25, 63] The 50–60 nm size of AuNS is ideal for these studies enabling rapid endocytosis and accumulation in cells.[64-67] Further, their straightforward synthesis in aqueous media with a non-toxic ligand, 2-[4-(2-hydroxyethyl) piperazin-1-yl]ethanesulfonic acid, HEPES, improves their biocompatibility for cancer treatments.

Low-temperature sensitive liposomes (LTSLs), currently under phase III clinical trial (Thermodox, Celsion Inc.), are ideal drug delivery vehicles due to their low phase transition temperature, T_m, of ~41.7 °C.[68-69] This enables drug release at mild hyperthermia, minimizing unnecessary heating of healthy tissues. Their size can be controlled to ~100 nm, which favors particle accumulation in the tumor microenvironment through the enhanced permeability and retention (EPR) effect.[65, 70] Further, they have high drug loading efficiency and minimal drug leakage at physiological temperature, which can reduce the toxic side effects of chemotherapy.[71-72] LTSLs have been shown to deliver 25 times more DOX into tumors than IV infusion of unencapsulated DOX, and 5 times more DOX than Doxil (commercial non-thermal sensitive liposomal formulation of DOX).[68] For enhanced utility of LTSLs, improved hyperthermia strategies that are noninvasive and administer heat uniformly throughout the cancerous tissue are necessary. However, current clinical approaches to induce local hyperthermia can be invasive, some require a heating probe directly in contact with solid tumors (e.g. radiofrequency ablation), or can give rise to heterogeneous tumor temperatures (e.g. ultrasonic energy) resulting in unpredictable drug release and toxicity to healthy tissues.[73-76]

Here we demonstrate that AUNS-mediated photothermal heating triggered by near-infrared light enables DOX delivery from LTSLs with high efficiency. Co-delivering liposomes and AuNS has several advantages over encapsulating AuNS within the liposomes. First co-delivery allows loading a higher amount of drug within the liposomes. Second, by co-delivering

the size of liposomes can be controlled to ~100 nm increasing their accumulation in cancer cells. Third, co-delivery also enables more nanostructures to localize in cells for enhanced photothermal transduction and drug delivery from liposomes. Finally, nanostructures encapsulation in liposomes is typically achieved by random mixing of the two components which often results in unsuccessful encapsulation and compromises the overall functionality of the hybrid structure. Therefore, by co-delivering AuNS and LTSLs, we observe AuNS-mediated release of DOX from LTSLs far surpasses that from non-thermal sensitive liposomes (NTSLs) under similar conditions because the phase transition temperature of NTSLs is above the clinically relevant hyperthermia range (40–43 °C). Furthermore, our work shows the combination treatment of AuNS-mediated photothermal hyperthermia with LTSLs-delivered chemotherapy has a higher therapeutic efficacy in triple negative breast cancer (TNBC) than with free DOX or photothermal therapy with AuNS alone. TNBC is highly aggressive and is known to develop multidrug resistance (MDR), limiting the successful usage of many chemotherapy drugs, including DOX.[77-79] Photothermal hyperthermia has been shown to reverse resistance to several anticancer drugs,[80-81] which is particularly useful as MDR cells do not exhibit cross-resistance to hyperthermia.[82-84] We envision that a combination treatment with LTSLs and plasmonic nanostructures will ultimately provide a clinically relevant platform for noninvasive drug delivery to TNBC.

2.3 Materials and Methods

2.3.1 Synthesis of PEG-AuNS

All reagents were purchased from Sigma-Aldrich except methoxy- polyethlyene glycol-thiol (mPEG-SH, M_w 5000, JenKem Technology). AuNS were synthesized through the one-step HEPES mediated growth method.[25] First, 18 ml of Milli-Q water (18 MΩ) was added to 12 ml 270

mM HEPES (pH 7.40 ± 0.2). Next, 300 µl of 20 mM chloroauric acid ($HAuCl_4$) was then mixed with the HEPES solution through gentle inversion and left to react at room temperature for 75 minutes. To PEGylate the AuNS, 3 ml of 50 µM mPEG-SH was added to AuNS and reacted at 4 ^{0}C for 24 hours.[85-86] After the reaction, the AuNS solution was centrifuged at 6000 rpm for 20 minutes while discarding the supernatant and resuspending the pellet in 2 ml of Milli-Q water. To ensure complete surface PEGylation, a second addition of mPEG-SH was performed (100 µl of 5 µM mPPEG-SH) for 10 minutes with constant stirring. Lastly, the PEG-coated AuNS were washed with Milli-Q water twice to remove excess chemicals.

2.3.2 Characterization and Photothermal Ability of PEG-coated AuNS

PEG-coated AuNS were imaged with an Osiris transmission electron microscope (TEM) at 200 keV to evaluate their size and morphology. Absorbance properties of AuNS and PEG-coated AuNS were characterized with a Varian Cary 5000 UV-Vis NIR spectrophotometer. A Malvern Nano ZS dynamic light scattering apparatus was used to measure the zeta potential of AuNS before and after PEGylation.

Laser optics used for this project were all purchased from Thorlabs. The optics included an 808 nm laser diode (L808P1WJ), a current controller (LDC240C), a thermoelectric controller (TEDC300C), a collimating lens (C230TME-B), and a silver polished mirror (PF-10-03-P01). Calipers and a power meter (Thorlabs, PM100D) were used to measure the laser spot size and power density. PEG-AuNS at four different concentrations, 80, 110, 140 and 170 µg/ml, were mixed with complete cellular media, Dulbecco's Modified Eagle's medium (DMEM, Gibco) supplemented with 10% fetal bovine serum (FBS, ATCC). The solution was preheated to 37^0 C, added to a 35 mm cell culture dish, and illuminated with the laser at 4, 5.5 and 7 W/cm^2 for 20 minutes. In order to mimic the biological environment, the temperature was kept constant by using

a temperature controller and a heating mantle. Culture dishes with PEG-coated AuNS suspensions were placed on top of an aluminum block wrapped with anti-reflecting black films and a heating mantle. The temperature of the solution was monitored using an infrared camera (FLIR T400) taking images incrementally over time.

2.3.3 Synthesis and Characterization of Doxorubicin-loaded Liposomes

All lipids, dipalmitoylphosphatidylcholine (DPPC), 1-stearoyl-2-hydroxy-*sn*-glycero-3-phosphocholine (MSPC), 1,2-distearoyl-*sn*-glycero-3-phosphoethanolamine-N-[methoxy(polyethylene glycol)-2000] (DSPE-PEG2000), cholesterol and hydrogenated-L-α-phosphatidylcholine (HSPC), were purchased from Avanti Polar Lipid. Doxorubincin hydrochloride was purchased from Fisher Scientific.

LTSLs and NTSLs were synthesized by a reverse-phase evaporation method [87-89]. Briefly, 5 mg of lipid (for LTSLs: DPPC:MSPC:DSPE-PEG2000 = 90:10:4; NTSLs = HSPC:CHOL:DSPE-PEG2000 = 75:50:3 in molar ratio)[90-93] was dissolved in 1 ml of chloroform, then dried by nitrogen air and subsequent vacuum. To form the liposomes, the lipid film was hydrated with 300 mM citrate buffer (pH 4.0) for 60 minutes (at 55 ^{0}C for LTSLs and 60 ^{0}C for NTSLs). Liposomes were then extruded 10 times through a 400 nm and a 100 nm polycarbonate membrane to obtain the desired size. The outside pH of liposome solution was titrated to pH 7.5 by 0.5 M sodium carbonate. As a result, a pH gradient was generated across the lipid bilayer[94-96]. DOX was then added to the liposome solution at a 1:20 DOX:lipid weight ratio and mixed for 60 minutes (at 37 ^{0}C for LTSLs and 60 ^{0}C for NTSLs). The final product was passed through a PD10 column to remove excess DOX. A Malvern Nano ZS dynamic light scattering was used to measure the hydrodynamic size of DOX-LTSLs and DOX-NTSLs. The encapsulation efficiency (EE) of

DOX was monitored at 480 nm by UV-vis spectroscopy.[97] Triton X-100 (2% wt/v) was added to DOX-loaded LTSLs and NTSLs solution to fully lyse the liposomes.

2.3.4 Temperature-triggered DOX Release Measurement

DOX release from LTSLs and NTSLs was monitored at three different temperatures, 37, 42 and 45 ^{0}C. First, 0.9 ml of 25 mM HEPES buffer saline (HBS) was pre-warmed in an incubator to the above listed temperatures. At time zero, 100 µl of DOX-LTSLs or DOX-NTSLs was then added into the HBS and incubated for a given time point. De-quenching of DOX fluorescence was monitored at 480 nm by using a UV-Vis spectrophotometer.[97] Cumulative drug release was calculated by,

$$\%\ Cumulative\ DOX\ Release = \frac{A_t - A_0}{A_\infty - A_0}$$

where A_t, A_0, A_∞ are the absorbances at a given time point, at time zero, or when the liposomes were fully lysed with Triton X-100 respectively.

2.3.5 Cellular Internalization and Localization of PEG-coated AuNS

Alexa Fluor 647 NHS Ester conjugate (ThermoFisher Scientific) was attached to PEG-coated AuNS through OPSS-PEG-amine (JenKem Technology) linker which creates a covalent amide bond between the NHS ester and amine. Alexa Fluor was mixed with OPSS-PEG-amine linker in 3:1 molar ratio at room temperature for 2 hours. The product was then added to AuNS solution and reacted at 4 ^{0}C for 3 hours. An additional mPEG-SH layer was then added to the fluorophore-conjugated AuNS for further stability. The final product was centrifuged at 4000 rpm for 10 minutes. Alexa-conjugated AuNS were added to cells and incubated for 24 hours. Calcein was used to stain live cells. Z-stack images were taken at both time zero (when the AuNS were

just added to cells) and after 24 hours of AuNS incubation. A Zeiss LSM 710 confocal microscope was used for the imaging.

For transmission electron microscope imaging, MDA-MB-231 cells were incubated with PEG-coated AuNS for 24 hours. Cells were then washed with buffer, fixed in 2.5% gluteraldehyde in 0.1M cacodylate buffer at room temperature for 1 hour and 4°C overnight. Samples were processed and imaged in the Vanderbilt Cell Imaging Shared Resource-Research Electron Microscope facility. The cell samples were post-fixed in 1% osmium tetraoxide at room temperature, then washed with 0.1M cacodylate buffer 3 times. Following fixation, the samples were dehydrated through a graded ethanol series followed by incubation in 100% ethanol and propylene oxide (PO) and 2 exchanges of pure PO. Lastly, samples were embedded in epoxy resin and polymerized at 60°C for 48 hours. To obtain thin sections of the sample, 70-80 nm ultra-thin sections were cut from the block and collected on copper grids. The copper grids were stained with 2% uranyl acetate and with lead citrate. Samples were imaged on the Philips/FEI Tecnai T12 electron microscope at different magnifications.

2.3.6 In vitro Temperature-Triggered Release of DOX

MDA-MB-231 cells were purchased from ATCC (HTB-26) and cultured in DMEM supplemented with 10% FBS and 1% penicillin/streptomycin. Cells were maintained at 37 ^{0}C and 5% CO_2. 48 hours prior to the experiments, 330,000 cells were seeded on a 35 mm cell culture dish. On the day of the experiment, fresh media containing DOX-LTSLs, DOX-NTSLs or DOX at 2 μg DOX/ml was then added to the cells. Cells were either incubated at 37 ^{0}C, or 42 ^{0}C for 15 minutes. After 12 hours, the media was changed to fresh cDMEM and cultured for an additional 18 hours. Cells were stained with calcein (5 μM) and propidium iodide (PI, 1 μM) for 20 minutes. A Zeiss LSM 710 confocal microscope was used for fluorescent imaging of the cells.

2.3.7 In vitro Photothermal Drug Delivery and Fluorescence Imaging

MDA-MB-231 cells were passaged for at least 14 days before seeding for the experiment. Approximately, 11,000 cells per well were seeded on a 96 well plate and allowed to adhere and grow. After 48 hours, 65 µl of PEG-coated AuNS (170 µg/ml) in DMEM were added to cells and incubated at 37 ^{0}C for 24 hours. The media was then removed and the cells were washed with cDMEM twice. A Zeiss Observer Z1 microscope was used to visualize cellular uptake of PEG-coated AuNS.

To show DOX release by LTSLs or NTSLs (Figure 4 results), 24 hr after AuNS incubation DOX-LTSLs at 2 µg/ml were added to the cells. Cells were then allowed an hour to equilibrate. An hour later, an 808 nm laser was applied to the cells and illuminated at 5.5 ± 0.1 w/cm^2 for 15 minutes with a laser spot size of approximately 3.5 mm^2. An infrared camera was used to monitor the temperature changes during laser irradiation. The culture media was removed 3 hours post laser treatment and washed with phosphate-buffered saline twice. This process removed any AuNS + LTSLs (or AuNS + NTSLs) from the cells but DOX that was already released from LTSLs (or NTSLs) remained internalized in cells. The cells were then stained with Hoechst and imaged with a confocal microscope.

For *in vitro* photothermal therapeutic study (Figure 5 and 6), a similar procedure was followed as stated above. However, the culture media was changed to fresh cDMEM 12 hours after laser irradiation instead of 3 hours after laser treatment. The cells were left undisturbed (with the fresh media) for an additional 18 hours. So, after a total of 30 hours post laser treatment, cells were stained with calcein and PI and imaged using the confocal microscope to evaluate cellular viability qualitatively. For apoptosis study, Annexin V, Pacific Blue (ThermoFisher Scinetific) at 25 ul/100 ul was used to stain cells 16 hours post laser treatment.

2.3.8 Cellular Viability Assay

MDA-MB-231 cells were passaged and seeded identically on 96 well plates as stated previously. Cells were incubated with 170 μg/ml PEG-coated AuNS for 24 hours and washed with cell medium twice. DOX-LTSLs or DOX-NTSLs at DOX concentrations of 0.5, 2 or 20 μg/ml were then added to the cells. An 808 nm laser at 5.5 W/cm^2 was applied for 15 minutes. The drug was removed, and the culture media was refreshed after 12 hours of laser irradiation. After an additional 18 hours of incubation (30 hours total), old media was removed and replaced with 100 μl of fresh media mixed with 10 μl of 12 mM 3-(4,5-dimethylthiazol-2-yl)-2,5-diphenyltetrazolium bromide (MTT, ThermoFisher Scientific) solution. After 2 hours of MTT incubation, 85 μl of media was removed and 50 μl of DMSO was added to solubilize and dissolve the formazan. A Biotek Synergy H1 plate reader was used to read the absorbance at 540 nm.

2.3.9 Statistical Analysis

All data are presented as mean ± standard deviation. Student's t tests were performed to evaluate the statistical differences. Statistical significance is considered when $p < 0.05$.

2.4 Results and Discussion

We synthesized AuNS by following our previously described procedure using a one-step seedless growth mechanism.[25] In this synthesis, the gold precursor Au^{3+} is reduced in the presence of HEPES, which plays the role of both a reducing and capping agent. HEPES is a widely used biological buffer that promotes the overall biocompatibility of AuNS. The weak adsorption of HEPES along the <111> planes enables kinetically driven protrusion growth along that direction, where the core-to-protrusion ratio is controlled by [HEPES]. By using 270 mM HEPES, the size of AuNS (tip-to-tip distance) was controlled to 56 ± 4 nm (Figure 2.1a), which is ideal for

therapeutic applications. This size regime tunes the plasmon resonance of AuNS to the near-infrared biological window (700–980 nm) where deep tissue penetration can be achieved with incident light.[98] AuNS have 3 distinct plasmon resonances (Figure 2.1b): a bonding plasmon mode at 800 nm, an antibonding plasmon mode at 550 nm, and a shoulder peak at 1100 nm. The antibonding mode is primarily contributed by the core plasmons while the bonding plasmon resonance is predominantly composed of AuNS protrusions, but with a finite contribution of the core plasmons.[25, 99] The shoulder peak arises from the hybridization of the plasmons of multiple protrusions of a AuNS.[100] The AuNS were further coated with polyethylene glycol (PEG) to enhance biocompatibility, reduce cytotoxicity, and provide steric stabilization.[101-105] Successful PEG coating was confirmed by detecting a clear 10 nm shift in the plasmon resonance (Figure 2.1b) due to the higher refractive index of PEG relative to water. A decrease in the surface charge of AuNS is also indicative of successful PEG coating. The surface charge of AuNS before coating was -35.3 mV, which was reduced to -2.9 mV after PEG coating. A near-neutral surface charge on nanoparticles is desirable to reduce non-specific binding of AuNS to cell surface.[64, 106-109]

The light-to-heat conversion ability of AuNS was studied to evaluate their photothermal efficiency, and efficacy in drug delivery from LTSLs. The photothermal behavior of AuNS in cellular media was evaluated at four different concentrations (80, 110, 140, and 170 μg/ml) by illuminating with an 808 nm laser at 5.5 W/cm^2 (Figure 2.1c) and measuring media temperature over time with a thermal camera. With 170 μg/ml of PEG coated AuNS, the temperature within the laser spot reached 57 °C within a minute of illumination. Varying the laser flux (4, 5.5, and 7 W/cm^2) revealed a linear relationship between photothermal temperature and AuNS concentrations (Figure 2.1d). The light to heat conversion by AuNS is initiated by electronic excitation of AuNS followed by relaxation which gives rise to rapid non-equilibrium heating of

the metal. This is followed by cooling to equilibrium during which heat is dissipated from AuNS into the surrounding medium. This dissipated heat is then harnessed by LTSLs enabling efficient drug delivery.[10]

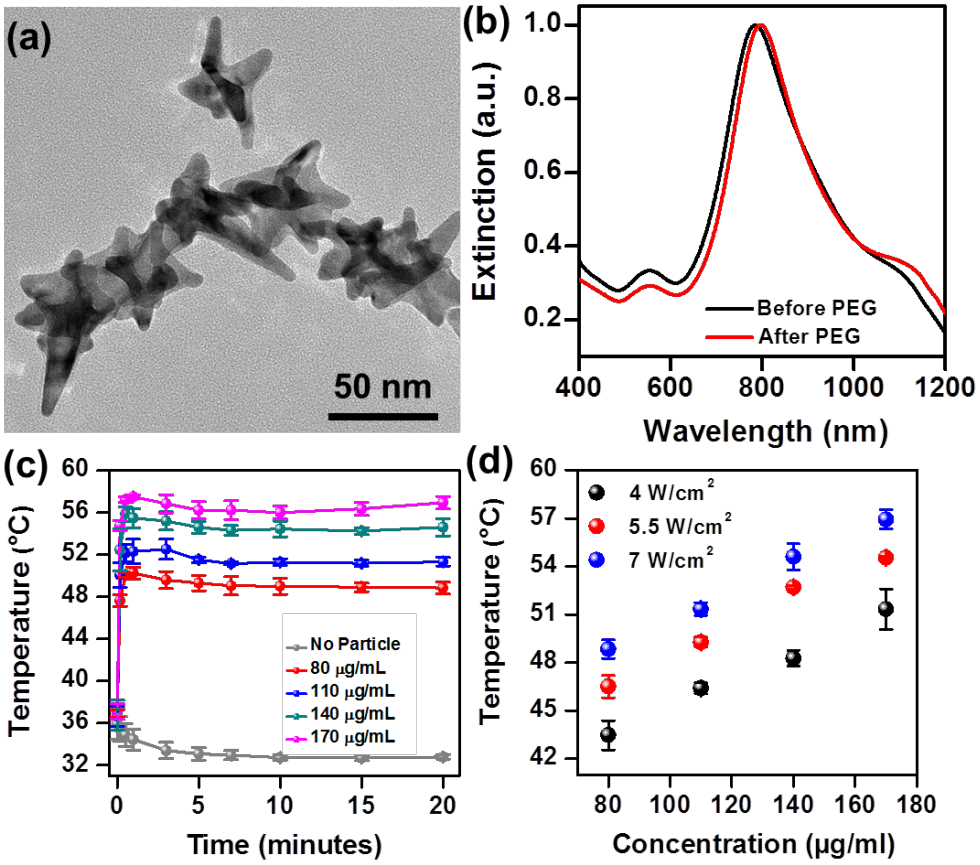

Figure 2.1 Characterization of PEG-coated AuNS. (a) TEM micrograph of AuNS. (b) Extinction spectra of AuNS before and after coating with PEG showing near-infrared resonance. Photothermal characteristics of PEG-coated AuNS showing (c) Temperature at the laser illumination spot at 5.5 W/cm^2 achieved by varying concentrations of PEG-coated AuNS. (d) The photothermal steady state temperature of PEG-coated AuNS after 10 minutes of laser irradiation at 4, 5.5, and 7 W/cm^2 at varying concentrations showing photothermal tunability with particle density and laser flux.

The photothermal ability of AuNS was exploited to enable light-activated drug release from LTSLs with a phase transition temperature (T_m) of ~41.7 °C. We synthesized LTSLs following a previously described procedure[87-89] by mixing the lipids DPPC:MSPC:DSPE-PEG2000 at 90:10:4 ratio in chloroform.[90, 92] The desired size of 110.1± 6.5 nm (Figure A. 2.1a)

of LTSLs was achieved by reverse-phase evaporation and subsequent extrusion. At the T_m of the LTSLs, the fully extended hydrocarbon chains of the lipids transform into a disordered liquid crystalline phase enabling drugs to diffuse through the bilayer membrane.[69] To evaluate the drug release ability of LTSLs, DOX was loaded into the LTSLs using the well-established pH gradient method.[94-96] This approach resulted in ~98 % DOX encapsulation efficiency within the LTSLs. Rapid release of DOX from LTSLs (within 5 min) with a 90% efficiency was achieved at a mild hyperthermia temperature of 42 °C (Figure 2.2a). At higher temperature, 45 °C, >97 % of DOX was released from LTSLs in less than 5 minutes. The long-term stability of DOX-loaded LTSLs (DOX-LTSLs) at 37 °C was also evaluated for 12 hours (Figure A. 2.2a). DOX Leakage studies showed <5 % of DOX escaped from LTSLs at 37 °C, demonstrating very low cytotoxicity of LTSLs at physiological temperature (Figure 2.2a). Highly efficient and rapid drug release from LTSLs with mild hyperthermia enhances the bioavailability of chemotherapy drug in cancer cells with minimal damage to healthy cells. We also compared the efficacy of LTSLs with the traditional non-temperature sensitive liposomal DOX formulation, NTSLs. NTSLs were synthesized by mixing the lipids HSPC:CHOL:DSPE-PEG2000 in a molar ratio of 75:50:3 and achieved a hydrodynamic diameter of 152.7 ± 0.7 nm (Figure A. 2.1b).[91, 93] DOX was loaded in NTSLs similar to the procedure followed for LTSLs. DOX release studies were performed, demonstrating <10% release at all three temperatures, 37 °C, 42 °C, and 45 °C (Figure 2.2b). In additional, long-term stability of DOX-loaded NTSLs (DOX-NTSLs) also shows minimal DOX leakage from NTSLs (Figure A. 2.2b).

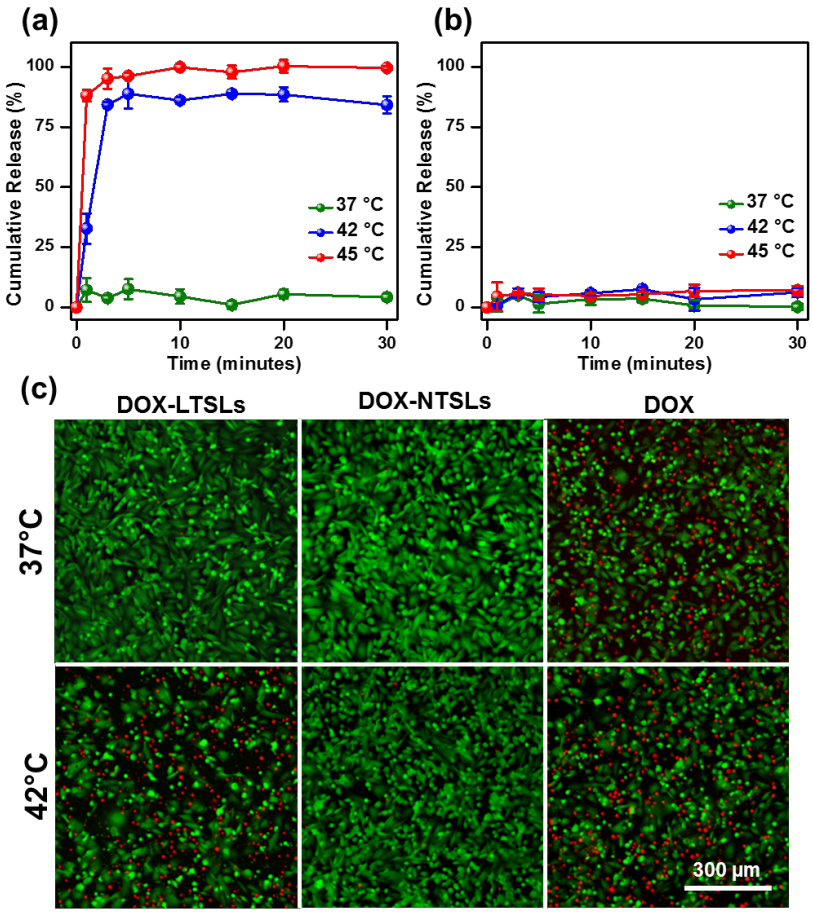

Figure 2.2 Cumulative release of doxorubicin, DOX, at 37 °C, 42 °C, and 45 °C for (a) DOX-LTSLs, and (b) DOX-NTSLs. (c) Confocal images of MDA-MB-231 breast cancer cells incubated with DOX-LTSLs (left panel), DOX-NTSLs (middle panel) and free DOX (right panel) at 2 µg DOX/ml. The cancer cells were incubated at 37 °C and 42 °C for 15 minutes and cellular viability was assessed 30 hours after treatment. Cells were stained with calcein (live cells, green) and propidium iodide (dead cells, red).

The therapeutic ability of LTSLs in controlled drug release was evaluated in MDA-MB-231 triple negative breast cancer (TNBC) cells (Figure 2.2c). TNBC is one of the most lethal types of breast cancer due to the lack of response to endocrine treatment and other targeted therapies.[110-111] Neoadjuvant and adjuvant chemotherapy currently remain the backbone of treatment in TNBC.[112] The survival of MDA-MB-231 cells was compared after treatment with DOX-LTSLs, DOX-NTSLs, and free DOX for 15 min at 37 °C and 42 °C to evaluate the effectiveness of LTSLs as a chemotherapy drug carrier to treat TNBC. After 15 min, all cells were left undisturbed at 37

°C for 30 hours to induce apoptosis. A live/dead cell assay was performed by staining live cells with calcein and dead cells with propidium iodide. Free DOX (2 μg/mL) resulted in cell death at both physiological temperature (37 °C) and 42 °C showing its severe toxicity at physiological temperatures which leads to off-target cell death with chemotherapy (Figure 2.2, right panel). DOX-NTSLs did not induce cell death at either temperature, showing unsuccessful drug delivery from NTSLs with mild hyperthermia (Figure 2.2, middle panel). Notably, DOX-loaded LTSLs were not cytotoxic to cells at physiological temperature and drug release was triggered only at their phase transition temperature (42 °C) resulting in cell death (Figure 2.2, left panel). These results reinforce the temperature controllability of drug release for LTSLs, an advantage for co-delivery strategies with plasmonic nanostructures.

By co-delivering AuNS with LTSLs in breast cancer cells, the photothermal ability of AuNS is harnessed to directly release DOX in cells for a highly controlled, light-activated cancer therapy. We confirmed AuNS internalization in cell by confocal fluorescence imaging (Figure 2.3a,b) and by TEM imaging (Figure 2.3c-e). To visualize cellular uptake, PEG-coated AuNS were covalently conjugated to fluorescent tag Alexa Fluor 647 via an amide bond and incubated with MDA-MB-231 cells for 24 hours and then imaged with a confocal microscope. At time point zero, when Alexa-Fluor conjugated AuNS was added to the culture media, Z-stack confocal fluorescence images show no AuNS were co-localized at the same focal plane of the cells (Figure 2.3a). Here cells are stained green with calcein and Alexa Fluor conjugated AuNS appear as red fluorescence. Following 24 hours of incubation, clear red fluorescence from Alexa Fluor conjugated AuNS were observable inside cells (Figure 2.3b). Orthogonal view of the z-stack image (right panel in Figure 2.3b) confirmed that AuNS were localized inside the cells in both x-z and y-z directions. To further confirm the uptake and distribution of AuNS inside cells, TEM

micrographs of MDA-MB-231 cells were obtained after 24 hours of incubation with PEG-coated AuNS. The dark clusters in Figure 2.3c indicate that AuNS were endocytosed in cells and entrapped in membrane-bound cytoplasmic vesicles.[113-114] We note AuNS were not observed in the nucleus (indicated by arrow in Figure 2.3c) or the mitochondria (indicated by arrows in Figure 2.3d). High magnification TEM micrograph (Figure 2.3e) shows that PEG-coated AuNS maintained their characteristic anisotropic morphologies cellular internalization.

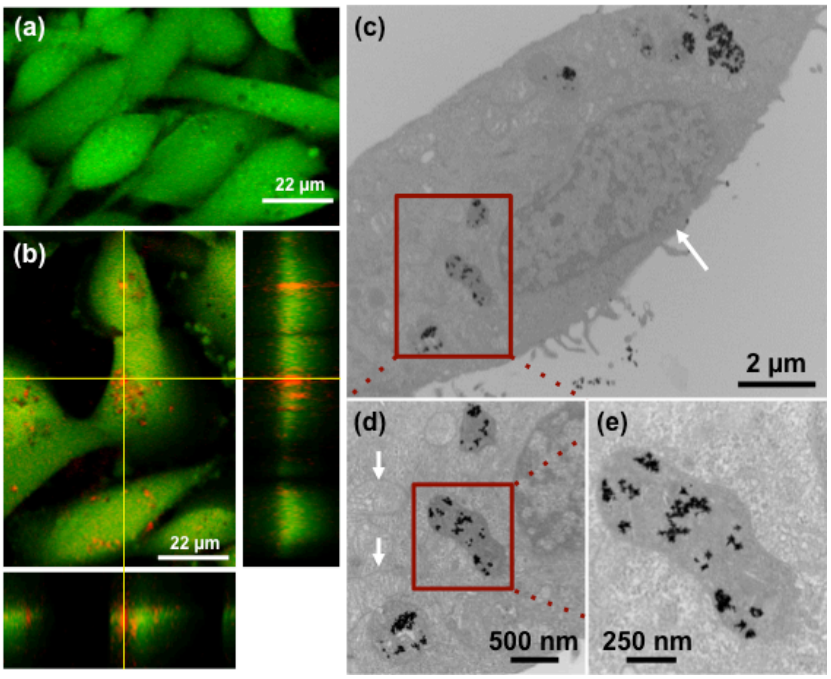

Figure 2.3 Cellular uptake of PEG-coated AuNS by MDA-MB-231 cells. Z stack confocal fluorescence images of cells incubated with PEG-coated AuNS at time zero (a) and after 24 hours of incubation (b). Orthogonal views (right panel in b) at both x-z and y-z direction show PEG-coated AuNS were delivered into the cells. (c-e) Transmission electron micrographs of PEG-coated AuNS show internalization by cells and localization in intracellular vesicles. In addition, PEG-coated AuNS were not found in the nucleus indicated by arrow in (c), nor in the mitochondria indicated by arrows in (d). High magnification micrograph in (e) shows AuNS maintain their anisotropic morphology in cells.

Following uptake of PEG coated AuNS, cells were incubated with either DOX-LTSLs or DOX- NTSLs at 2 μg DOX/ml and subsequently treated with an 808 nm laser at 5.5 W/cm^2 for 15 minutes. An infrared camera was used to monitor the temperature elevation during laser irradiation

(Figure 2.4a). The temperature profile of cellular media with AuNS during these *in vitro* experiments is shown in Figure 2.4b.

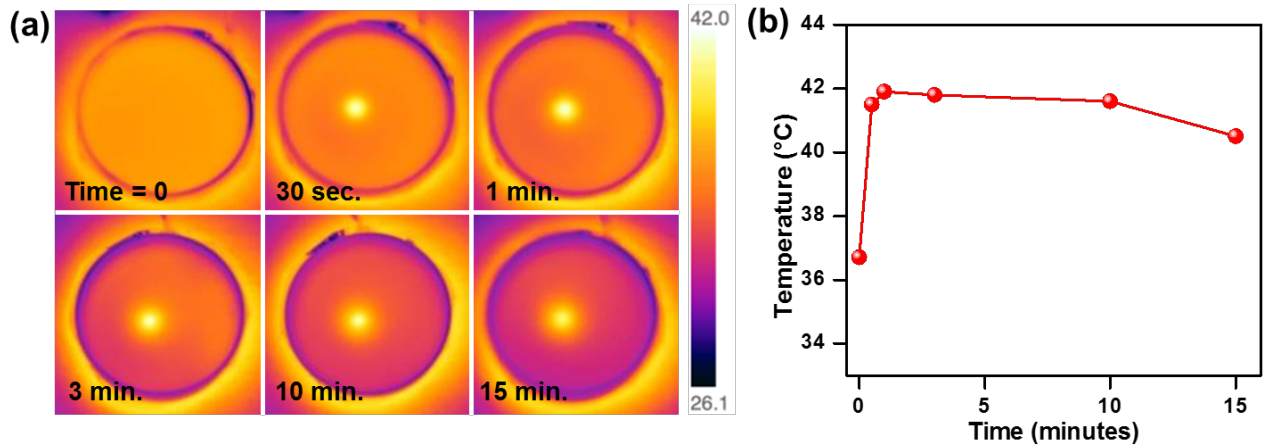

Figure 2.4 (a) Infrared images and (b) the temperature profile of the culture dish during AuNS-mediated photothermal therapy. Cells were incubated with 170 µg/ml of PEG-coated AuNS for 24 hours, washed and illuminated with 5.5 W/cm^2 laser for 15 minutes.

We note that at this laser flux, AuNS generated 42 ±1 °C in the culture dish within the laser beam (3 - 3.5 mm^2 spot size), sufficient to release DOX from LTSLs. Three hours post laser treatment the culture media was removed and cells were washed with PBS buffer. The cells were then stained with Hoechst and imaged with a confocal microscope. Cellular uptake and translocation of DOX into the nucleus was visualized by utilizing DOX's intrinsic fluorescence (excitation at 488 nm, emission at ~570 nm).[115] After drug delivery, a concentration gradient of DOX is generated across the cellular membrane which drives DOX influx into cells; DOX then translocates into the nucleus.[116-118] DOX is known to induce cytotoxicity through both the inhibition of DNA synthesis and the production of free radicals.[119-120] Confocal fluorescent images demonstrate the ability of LTSLs to successfully deliver DOX in cells by utilizing the photothermal hyperthermia induced by AuNS (Figure 2.5, bottom panel). Due to the high phase transition temperature of NTSLs, no DOX delivery was achieved (Figure 2.5, top panel) at mild hyperthermia.

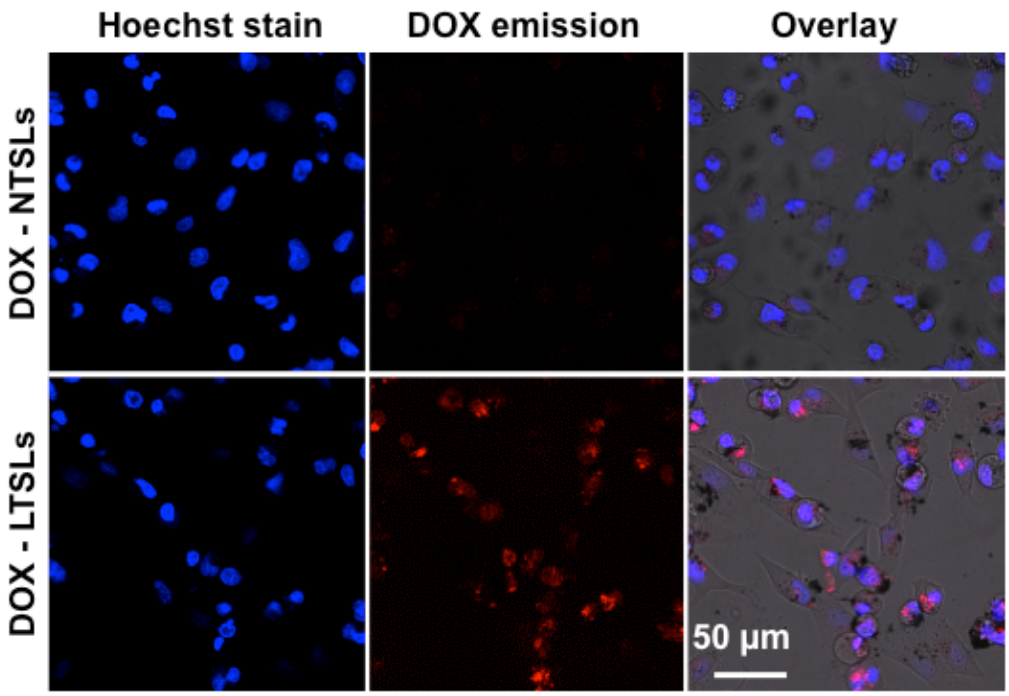

Figure 2.5 Confocal fluorescence images of cells incubated with PEG-coated AuNS, illuminated with an 808 nm laser and treated with either DOX-LTSLs (bottom), or DOX- NTSLs (top). Left panel shows cell nucleus stained with Hoechst, middle panel shows DOX fluorescence at ~570 nm, and right panel is the overlay of left, and middle panel, and bright field.

Light activation of AuNS not only enables highly controlled and localized drug delivery from liposomes, the hyperthermia enhances drug uptake and cytotoxicity of anticancer drugs.[27-28] Mild hyperthermia improves cellular membrane permeability and alters physiological behavior of cells, making them more susceptible to apoptosis.[30, 98, 121-122] We have performed both fluorescence imaging (Figure 2.6) and MTT viability analysis (Figure 2.7) to demonstrate that photothermal hyperthermia induced by AuNS can successfully deliver DOX from LTSLs, resulting in significant dell death. Calcein/PI live/dead cell assays were performed in MDA-MB-231 cells that were illuminated with an 808 nm laser for 15 minutes. Cells were incubated with PEG-coated AuNS in the presence of either DOX-LTSLs (Figure 2.6a) or DOX-NTSLs (Figure 2.6b). Due to the high phase transition temperature (>46 °C) of NTSLs, no cell death was observed with NTSLs with AuNS (Figure 2.6b) or without AuNS (Figure A. 2.3b). This demonstrates that drug delivery from

NTSLs is not achievable under the mild hyperthermia (40-43 °C) generated by AuNS. However, LTSLs in the presence of PEG-coated AuNS successfully released DOX, resulting in intense cell death (Figure 2.6a) where dead cells were stained red with propidium iodide (PI). In the absence of AuNS, DOX-LTSLs did not induce cell death indicating that laser itself does not generate enough heat to release DOX from LTSLs (Figure A. 2.3a). We note that unlike photothermal therapy with gold nanoparticles *in vitro* where necrotic cell death occurs within the laser spot, in photothermal drug delivery *in vitro* cell death is localized in the vicinity of the liposomes, but due to concentration gradient of DOX apoptotic cell death extends slightly beyond the laser spot. This process has been observed previously in light-mediated drug delivery *in vitro*.[123-124] However this does not imply, photothermal DOX release *in vivo* will pose a risk of off-target toxicity since DOX remains within the tumor microenvironment, and successful tumor treatment with this approach has been previously shown.[55] Apoptotic cell death by chemotherapeutic drug is strongly preferred over necrotic cell death incurred during photothermal therapy by gold nanoparticles since necrosis gives rise to uncontrollable inflammation, and undesirable immunogenic responses due to loss of cellular membrane integrity.[125-126] To confirm apoptotic cell death, Annexin was used to stain the phosphatidylserine of apoptotic cells 16 hours post treatment with PEG-coated AuNS + DOX-LTSLs + laser (Figure 2.6c). Calcein and PI were also used to indicate live and dead cells. The overlay image (Figure 2.6d) of Annexin (blue) with calcein (green) and PI (red) clearly shows cells that were undergoing apoptosis where the arrows indicate live cells that were in their apoptotic cell cycle. We note that AuNS themselves alone (Figure A. 2.4a), or laser radiation alone at 5.5 W/cm^2 do not induce significant cell death (Figure A. 2.4b).

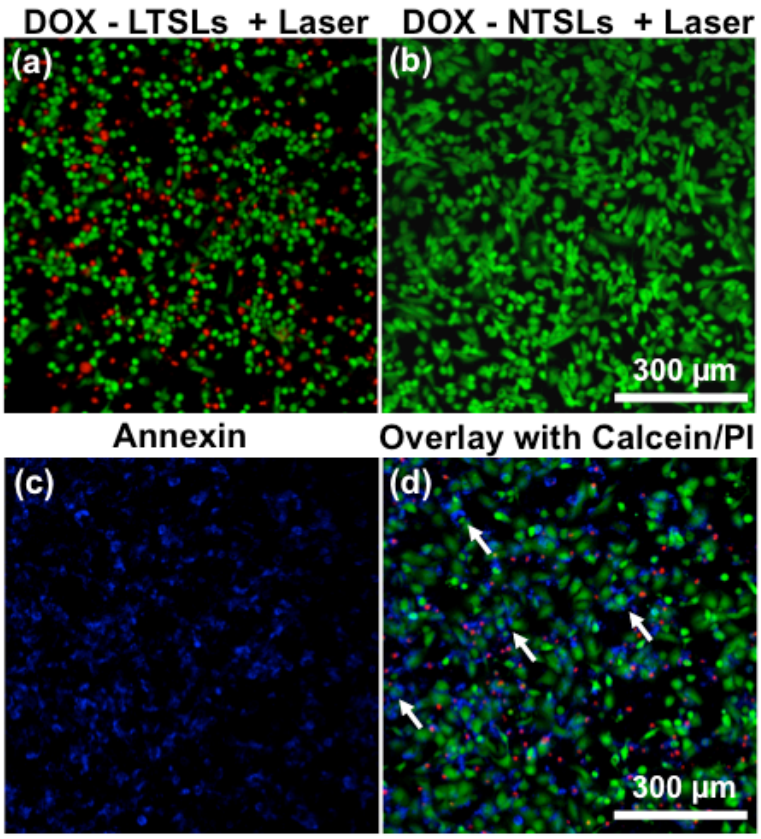

Figure 2.6 Therapeutic effect of photothermal drug delivery from liposomes. MDA-MB-231 cells were incubated with PEG-coated AuNS and (a, c-d) DOX-LTSLs or (b) DOX-NTSLs. Cells were treated with an 808 nm laser at 5.5 W/cm^2 for 15 minutes, laser spot size was ~3.5 mm^2. Cells were stained with calcein (live cells, green) and PI (dead cells, red) 30 hours post-treatment. (c) Cells were also stained with Annexin V (blue) to evaluate apoptotic cell death 16 post-treatment. (d) Overlay image of Annexin V with calcein/PI and arrows indicating the live cells that underwent apoptosis (stained with both blue and green).

Quantitative assessment of the therapeutic outcome of photothermal drug delivery was achieved with MTT cellular viability assays (Figure 2.7). MDA-MB-231 cells were incubated with different concentrations of DOX-LTSLs, DOX-NTSLs, and free DOX for 12 hours both with and without PEG-coated AuNS. At low DOX concentration (0.5 or 2 µg/ml), DOX-LTSLs and DOX-NTSLs did not induce significant cell death, showing >90% survival. Cellular viability decreased to ~77 % using both DOX-LTSLs and DOX-NTSLs at a DOX concentration of 20 µg/ml, likely attributed to the increase in liposomes uptake or leakage of DOX at such high concentrations. Cells treated with DOX-LTSLs alone and irradiated with 808 nm laser do not result in significant cell

death since the laser alone does not generate sufficient heat to reach the phase transition temperature of LTSLs. However, the difference in cellular viability between cells that were treated with DOX-LTSLs + laser, and cells treated with DOX-LTSLs + AuNS + laser at all three DOX concentrations, were statistically significant (p = 0.005 for 0.5 µg/ml, p = 0.003 for 2 µg/ml and p = 0.003 for 20 µg/ml). The photothermal hyperthermia induced by PEG-coated AuNS initiated rapid drug delivery from DOX-LTSLs resulting in cellular viability of 67%, 42% and 39% at 0.5 µg/ml, 2 µg/ml and 20 µg/ml DOX concentrations, respectively. Notably, the combination of AuNS with DOX- LTSLs resulted in higher cell death than free DOX alone at all three concentrations of DOX (84%, 50%, and 43%). For clarity, we also re-plotted the MTT assay data from Figure 6a for the DOX-LTSLs samples (DOX- LTSLs, DOX-LTSLs + laser, and DOX-LTSLs + AuNS + laser) to clearly show a significantly higher cell death is observed due to DOX release from LTSLs in the presence of AuNS (Figure 2.7b). Since NTSLs are not thermally responsive at mild hyperthermia, negligible cell death was observed for all cells incubated with DOX-NTSLs independent of the presence of AuNS.

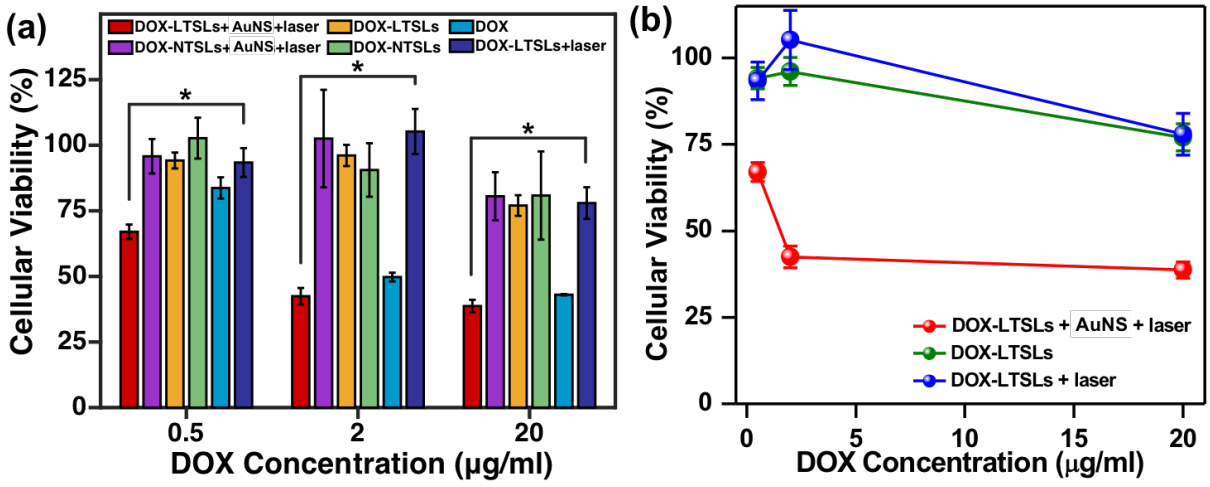

Figure 2.7 (a) MTT assay of all samples and (b) MTT assay summarizing the cellular viability of cells treated with DOX- LTSLs, DOX-LTSLs + laser, and DOX-LTSLs + AuNS + laser. All samples for this assay was illuminated with 808 nm laser at 5.5 W/cm^2 for 15 minutes. Error bars represent n=4 samples. Data is shown in mean ± standard deviation.

Our results convey that the AuNS-mediated mild hyperthermia results in successful drug delivery from LTSLs with high therapeutic efficacy below the United States Food and Drug Agency (FDA) approved DOX concentration. FDA standards for DOX treatment in a 60 kg adult human is ~2 ug/mL every 3 weeks, not to exceed a total of 13.5 ug/mL.[127-129] In summary, while free DOX will induce toxicity even to healthy cells when translated to a clinical setting, targeted photothermal drug delivery with AuNS is light activated, highly controlled, and can minimize off-target toxicities.

2.5 Conclusion

In this study, we synergistically combined the therapeutic effects of PEG coated AuNS with DOX-loaded LTSLs to induce cell death in aggressive triple negative breast cancer (TNBC) cells with a highly controlled, light-activated approach. The unique nanoantenna-like geometry of AuNS, consisting of a core with multiple sharp protrusions, enables strong light-to-heat conversion, allowing rapid and highly efficient drug delivery from LTSLs. We chose a model TNBC cell line, MDA-MB-231, to both qualitatively (calcein/PI live/dead cell assay and apoptosis assay) and quantitatively (MTT assay) assess the therapeutic outcome of AuNS combined with DOX loaded LTSLs. Our results provide strong evidence that photothermal heating by AuNS gives rise to mild hyperthermia sufficient to reach the phase transition temperature of LTSLs, resulting in 58% cell death at a DOX concentration of 2 μg/ml. We envision the co-delivery of LTSLs with AuNS will ultimately facilitate a clinically applicable technology, enabling the delivery of dose-controlled treatment and minimizing off-target toxicities that are associated with chemotherapy. Future integration of this approach to include imaging capabilities would enable longitudinal tracking to further improve detection, treatment, and assessment of therapeutic outcomes with a platform that

can be externally-triggered by near-infrared light. In addition, LTSLs can ultimately be loaded with a range of drugs, and when combined with AuNS this platform will facilitate targeted treatment of multiple diseases, including cancer, multiple sclerosis, and many infectious diseases.

2.6 Appendix

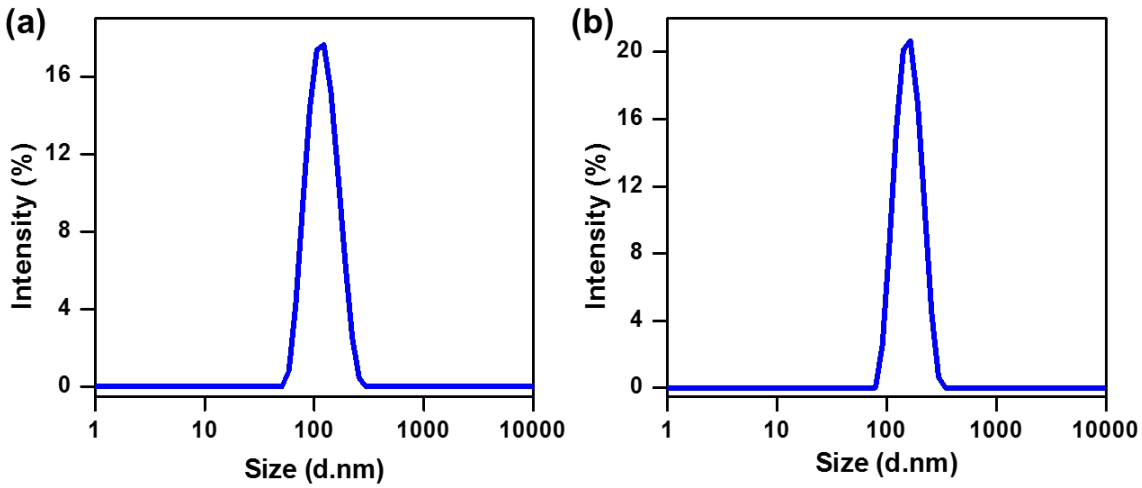

Figure A. 2.1 Dynamic light scattering (DLS) showing the hydrodynamic diameter of (a) DOX-LTSLs and (b) DOX- NTSLs.

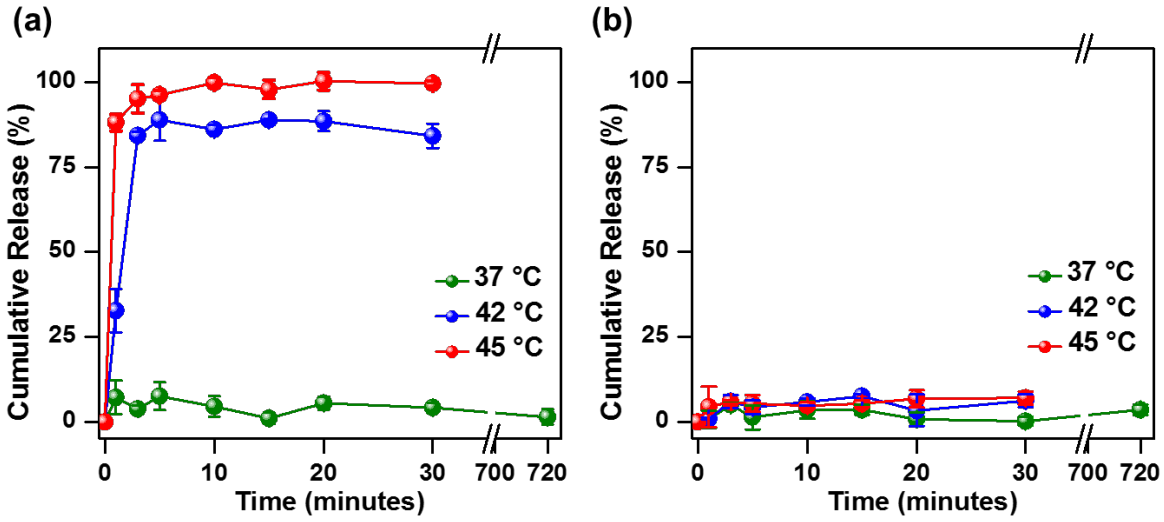

Figure A. 2.2 DOX release from (a) DOX-LTSLs and (b) DOX-NTSLs at 37, 42 and 45 ^{0}C. Long-term stability of DOX-LTSLs and DOX-NTSLs at physiological temperature is also shown for 12 hours.

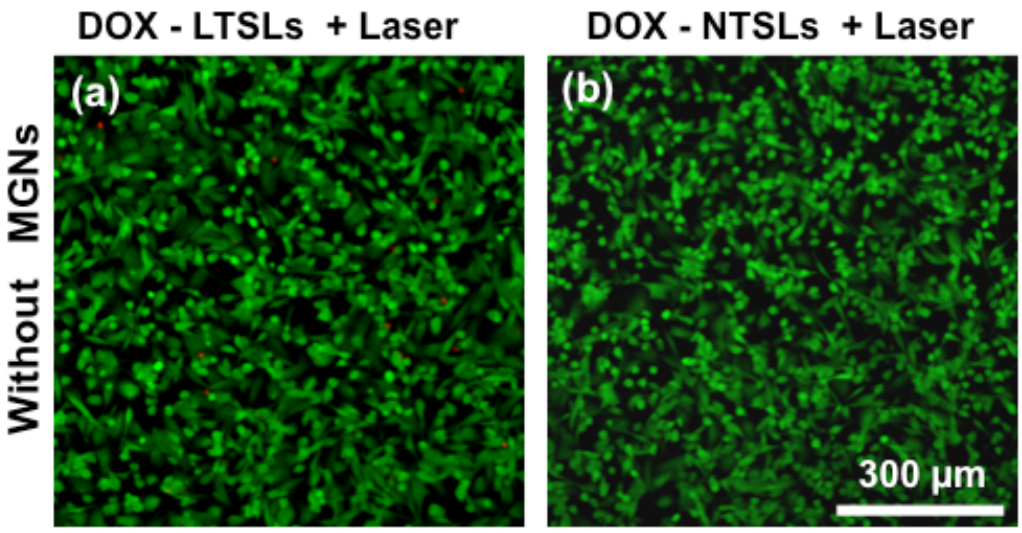

Figure A. 2.3 MDA-MB-231 cells were incubated without PEG-coated AuNS, but with (a) DOX-LTSLs and (b) DOX-NTSLS. Cells were treated with an 808 nm laser at 5.5 W/cm^2 for 15 minutes, laser spot size was ~3.5 mm^2. Cells were stained with calcein (live cells, green) and PI (dead cells, red) 30 hours post-treatment.

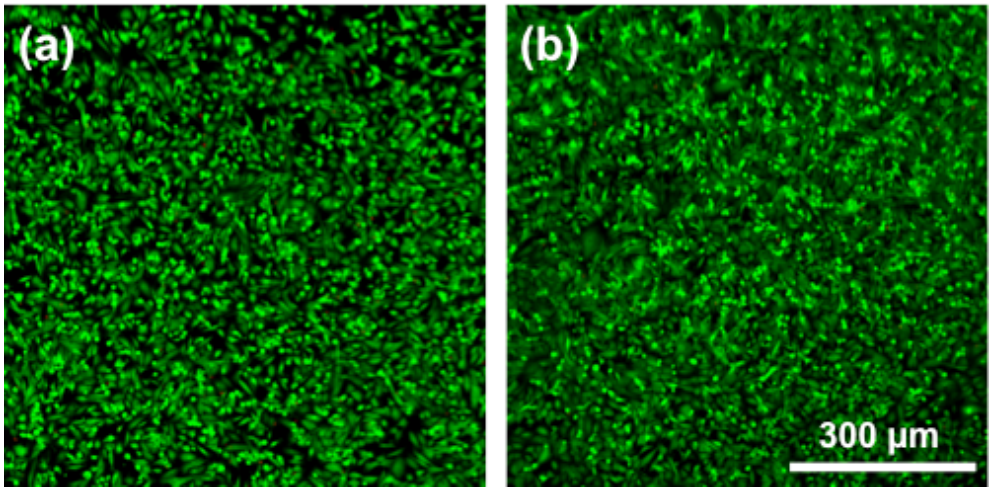

Figure A. 2.4 Confocal image of MDA-MB-231 cells (a) incubated with PEG-coated AuNS for 24 hours but not treated with laser, and (b) illuminated with an 808 nm laser alone (without AuNS) at 5.5 W/cm^2 for 15 minutes. Cells were stained with calcein (live cell, green) and propidium iodide (dead cell, red).

Chapter 3

MULTIPLEXED SURFACE ENHANCED RAMAN SPECTROSCOPY WITH GOLD NANOSTARS FOR DETECTION OF CANCER SPECIFIC BIOMARKER

Adopted from: Webb, J. A.; Ou, Y. C.; Faley, S.; Paul, E. P.; Hittinger, J. P.; Cutright, C. C.; Lin, E. C.; Bellan, L. M.; Bardhan, R., Theranostic gold nanoantennas for simultaneous multiplexed raman imaging of immunomarkers and photothermal therapy. *ACS Omega* **2017,** *2* (7), 3583-3594 *with permission from the American Chemical Society.*

And

Ou, Y. C.; Webb, J. A.; O'Brien, C. M.; Pence, I. J.; Lin, E. C.; Paul, E. P.; Cole, D.; Ou, S. H.; Lapierre-Landry, M.; DeLapp, R. C.; Lippmann, E. S.; Mahadevan-Jansen, A.; Bardhan, R., Diagnosis of immunomarkers in vivo via multiplexed surface enhanced Raman spectroscopy with gold nanostars. *Nanoscale* **2018,** *10* (27), 13092-1310 *with permission from the Royal Society of Chemistry*.

3.1 Summary

In this work, we demonstrate the targeted diagnosis of immunomarker programmed death ligand 1 (PD-L1) and simultaneous detection of epidermal growth factor receptor (EGFR) in breast cancer tumors *in vivo* using gold nanostars (AuNS) with multiplexed surface enhanced Raman spectroscopy (SERS). Real- time longitudinal tracking with SERS demonstrated maximum accumulation of AuNS occurred 6 h post intravenous (IV) delivery, enabling detection of both biomarkers simultaneously. Raman signals correlating to both PD-L1 and EGFR decreased by ~30% in control tumors where receptors were pre-blocked prior to AuNS delivery, indicating both the sensitivity and specificity of SERS in distinguishing tumors with different levels of PD-L1 and EGFR expression. Our *in vivo* study was combined with the first demonstration of *ex vivo* SERS spatial maps of whole tumor lesions that provided both a qualitative and quantitative assessment of biomarker status with near cellular-level resolution. High resolution SERS maps also provided an overview of AuNS distribution in tumors which correlated well with the vascular density. Mass

spectrometry showed AuNS accumulation in tumor and liver, and clearance via spleen. Electron microscopy revealed AuNS were endocytosed in tumors, Kupffer cells in the liver, and macrophages in the spleen. This study demonstrates that SERS-based diagnosis mediated by AuNS provides an accurate measure of multiple biomarkers both *in vivo* and *ex vivo*, which will ultimately enable a clinically-translatable platform for patient-tailored immunotherapies and combination treatments.

3.2 Introduction

T cells are an important effector of the immune system and are critical for inhibition of tumor development, growth, and invasion. Therefore, tumors evolve to evade immune surveillance by orchestrating a tumor microenvironment that suppresses productive antitumor immunity.[130-131] The overexpression of immune checkpoint receptor programmed death protein-1 (PD-1), expressed in activated T cells, and the subsequent engagement of PD-1 to its ligand PD-L1 results in inhibition of T cell proliferation, reduced secretion of effector cytokines, and immunosuppression.[132] PD-L1 is upregulated in numerous tumor types including breast cancer,[133] renal-cell cancer,[134] non-small cell cancer,[135] and melanoma[136] among others. This underscores the significance of PD-L1 as a predictive biomarker for immunotherapies. Inhibition of PD-L1 with therapeutic antibodies has shown to activate antitumor immunity and long term patient survival.[137-138] However, <25% of patients respond to PD-L1 blockade incurring high costs of unsuccessful therapies and toxic side-effects from prolonged antibody treatment.[138-139] Current clinical standards rely on immunohistochemistry (IHC) of biopsies, which often provide poor assessment of PD-L1 status in tumors. First, there are no clear criteria to define PD-L1 positivity by IHC which makes this approach prone to misinterpretation due to heterogeneous PD-L1 expression in inter-

and intra-tumoral lesions.[140-141] Second, retrieval of PD-L1 antigen is also difficult in fixed tissue which results in significant variability in PD-L1 assay across clinical trials.[142] Further, IHC of PD-L1 expression on archival tissue samples should be determined with caution, as prior treatment procedures can alter PD-L1 status in the tumor microenvironment.[143-144] And last, IHC is also limited in validation of multiple biomarkers in the same biopsy requiring repeated invasive procedures and patient discomfort. Therefore, a clinical need exists for noninvasive diagnostic tools that can both accurately identify PD-L1 *in vivo* and concurrently detect other biomarkers to identify patients who will respond to single checkpoint blockade, as well as accelerate clinical decisions by diagnosing patients who will benefit from combinatorial therapies.

In this work we address this critical need and demonstrate the diagnosis of PD-L1 *in vivo* and simultaneously diagnose EGFR (epidermal growth factor receptor) in triple negative breast cancer (TNBC) tumors. TNBC is a highly aggressive phenotype of breast cancer characterized by the lack of estrogen receptor, progesterone receptor, and HER2/neu. Despite high rates of pathologic complete response after neoadjuvant chemotherapy, patient survival rates remain low. Recent work has shown TNBC tumors are highly immunogenic with high PD-L1 gene expression and higher rates of $CD8^+$ T-cell infiltration than ER/PR positive breast cancer.[145] Further, many TNBC tumors are known to overexpress EGFR, which is a transmembrane glycoprotein.[146] The upregulation of EGFR promotes tumor progression by enhancing cell growth, angiogenesis, metastasis, and anti-apoptosis. Several EGFR-tyrosine kinase inhibitors, for example, gefitinib and erlotinib, have demonstrated clinical efficacy in blocking the signal transduction pathways involved in tumorigenesis. Recent studies have also demonstrated that EGFR mutation status is directly correlated to the upregulation of PD-L1 which motivates us to diagnose both biomarkers with high sensitivity and specificity.[147-149] We have achieved this with noninvasive, multiplexed,

surface-enhanced Raman spectroscopy (SERS) using gold nanostars (AuNS) labeled with targeting antibodies and Raman active molecules. SERS has rapidly emerged from a simple analytical technique to a preclinical screening tool for both qualitative and quantitative measure of biomarkers in tumors and for identification of cancerous cells.[150-152] SERS seamlessly enables multiplexed detection of multiple biomarkers due to the narrow linewidths of vibrational signatures of Raman molecules that can be simultaneously tracked both *in vivo* and *ex vivo*.[153-155] The high spatiotemporal resolution of SERS has also enabled delineation of tumor margin from healthy tissue, and facilitated intraoperative tumor resection followed by identification of any residual disease.[156-158]

In this work we demonstrate longitudinal tracking of both PD-L1 and EGFR *in vivo* showing the localization of each marker with high sensitivity and specificity after intravenous delivery of AuNS in mouse models of TNBC. We note that whereas nanoparticles are often intratumorally delivered *in vivo* to achieve high SERS signal,[155, 159-160] our approach of intravenous delivery is more clinically relevant for biomarker assessment. The strength of this work is *in vivo* time course study was combined with the *first demonstration* of *ex vivo* SERS maps of whole tumor lesions, that provided both a qualitative assessment of biomarker status and quantitative measure of their expression levels. High spatial resolution SERS maps also revealed distribution of AuNS in tumors that correlated well with highly vascularized areas of the tumor. Further, we examined the bioavailability and clearance of AuNS and corresponded those trends to *in vivo* endpoints. We anticipate the findings of this work will ultimately be extended to large animals and humans, and enable a clinically-translatable technology towards the emerging fields of immunoimaging and immunotherapies.

3.3 Materials and Methods

3.3.1 Synthesis and Functionalization of Gold Nanostars (AuNS)

Both (4-(2-hydroxyethyl)-1-piperazineethanesulfonic acid) (HEPES) and gold(III) chloride trihydrate (HAuCl4) were purchased from Sigma-Aldrich. AuNS were synthesized through the one-step, seedless, HEPES-mediated method.[25] First, 18 mL of Milli-Q water at 18 MΩ was mixed with 12 mL of 270 mM HEPES (pH 7.40 ± 0.2) by gentle inversion. Next, 300 μL of 20 mM chloroauric acid ($HAuCl_4$) was added. The solution was left undisturbed at room temperature and reacted for 75 minutes.

SERS tags, 4-mercaptobenzoic acid (pMBA) and 5,5'-Dithiobis(2-nitrobenzoic acid) (DTNB) were purchased from TCI America. Methoxy-polyethlyene glycol-thiol (mPEG-SH, M_w 5000) and orthopyridyl-disulfide poly(ethylene glycol)-N-hydroxysuccinimide ester (OPSS-PEG-NHS ester, M_w 2000) were purchased from JenKem Technology. To conjugate Raman tags to the AuNS surface, pMBA or DTNB were dissolved in 100% ethanol. Small concentrated volume (6 μL of 10 mM) of pMBA or DTNB solution was added to 60 mL of AuNS and reacted for 10 minutes with constant stirring at 4 ^{0}C. The solution was centrifuged at 6000 rpm for 10 minutes to remove excess, unreacted Raman tag. To bind active targeting antibody to AuNS, OPSS-PEG-NHS linkers were first reacted with the monoclonal antibodies, Human EGF R/ErbB1 antibody (antiEGFR, R & D Systems) or Human CD274 (B7-H1, PD-L1) antibody (antiPDL1, BioLegend). Briefly, lyophilized OPSS-PEG-NHS was dissolved in 100 mM pH 8.6 ± 0.1 sodium bicarbonate ($NaHCO_3$) buffer at a concentration of 160 mg/mL. Note, high pH is crucial for ester and amine chemistry in forming amide bonds. As a result, the antibody chemistry was tailored to achieve this desirable pH. At 1:9 volume ratio, 72 μL of 1 mg/mL antiEGFR antibody (reconsistuted in pH 8.6 $NaHCO_3$ buffer) was added to 8 μL of OPSS-PEG-NHS solution. AntiPDL1 antibody was

received at pH 7.4 phosphate buffer saline. To maintain the favorable pH for linker-antibody reaction, OPSS-PEG-antiPD-L1 was prepared in the concentration and volume ratio as with the OPSS-PEG-antiEGFR reaction, but it was further diluted 5-fold with pH 8.6 $NaHCO_3$. The OPSS-PEG-antibody chemistry was performed on an inverter at 4 °C for 24 h.

After the OPSS-PEG-antibody reaction was completed, 80 µL of OPSS-PEG-antiEGFR or OPSS-PEG-antiPDL1 was added to 6 ml of Raman tag-labeled-AuNS (DTNB-AuNS or pMBA-AuNS) at 1.14 mg/mL. Antibody-AuNS solution was left on an inverter at 4 °C and reacted for 24 h. Post 24 h antibody-AuNS reaction, an additional layer of polyethylene glycol (mPEG-SH, M_w 5000) chemistry was performed to passivate any free surface area on the gold, neutralize surface charge, and provide particle stability. Briefly, 700 µL of 5 µM mPEG-SH was added to the AuNS solution and mixed for 10 minutes at room temperature. Lastly, the functionalized AuNS (antiEGFR-pMBA-AuNS or antiPDL1-DTNB-AuNS) were centrifuged at 4000 rpm for 10 minutes. The pellet was then resuspended in sterile phosphate buffered saline (pH 7.40 ± 0.1) at 6 mg/mL.

3.3.2 Characterization of Functionalized AuNS

A 2:1 mixture of antiEGFR-pMBA-AuNS and antiPD-L1-DTNB-AuNS were visualized using an Osiris transmission electron microscope (TEM) at 200 keV. Plasmon resonance of AuNS and functionalized AuNS were monitored with a Varian Cary 5000 UV-Vis NIR spectrophotometer. Raman spectra of antiEGFR-pMBA-AuNS, antiPD-L1-DTNB-AuNS, and the 2:1 mixture were obtained by using the custom portable Raman setup with a 785 nm laser.

3.3.3 In Vitro SERS Multiplex Imaging of MDA-MB-231 cells

<u>Multiplex with (1:1) Cocktail with MDA-MB-231 cells</u>

CaF_2 disks were seeded with MDA-MB-231 cells. Cells were incubated with media (no FBS, nDMEM) supplemented with 170 µg/mL (1:1) cocktail antiEGFR-pMBA-AuNS to antiPDL1-DTNB-AuNS for 16 h at 37 ^{0}C. Next, cells were washed with nDMEM (x2), equilibrated for 2 h at 37 ^{0}C. After 2 h in cDMEM, cells were fixed, washed and dried overnight at 4 ^{0}C. Using an 100x objective, a video montage of the cells was captured, and the resulting brightfield image provided x,y coordinates for the Raman instrument to record SERS chemical footprints of a rectangular area of ~100 µm by 100 µm. Recording spectra with 0.75 µm steps, the Raman microscope took measurements of the cells with a 785 nm wavelength laser source with 1200 lines/mm grating in high confocal mode. Static spectra (1200 cm^{-1} center) were recorded using a 100x objective with a ~1 µm spot size at a power of 1 mW with a 10 s acquisition time.

Multiplex with (1:1) Cocktail with 231 cells after Blocking PD-L1 Receptor

To test the fidelity of the multiplex technology, a blocking PD-L1 receptor control experiment was performed to determine the specificity and mapping capability of this (1:1) cocktail of functionalized antibody-specific AuNS. MDA-MB-231s were seeded on CaF_2 disks and pre-blocked by incubating with nDMEM supplemented with 4 µg/mL Human CD274 (B7-H1, PD-L1) antibody (monoclonal antiPDL1) for 1 h at 37 ^{0}C.[161-163] Cells were then washed, equilibrated in cDMEM, fixed and dried.

3.3.4 MDA-MB-231 Xenograft Model and in vivo SERS Raman Imaging

All animal procedures were followed and approved by Vanderbilt University Medical Center Animal Care and Use Program (IACUC #M1600097-00). Athymic nude mice at 3-4 week old (Hsd: Athymic Nude-Foxn1^{nu}; Envigo) were used in this study. MDA-MB-231 cells were cultured in Dulbecco's Modified Eagle's medium (DMEM, Gibco) supplemented with 10% fetal bovine serum (FBS, Denville Scientific). The cells were maintained at 37 ^{0}C and 5% CO_2 and

were cultured at least two weeks prior to injection into mice. The cells were diluted 1:1 with matrigel (GFR Membrane Matrix, Corning). One million MDA-MB-231 cells per 100 µl were injected into the left mammary fat pad of each mouse. The tumor was monitored with calipers every two days. SERS experiments started once the tumor reached 5 mm in diameter. SERS spectra of 5 different spots of the tumor xenograft were measured with 10 s acquisition time before functionalized AuNS were injected (0 h). Functionalized AuNS, antiEGFR-pMBA-AuNS and antiPDL1-DTNB-AuNS at 2:1 ratio were injected retro-orbitally. Raman measurement was done at 6, 12, 24, 48 and 72 h post particle injection. For each time point, mice were anesthetized with isoflurane. All room lights were turned off during SERS measurement. The Raman fiber optic probe was gently placed on the tumor xenograft for a spectral measurement (1 s acquisition time per spectrum with 10 accumulations). A 785 nm near-infrared diode laser (Innovative Photonics Solutions) was operated at 80 mW. A neon-argon lamp, acetaminophen, and naphthalene were used as standards to calibrate the absolute and relative wavenumber axis of the system in determining and calculating Raman shifts. Raman scattering was collected with an imaging spectrograph (Kaiser Holospec), and a -70 °C cooled CCD camera (Princeton Instruments) was used to capture the data, which was further processed by the connected computer system.

All obtained spectra were processed through steps including spectral response calibration with a NIST calibrated lamp, smoothing using a (2,7) Savitzky-Golay filter, and background subtraction using a modified (7^{th} order) polynomial fit method.[164-167] To clearly visualize the appearance of DTNB and pMBA peaks, 1325 cm^{-1} and 1580 cm^{-1} were normalized to the biological peak, 1440 cm^{-1} at each time point. For pre-block control, mice were injected (IP) with 200 µg of antiEGFR antibody and 200 µg of antiPDL1 antibody (1 mg/mL in pH 7.40 ± 0.1 phosphate buffered saline) 2 h before functionalized AuNS injection. Note, the antibodies used for

pre-blocked controls were the same products used to functionalize the active targeting AuNS. Raman measurement for the pre-block control group was performed in the same manner as the experiment group.

3.3.5 Inductively Coupled Plasma-Mass Spectrometry (IC-PMS)

Mice bearing MDA-MB-231 cells were injected with functionalized AuNS, antiEGFR-pMBA-AuNS and antiPDL1-DTNB-AuNS at 2:1 ratio. Per mouse, the tumor, stomach, liver, spleen, kidneys, heart, lungs, and brain were retrieved at maximum accumulation time (6 h post particle injection) or at the end of the study (72 h post particle injection) and were frozen immediately in liquid nitrogen.

Sample Preparation

Tumors and major organs were then freeze dried using a lyophilizer. Next, acid digestion was used to dissolve gold contents. Dried tumors and organs were place in scintillation vials and weighed. Trace metal grade HCl (Fisher, A508-P500) and HNO_3 (Fisher, A509-P500) were used to prepare 75 vol. % aqua regia (4:1 volume ratio HCl: HNO_3), which was then added to the organ/tumor. Samples were soaked in aqua regia for 72 h. Aqua regia was then boiled off with gentle heating. The semi-dried samples were re-dissolved in 10 ml of 2 vol. % aqua regia. Impurities were removed with syringe filtering prior to IC-PMS reading. Organs with high gold accumulation: liver, spleen, and tumor were further diluted 10-fold with 2 vol. % aqua regia.

IC-PMS Analysis

IC-PMS Analysis IC-PMS measurements of aqueous samples were carried out at Vanderbilt University, Department of Civil and Environmental Engineering. Perkin Elmer model ELAN DRC II in standard mode was used for readings. A six-point calibration curve between approximately 0.05 µg/L and 500 µg/L was used for gold isotope 197. For every 3-5 samples,

analytical blanks and analytical check standards (0.5 µg/L) were measured and confirmed to be within 15% of the specified value. The instrument was set at 1.5 kW radio frequency (RF) power, 15 L/min argon plasma flow, 1 L/min nebulizer flow, and 1 s integration time for 3 replicates.

3.3.6 Transmission Electron Microscope Imaging of Tumor and Organs

Mice bearing MDA-MB-231 cells were injected with functionalized AuNS, antiEGFR-pMBA-AuNS and antiPDL1-DTNB-AuNS at 2:1 ratio. SERS spectra were measured at 6 h post particle injection to ensure the increase in DTNB/pMBA signal was observed. The mouse was then sacrificed, and the tumor xenograft was retrieved. Additionally, the heart, liver, and spleen of a different set of mice were removed 72 h post functionalized AuNS injection to evaluate the clearance of the particles. Samples were fixed in 2.5% gluteraldehyde in 0.1M cacodylate buffer (pH 7.4 ± 0.1) at room temperature for 1 h and then 24 h at 4 ºC. Specimens were processed for transition electron microscopy (TEM) and imaged in the Vanderbilt Cell Imaging Shared Resource-Research Electron Microscopy facility.

Sample Preparation

The samples were fixed with 1% osmium tetraoxide for 1 h at room temperature and further washed with 0.1 M cacodylate buffer. Dehydration was done through a graded ethanol series. Next, 3 exchanges of 100% ethanol and 2 exchanges of pure propylene oxide (PO) were performed. Subsequently, 25% Epon 812 resin and 75% PO were used to infiltrate the samples for 30 min at room temperature. They were then infiltrated with 50% Epon 812 resin and 50% PO for 1 h and overnight, respectively. The samples went through a Epon 812 resin and PO (3:1) exchange for 4 h and finally were incubated with pure epoxy resin overnight. Lastly, two changes of pure epoxy resin were used to embed the samples. Polymerization was done for 2 days at 60 °C. Ultra-structure identification was first achieved with thick sections at 500-1000 nm. Once regions of interest were

identified, 70-80 nm ultra-thin sections were cut. Samples were placed on 300-mesh copper grids and were stained with 2% uranyl acetate, followed by Reynold's lead citrate. The final tissue samples were imaged with the Philips/FEI Tecnai T12 electron microscope.

3.3.7 Ex vivo Raman Mapping

Mice bearing MDA-MB-231 were injected with functionalized AuNS (antiEGFR-pMBA-AuNS and antiPDL1-DTNB-AuNS at 2:1 ratio) retro-orbitally. The tumor xenograft was retrieved and cryo-embedded 6 h post particle administration. Frozen tumor samples were cryo-sectioned on CaF_2 disks by Vanderbilt University TPSR (5 μm thick). Samples were thawed at 4 °C overnight and then room temperature for 2 h prior to Raman mapping. Montages of brightfield images were obtained with a 20x (NA) objective. A rectangular Raman map with a 50 μm step size was acquired with 10 s integration time, L50x objective (NA), and a 785 nm laser (30 mW). After the Raman spectra for the entire map were obtained, cosmic ray removal with nearest neighbor method was implemented. A custom MATLAB code was used to perform smoothing and biological fluorescent background subtraction. Smoothing of the data was done by following the Savitzsky and Golay method with 5^{th} order and coefficient value of 61. Modified polyfit method was performed to subtract the background fluorescence. A polynomial with 9^{th} order was used to fit the Raman spectra with threshold of 0.0002. The Raman mapwas then generated with wavenumber of interest (DTNB = red, pMBA = green).

To obtain quantitative analysis of both pMBA and DTNB, the raw biological peak (1440 cm^{-1}) was selected to generate the masks of whole tissues. The pixels were assigned as a part of a mask when their intensities were higher than a specified threshold. A Gaussian function was applied to the mask images to smooth the edges (sigma = 20 μm). The residuals and the holes in the images were removed and filled (area opening algorithm), respectively. The final masks were

compared with the optical images to ensure the authenticities. The sub-masks of high- and low-intensity groups were obtained in a similar fashion from the processed (smoothed and baseline corrected) images of biological peak. These masks were separated according to a threshold and are processed with necessary smoothing, removing, and filling. Tissue mask and sub-masks were then applied to 1325 cm^{-1} and 1580 cm^{-1} for each individual tag. As a result, the Gaussian model mean and sigma can be obtained.

3.3.8 Statistical Analysis

Statistical differences were evaluated with Student's t tests. All data are presented as mean ± standard deviation.

3.4 Results and Discussion

Gold nanostars (AuNS) were synthesized by a one-step seedless method as described in our previously published procedure.[25, 168-169] The biological buffer, HEPES (2-[4-(2-hydroxyethyl)piperazin-1-yl]ethanesulfonic acid) is used as both a capping and reducing agent, enabling shape-controlled synthesis. Gold nanoparticles synthesized via biological buffer or peptides are biocompatible with minimal toxicity.[37, 38] The sub-100 nm size of AuNS (~50-70 nm tip-to-tip dimension (Figure 3.1a) allows AuNS to accumulate in the tumor microenvironment through the enhanced permeability and retention effect (EPR), thus increasing the likelihood of endocytosis by cancer cells.[170-171] The unique structure of AuNS gives rise to the "nanoantenna effect" where the spherical cores absorb incident light and route it to the protrusions where strong electromagnetic field are concentrated at the tips.[25, 63, 172] These intense near-field enhancements at the tips of AuNS amplify the vibrational signal of proximal Raman molecules by 9 – 10 orders of magnitude enabling high resolution SERS.[42, 10] In this work, we show the multiplexed detection

of biomarkers PD-L1 and EGFR through SERS by conjugating Raman tags and monoclonal antibodies specific to these biomarkers onto AuNS surface (Figure 3.1b). We generated two sets of bioconjugated AuNS, PD-L1 targeting set was labeled with Raman tag 5,5-dithio-bis-(2-nitrobenzoic acid) (DTNB) and anti-PD-L1 monoclonal antibodies, and EGFR targeting set was labeled with Raman tag para-mercaptobenzoic acid (pMBA) and anti-EGFR antibodies. Both DTNB and pMBA were covalently linked to AuNS surface via a thiol group. Monoclonal antibodies were conjugated with AuNS via OPSS-PEG2000-NHS linkers where the thiols on the orthopyridyl (OPSS) group bind to AuNS, and the N-hydroxysuccinimide (NHS) ester group forms an amide bond via the primary amines of the antibodies. Lastly, a layer of thiolated-polyethylene glycol was added to AuNS surface to ensure charge neutrality, reduce uptake by the mononuclear phagocytic system (MPS), and to provide *in vivo* stability. The biofunctionalization of AuNS resulted in a ~25 nm shift in the plasmon resonance (Figure 3.1c) indicative of an increase in the particle size as well as change in refractive index of the medium. The plasmon resonance of functionalized AuNS was controlled in the near-infrared region (650-900 nm) to enable enhanced tissue penetration and deep tissue imaging. The Raman spectra of the functionalized AuNS were acquired using a custom Raman system with a 785 nm continuous wave laser (Figure 3.1d). The signature peak of antiEGFR-pMBA-AuNS is at 1580 cm^{-1}, which corresponds to the ring stretching mode of pMBA.[173] The dominant peak, 1325 cm^{-1} of antiPD-L1-DTNB-AuNS is attributed to the symmetric stretching mode of the nitro group of DTNB.[174] For multiplexed SERS a 2:1 ratio of antiEGFR-pMBA-AuNS: antiPD-L1-DTNB-AuNS was employed since the peaks of interest for DTNB and pMBA have comparable Raman intensities at this ratio. Furthermore, due to their distinct Raman fingerprints and narrow linewidths, both pMBA and DTNB are easily distinguishable enabling multiplexed detection of PD-L1 and EGFR both *in vitro* and *in vivo*.

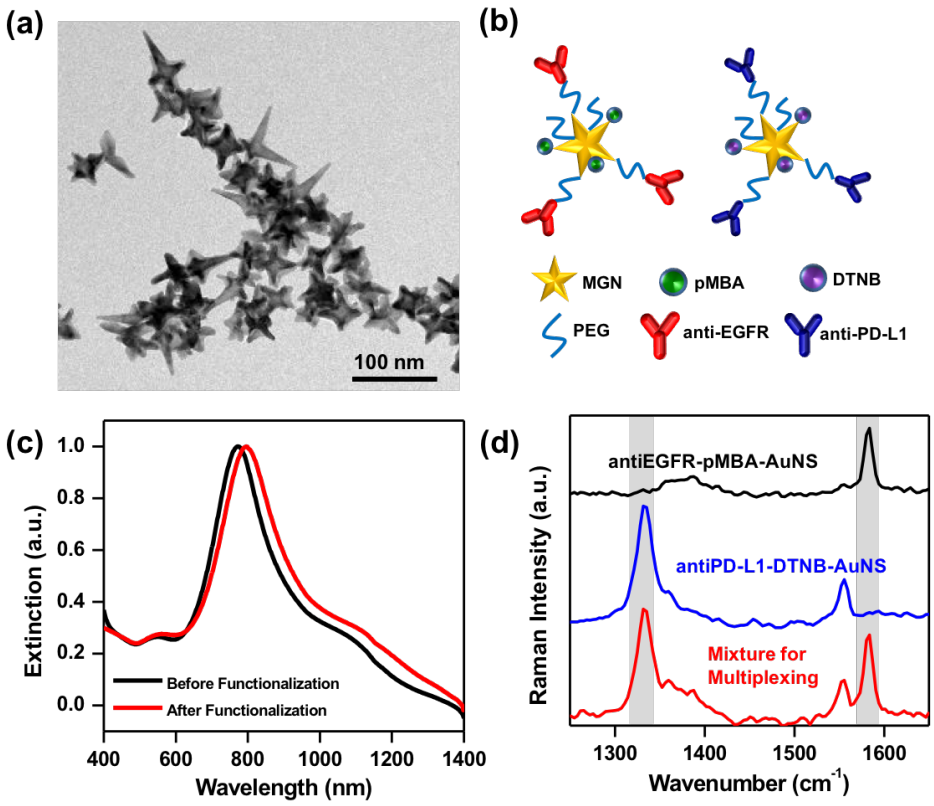

Figure 3.1 Characterization of functionalized AuNS. (a) TEM image of antibodies and Raman tag functionalized AuNS showing the anisotropic structure and sub-100 nm size of AuNS. (b) Schematic representation of AuNS functionalized with Raman-active tag, pMBA or DTNB. Each Raman tag pairs with a targeting antibody, anti-EGFR with pMBA and anti-PD-L1 with DTNB. (c) Extinction spectra of AuNS before (bare AuNS) and after functionalization (with Raman tag and targeting antibody). (d) Raman spectra of antiEGFR-pMBA-AuNS, antiPDL1-DTNB-AuNS and a 2:1 mixture. The Raman peaks of interest of both pMBA and DTNB are highlighted in gray.

To confirm the receptor-antibody binding, we incubated the MDA_MB-231 cells with a mixture of antiEGFR-pMBA-AuNS: antiPD-L1-DTNB-AuNS. After 16 h of incubation, TEM micrographs showed most of the AuNS were bound to the surface of the cancer cells with minimal endocytosis (Figure A. 3.1).

We first performed multiplexed SERS imaging *in vitro* by simultaneously incubating cells with a mixture of antiPDL1-DTNB-AuNS and antiEGFR-pMBA- AuNS in a 1:1 ratio. Because the vibrational signature of DTNB and pMBA do not overlap, this approach allows us to detect both PD-L1 and EGFR by mapping the signal of DTNB (1325 cm^{-1}) and pMBA (1580 cm^{-1})

respectively. Brightfield image (Figure 3.2a) shows an image of cells with light scattering from AuNS localized on cell surface. A Raman spectral map of ~100 μm x 100 μm was measured with 0.75 μm steps, and the intensity of 1325^{-1} peak ($I_{SERS1325}$) and 1580 cm^{-1} peak ($I_{SERS1580}$) was plotted together as a function of position (Figure 3.2b). Strong signal is observable from both DTNB and pMBA, and the high spatiotemporal resolution of Raman allows us to qualitatively evaluate the localization of individual receptor bound AuNS. A magnified view of local traffic map of multiplexed SERS footprint is shown in Figure 4c correlating the distribution of PD-L1 and EGFR in the cells. Note that strong signal is observed where multiple AuNS cluster giving rise to SERS enhancements via hot spots. Specific locations on the magnified SERS map (Figure 3.2c) and corresponding SERS spectra (Figure 3.2d) indicate spatial localization from both probes (Figure 3.2di), DTNB alone (Figure 3.2dii), pMBA alone (Figure 3.2diii), or signal only from cellular lipids at 1440 cm^{-1} (Figure 3.2div).[175] We note that the intrinsic Raman peaks of biological lipids are typically very weak, necessitating the use of labeled AuNS for characterizing receptor expression.

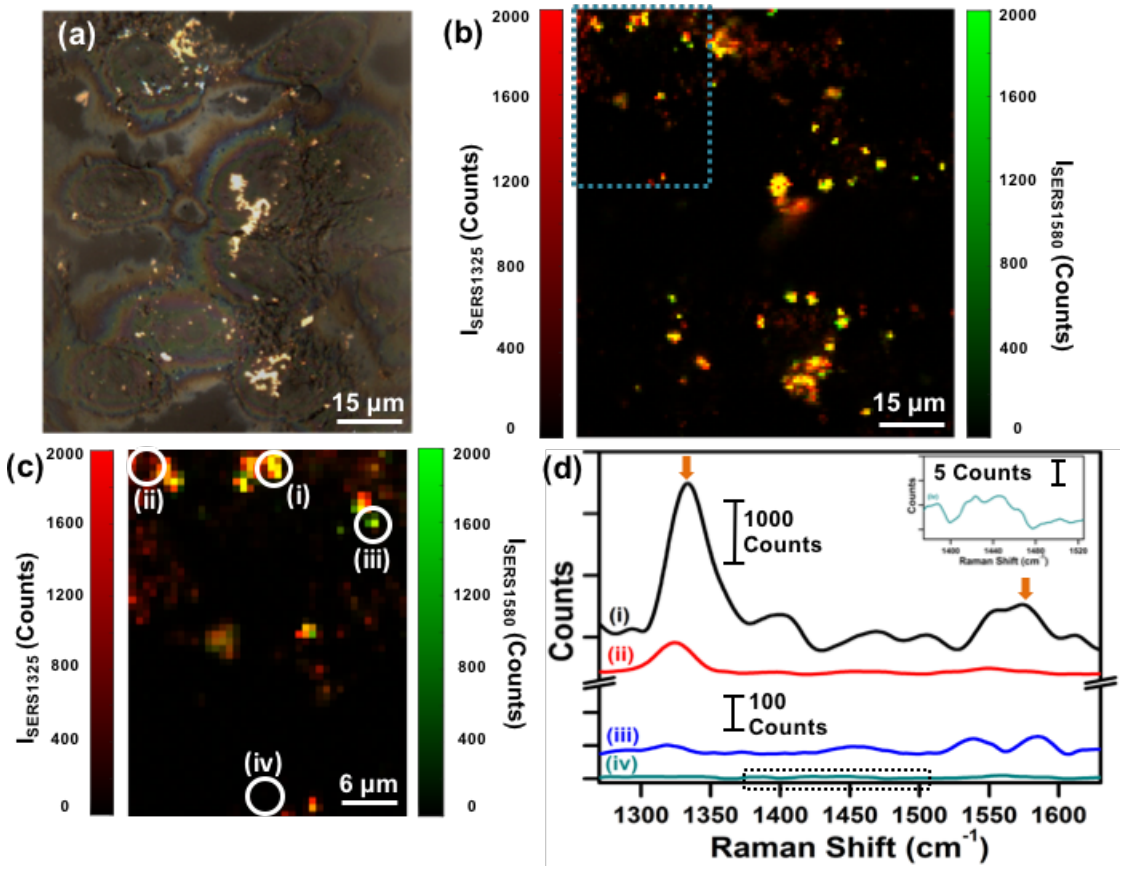

Figure 3.2 SERS multiplex mapping of MDA-MB-231cells with (1:1) mixture of antiEGFR-pMBA-AuNS to antiPDL1-DTNB-AuNS. (a) Brightfield image of cells after 16 h incubation provides coordinates for multiplex Raman map. (b) Overlap of spatial Raman intensity maps of both 1325 cm^{-1} peak for DTNB and 1580 cm^{-1} peak for pMBA, recorded at 0.75 µm steps. (c) Magnified view of the blue rectangular area from "b" shows Raman intensity plot of both $I_{SERS1325}$ and $I_{SERS1580}$ indicating a cellular "traffic map" with various points selected (d) demonstrating (i) signal from both probes, (ii) DTNB alone, (iii) pMBA alone, and (iv) no signal from probes or intracellular lipids (dashed box). Arrows denote peaks of interest, 1325 cm^{-1} peak for DTNB and 1580 cm^{-1} peak for pMBA.

Further, to demonstrate that the observed Raman signal results from specific binding of antibody-conjugated AuNS rather than due to clustering via non-specific binding, we performed a control study where 4 µg/mL monoclonal antiPDL1 (1 h, 37 °C) was introduced in cells to block the PD-L1 receptors prior to incubating with a 1:1 mixture of antiPDL1-DTNB-AuNS and antiEGFR-pMBA-AuNS (170 µg/mL). The brightfield image of the cells (Figure 3.3a) as well as a SERS map (Figure 3.3b) at every 0.75 µm step indicated that the blocking of receptors results in

significantly fewer AuNS binding to cells (Figure 3.3c). The multiplexed SERS "traffic map" presented for the experimental group (Figure 3.2b) and control group (Figure 3.3b) demonstrate that AuNS are both sensitive and specific in detecting biomarkers of cancer when conjugated with targeting moieties. In addition, SERS imaging provides a qualitative assessment of the distribution of both biomarkers in the cellular environment.

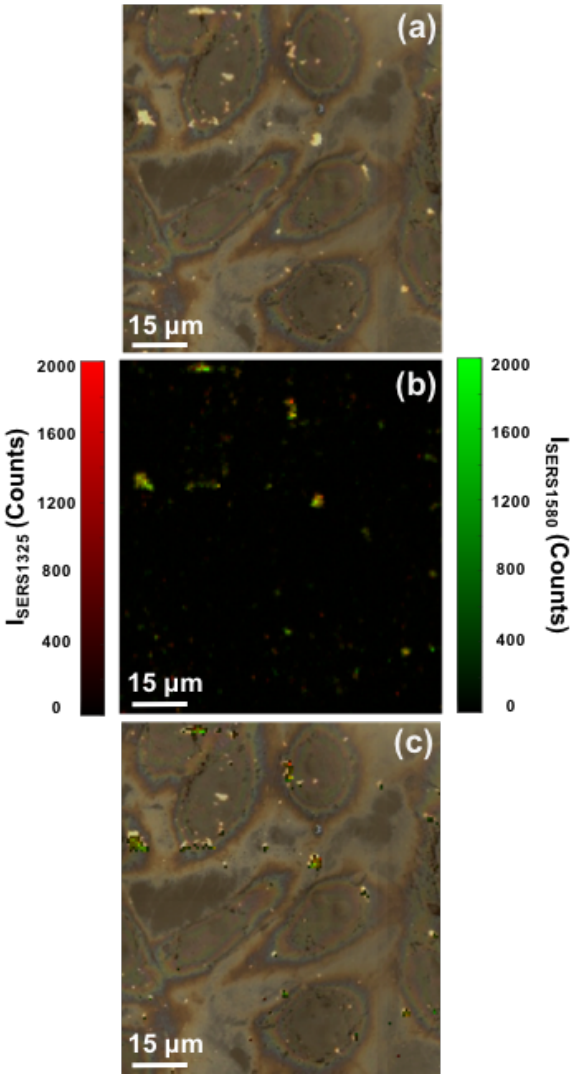

Figure 3.3 Blocking PD-L1 SERS multiplex mapping of MDA-MB-231 cells with (1:1) mixture (antiEGFR-pMBA-AuNS to antiPDL1-DTNB-AuNS). Cells were pre-blocked with monoclonal antiPDL1 for 1 h. (a) Brightfield image of cells after 16h incubation with (1:1) mixture provides coordinates for multiplex Raman map. (b) Overlap of spatial Raman intensity maps of both $I_{SERS1325}$ for DTNB and $I_{SERS1580}$ for pMBA recorded at 0.75 µm steps. (c) Overlap of brightfield and SERS map (both $I_{SERS1325}$ and $I_{SERS1580}$) to compare the effects of blocking on surface binding.

Multiplexed *in vivo* SERS was performed by administering the mixture of functionalized AuNS via retro-orbital injections to nude mice bearing MDA-MB-231 triple negative breast cancer xenografts. Whereas SERS-active nanoparticles have been commonly delivered *in vivo* via intratumoral[155, 160] or subcutaneous[159] delivery, we found systemic injection is necessary for tracking AuNS longitudinally to assess receptor status. Furthermore, systemic delivery is clinically-translatable enabling us to understand the uptake, biodistribution, and clearance of AuNS, and the overall sensitivity and specificity of our approach for multiplexed detection of biomarkers. We also note that whereas multiplexed *in vivo* SERS has been shown previously, longitudinal tracking of SERS-active nanoparticles at different time-points has not been effective.[153, 176] We performed SERS at 6, 12, 24, 48 and 72 h post AuNS delivery with a custom Raman setup described in the methods section.[177-178] The fiber optic Raman probe was gently placed on top of the mammary xenograft to acquire one second acquisitions with ten accumulations. A 785 nm continuous-wave laser was used at 80 mW and SERS measurements were obtained at five different spots on the tumor and the spectra were then averaged (Figure 3.4). The acquired Raman spectra were processed with fluorescence subtraction to remove biological auto-fluorescence and then normalized to the 1440 cm^{-1} biological peak. The 1440 cm^{-1} biological band (CH vibrations for both lipid and protein) has minimal change during time-course study in the same mouse shown in supporting information (Figure A. 3.2) serving as an excellent internal reference.

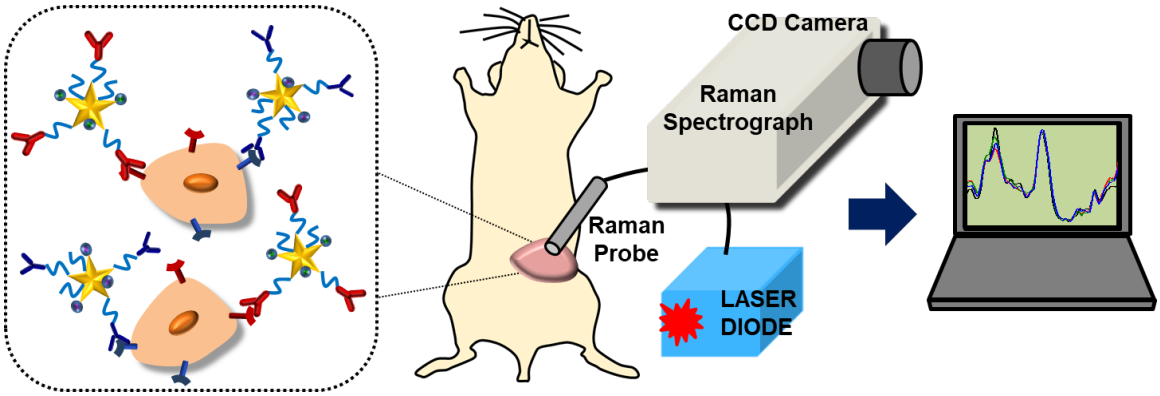

Figure 3.4 Schematic representation of *in vivo* SERS setup where nude mice bearing MDA-MB-231 xenografts were administered a mixture of antiEGFR-pMBA-AuNS and antiPD-L1-DTNB-AuNS via retro-orbital injections. A custom-built portable Raman setup was used for SERS measurement consisting of a 785 nm continuous-wave laser diode, a spectrograph, CCD camera, and fiber-optic probe.

To evaluate the changes in the intensity of Raman peaks, baseline Raman spectra of the tumor xenograft were also acquired immediately prior to the functionalized AuNS injection (0 h). Both signature peaks of DTNB (1325 cm^{-1}) and pMBA (1580 cm^{-1}) increased significantly and reached a maximum at 6 h post AuNS delivery as observed in our longitudinal study (Figure 3.5a). Averaged of five spectra across different locations of the tumor from each mouse (n=4 total mice) are shown in Figure A. 3.3. By tracking the Raman spectral features of DTNB and pMBA during time-course study, the simultaneous targeted detection of checkpoint ligand PD-L1 and biomarker EGFR is assessed *in vivo*. Maximum accumulation of AuNS occurs at ~ 6h, and between 48 h to 72 h both DTNB and pMBA signals returned to baseline levels (Figure 3.5b), indicating the clearance of AuNS via mononuclear phagocyte system of liver and spleen. To demonstrate both the sensitivity and specificity of functionalized AuNS in targeted detection of EGFR and PD-L1, we pre-blocked both biomarkers as our negative control. Prior work in the literature has effectively demonstrated that antibody dosage can successfully block receptors in mice tumors.[179-182] We injected 200 μg of monoclonal antibodies (anti-EGFR and anti-PD-L1) via intraperitoneal

injection (IP) 2h prior to injection of functionalized AuNS to saturate the surface receptors and block the binding of functionalized AuNS to these biomarkers. Longitudinal SERS comparing the experimental group with the control group tumors (Figure 3.5b-c) showed statistically significant differences in both PD-L1, corresponding to DTNB signal which decreased by 31% ($p < 0.0005$), and EGFR, corresponding to pMBA signal which decreased by 32% ($p < 0.0005$). The observed differences in SERS signal in longitudinal measurements between experimental and control groups demonstrate (1) the specificity of our approach in rapid and accurate targeted detection of PD-L1 and EGFR *in vivo*, and (2) the sensitivity of our approach as AuNS amplify the SERS signal of Raman reporters sufficiently to provide an assessment of receptor expression on tumor surface.

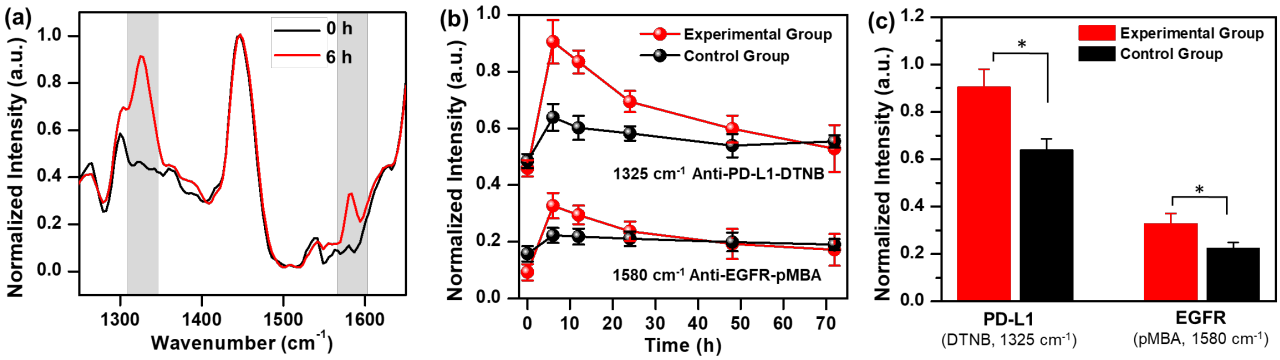

Figure 3.5 Multiplexed SERS longitudinal study. (a) Averaged, normalized Raman spectra of tumors (n=4) were plotted before (0h) and at maximum accumulation time point, 6h-post functionalized AuNS injection. The appearance of SERS signal of the signature peaks for both pMBA (1580 cm^{-1}) and DTNB (1325 cm^{-1}) are indicated by gray boxes. (b) Longitudinal SERS (n=4) performed at 6, 12, 24, 48 and 72 h post particle injections where pMBA and DTNB signals were normalized to 1440 cm^{-1} biological peak. In the control group both markers were pre-blocked with monoclonal antibodies 2h prior to delivery of functionalized AuNS. (c) SERS intensity comparison of experimental and control group tumors at 6h time-point showing that for both PD-L1 and EGFR detection, SERS signal decreased by ~30% ($p < 0.0005$) in the control group.

Multiplexed *in vivo* monitoring of PD-L1 and EGFR has several advantages over the current standard measure i.e. immunohistochemistry (IHC) of invasive biopsies. First, *in vivo* measurements track biomarker status of whole tumor lesions which reduces misinterpretation due

to inter- and intratumoral heterogeneity. Second, it allows monitoring of biomarker expression during the course of the disease minimizing the need for repetitive biopsies and patient discomfort. This is of particular clinical relevance as both PD-L1 and EGFR expression in patients are known to alter with prior treatments. Third, *in vivo* SERS enabled by systemic delivery of contrast agents such as functionalized AuNS takes into account multiple factors such as vascular permeability, blood vessel density, necrotic regions providing a more comprehensive assessment of PD-L1/EGFR expression than the qualitative "yes or no" type of information available through IHC. We are not suggesting *in vivo* SERS should replace IHC, which is a gold standard in clinical histopathology, but rather supplement IHC to obtain a more accurate and reliable prognosis enabling patient-tailored treatment strategies.

In vivo SERS is ideal for rapid molecular identification of biomarkers specifically for subcutaneous tumors where the penetration-depth of near-infrared light and detection of Raman scattering is less affected by the tissue characteristics. However, for clinical translation of this technology, SERS should benefit patients with both early-stage and late-stage cancer. Whereas current clinical pathology mostly relies on IHC, it is inherently subjective, often misinterpreted when presented with highly heterogeneous tumors, and limited in multiplexed validation of multiple biomarkers in the same biopsy. Other *ex vivo* techniques, such as immunofluorescence (IF), have enabled quantitative assessment of biomarkers; however, tissue autofluoroscence and rapid photobleaching of commonly used fluorescent tags make this approach unreliable. Therefore, in addition to *in vivo* SERS imaging, here we show that *ex vivo* Raman maps of tumor sections is a powerful approach combining high spatial and temporal resolution, and address some of the current challenges with IHC and IF.

Tumors were retrieved at the maximum accumulation time-point (6h post AuNS delivery), cryo-fixed, sectioned at 5 µm thickness, and transferred to calcium fluoride (CaF_2) disks to minimize Raman signal from the substrate. A brightfield image of the tissue was recorded (Figure 3.6a) to show tumor sections retain their morphology on CaF_2 disks. We performed SERS maps of an entire tissue section at 50 µm step size (50 µm in both x and y direction), providing near cellular-level resolution. The tissues were excited with a 785 nm laser at 30 mW using a 50x objective with 10 s acquisitions. SERS spectra were processed to remove cosmic rays, subtract tissue autofluorescence, and subsequently intensities of DTNB and pMBA were plotted such that each pixel generated a color map assigned with an RGB color - red for DTNB (1325 cm^{-1}) and green for pMBA (1580 cm^{-1}) (Figure 3.6b).

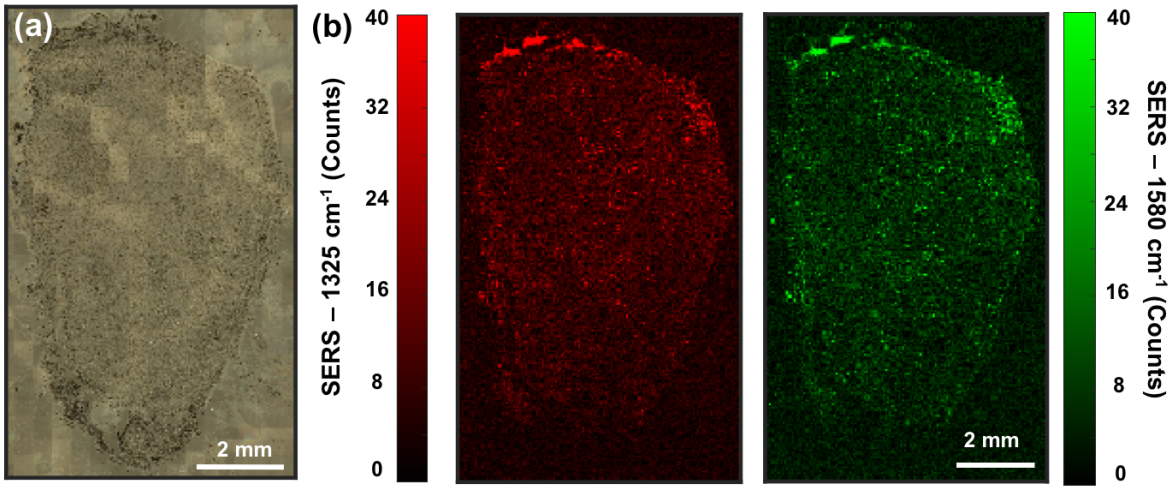

Figure 3.6 *Ex vivo* Raman mapping of MDA-MB-231 tumor xenograft. Tumor was collected 6 h post functionalized AuNS injection. Raman mapping was done at 50 µm x 50 µm per pixel. (a) Birghtfield imaging of the tissue. (b) The intensity map of anti-PDL1-DTNB-AuNS at 1325 cm^{-1} (left) is assigned with red while the intensity map of anti-EGFR-pMBA-AuNS at 1580 cm^{-1} (right) is assigned with green.

The intensity map shown in Figure 3.7a provides an overview of localization of the functionalized AuNS, antiEGFR-pMBA-AuNS and antiPD-L1-DTNB-AuNS, where the signal from each Raman tag can be correlated to the respective biomarkers targeted. We then identify

regions of interest (Figure 3.7ai, ii) in the spatially-resolved Raman map of the tissue to qualitatively assess biomarker status. High magnification SERS maps (Figure 3.7b) show near cellular-level resolution of tumor areas that are PD-L1 rich (Figure 3.7bii-2), EGFR rich (Figure 3.7bii-3), rich in both biomarkers (Figure 3.7bii-4), as well as likely necrotic areas where AuNS did not accumulate (Figure 3.7bi-1, no signal). The corresponding SERS spectra from these regions of interest confirm the biochemical footprint of PD-L1 and EGFR targeted AuNS distribution (Figure 3.7c).

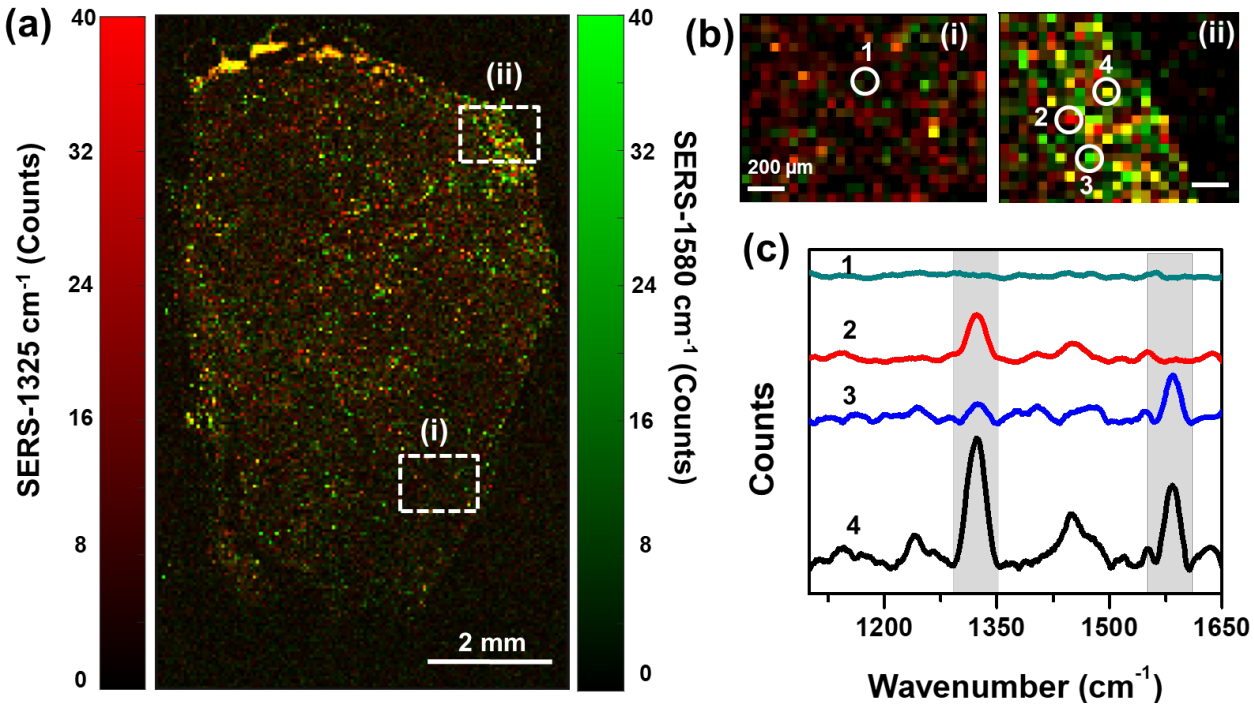

Figure 3.7 *Ex vivo* Raman spatial maps of breast cancer tumor sections. (a) SERS intensity map of the entire tissue section performed at 50 µm per pixel showing an overlap of both DTNB (1325 cm^{-1}) and pMBA (1580 cm^{-1}) signals. Specific regions of interest (ROI) are indicated. (b) High magnification SERS intensity map from the ROIs indicated in 'a' showing (i) tissue region with minimal AuNS accumulation and no Raman signal, (ii) tissue region with high AuNS accumulation indicating PD-L1 and EGFR expression. (c) Corresponding Raman spectra indicating (1) no AuNS binding, (2) PD-L1 rich area, (3) EGFR rich area, and (4) both EGFR and PD-L1 rich area (DTNB and pMBA signature peaks are indicated by grey boxes).

Nanoparticle accumulation in tumors through surface receptor binding and through the EPR effect is known to occur in well-vascularized areas.[183-185] Therefore, by comparing the Raman

intensities of both DTNB and pMBA in the tissue maps to the vascular density, we demonstrate the accuracy of our approach where functionalized AuNS should accumulate in the high vascular density areas with high SERS intensity. Conversely, low accumulation of AuNS is attributable to poorly vascularized or necrotic regions of the tumor which should correspond to low SERS intensity. We generated a SERS distribution map (Figure 3.8a-c) using the 1440 cm^{-1} biological peak, which remains constant throughout the tumor, to obtain a tissue mask. This mask blocks out all the empty/no-tissue areas (Figure A. 3.4a) and enables generation of Gaussian distributions of both DTNB (1325 cm^{-1}) and pMBA (1580 cm^{-1}). By fitting the biological peak intensities (1440 cm^{-1}) throughout the tumor with two Gaussian functions, low (Figure A. 3.4b) and high (Figure A. 3.4c) Raman intensity regions were generated with high confidence (R^2 = 0.995). Tissue sub-masks of high and low SERS intensity regions of DTNB and pMBA were then generated by setting a threshold and by fitted using the two Gaussian functions. A 2-dimensional (2D) Gaussian filter (sigma = 20 μm) was also applied to prevent any extreme pixels for biased results. By applying the tissue sub-masks to the DTNB Raman signal map, low (Figure 3.8a top), high (Figure 3.8b top), and combined (Figure 3.8c) SERS distribution maps were generated with good fits to the distribution of the SERS signal (R^2 = 0.983 for high intensity, and R^2 = 0.999 for low intensity). These high and low SERS intensity maps are useful in visualizing regions of the tissue to assess their state of angiogenesis or necrosis. Vascular staining was performed with endothelial cell marker CD31 to confirm the degree of angiogenesis in the tumor tissue and correlate to the SERS intensity of DTNB and pMBA which directly corresponds to AuNS accumulation. We observed that high SERS intensity areas correlate strongly to well-vascularized areas where the blood vessels are indicated by arrows in Figure 3.8b bottom. However, low SERS signal regions of the tissue did not have abundant vascular density (Figure 3.8a bottom) clearly indicating that AuNS

accumulation and resulting SERS signal overlaps with the vascular density of the tumor. SERS intensity distribution maps for pMBA present similar results as the DTNB maps (Figure A. 3.5). The spatial information provided by the Raman maps enables us to provide a quantitative assessment of biomarkers to understand the heterogeneity of receptor expression both inter-and intra-tumorally. We retrieved n = 3 mouse tumors at maximum accumulation time-point (6h post AuNS injection) and performed SERS mapping and obtained the mean intensity of DTNB and pMBA for each tumor section to generate low and high signal areas corresponding to low and high accumulation of AuNS. The quantitative (Figure 3.8d) assessment of functionalized AuNS distribution shows (i) there is a significant difference between the SERS intensity in high vascularized and low vascularized areas, but (ii) there is no significant difference in expression between EGFR or PD-L1 receptor throughout this tumor. This is expected as both EGFR and PD-L1 are in abundance in MDA-MB-231 cells and differences in expression levels in individual tumor sections cannot be easily detected.

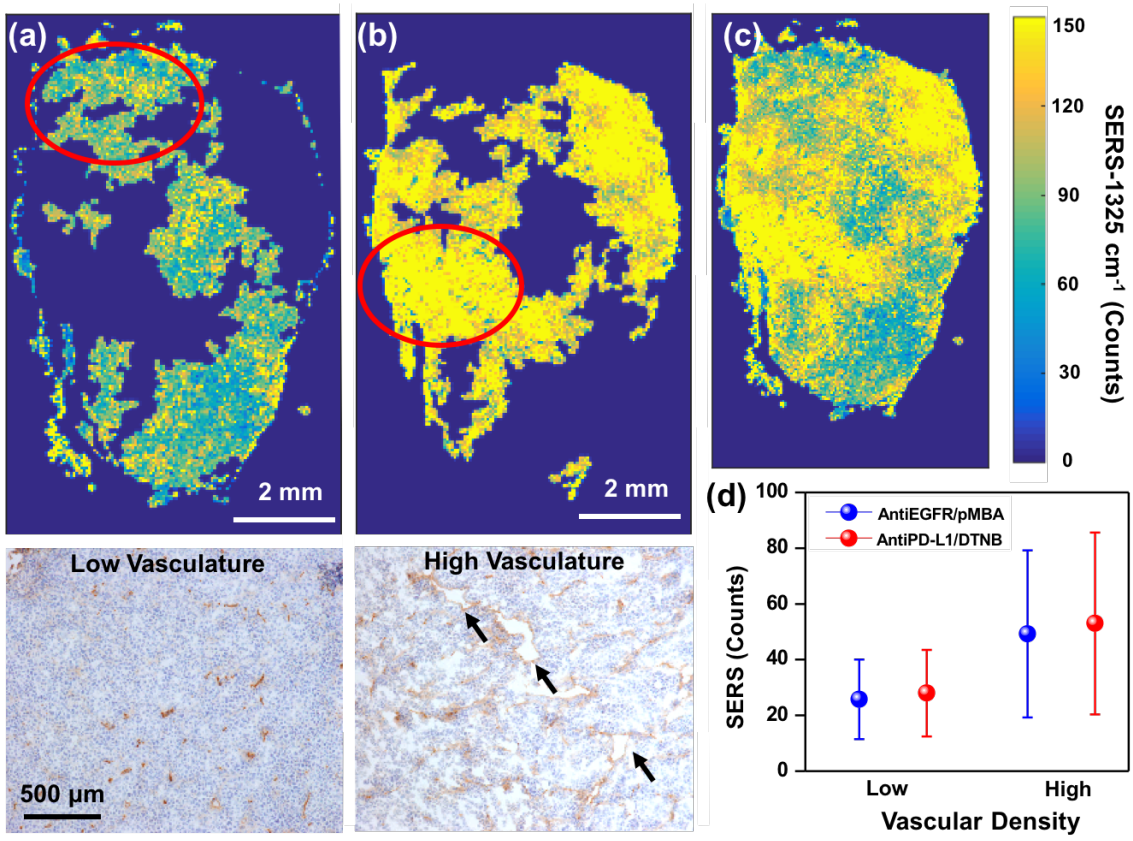

Figure 3.8 Analysis of receptor status via Raman spatial maps of tumor sections at 1325 cm^{-1} corresponding to antiPD-L1/DTNB/AuNS. (a) Low SERS intensity map and corresponding CD31 staining (bottom) of the circled area showing poorly vascularized area of the tissue. (b) High SERS intensity map and corresponding CD31 staining (bottom) of the circled area showing high vascular density. The micro vessels are indicated by the black arrows. (c) Overlay of (a) and (b) provides an overall SERS spatial map. (d) Quantitative assessment of both antiPD-L1/DTNB/AuNS and antiEGFR/pMBA/AuNS in low and high vascularized areas.

The SERS maps of tumors *ex vivo* provides ***(i)*** a qualitative assessment of both PD-L1 and EGFR confirming multiplexed biomarker status in the same tissue section, which cannot be assessed with IHC; ***(ii)*** a distribution map of functionalized AuNS accumulation in the tumor that can be strongly correlated to the vascular density indicating the high accuracy of our approach and that AuNS localize in well-vascularized areas through both receptor-mediated endocytosis and EPR effect; ***(iii)*** spatially-resolved quantitative analysis of both PD-L1 and EGFR expression levels in the same tissue section that allows us to determine heterogeneities in receptor status; and

finally ***(iv)*** SERS provides a highly reliable approach for both *in vivo* and *ex vivo* measurement since it is undeterred by tissue autofluorescence or photobleaching, which typically plagues IF-based methods. These collective attributes of SERS mediated by immunoactive AuNS will ultimately enable patient-selection for PD-L1 checkpoint blockade as well as identify those who will respond to combination PD-L1/EGFR treatment to improve breast cancer patient outcome, as well other cancers where these biomarkers are upregulated.

We performed histochemical analysis of tumor sections to understand the biocompatibility of functionalized AuNS *in vivo*. Haemotoxylin and Eosin (H&E) staining of the tumor sections both with and without functionalized AuNS was also performed to ensure the biocompatibility of AuNS (Figure 3.9). H&E identified that the cellular morphology of tumor tissues did not have any detrimental effect in the presence of AuNS indicating that they are nontoxic to cells.

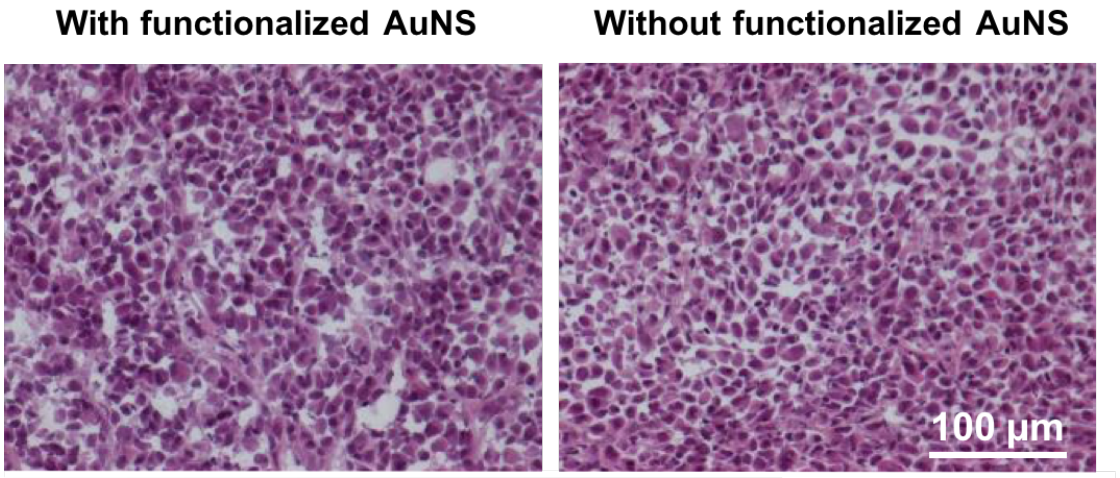

Figure 3.9 Haemotoxylin and Eosin (H&E) staining of MDA-MB-231 tumor xenograft with (left) and without (right) functionalized AuNS administration. The results show the morphology of tumor does not change with functionalized AuNS indicating the particles themselves are not detrimental to biological tissues.

Silver enhancement stains of tissue were performed which allows visualization of AuNS as gold selectively catalyzes the reduction of silver ions and deposits metallic silver which embeds the AuNS in kidney sections visible under a light microscope. The dark spots in tumor sections

from the experimental group indicate the presence of functionalized AuNS bound to the cell surface, not present in tumors without AuNS (Figure 3.10a).

Quantitative longitudinal analysis of biodistribution of nanoparticles in tissue after systemic delivery is necessary to evaluate their pharmacokinetics, uptake in tumor relative to other tissues, and their stability and potential toxicity *in vivo*. We studied the bioavailability and clearance of functionalized AuNS with inductively coupled plasma mass spectroscopy (IC-PMS) to measure the Au content in tumors and major organs at 6 h (maximum accumulation) and 72 h after IV delivery of AuNS (Figure 3.10b). Acid digestion method was used to dissolve gold in the tissues into the solution for mass spectroscopy reading. At both 6 h and 72 h, very few gold amounts were found in the stomach (2.8 ± 1.4), heart (5.2 ± 3.0) and lungs (4.0 ± 3.5). Minimal amounts of Au was found in the brain (0.5 ± 0.6) since the blood brain barrier does not allow entry of functionalized AuNS.[186-187] The majority of gold content was found in both mononuclear phagocyte system (MPS) organs at 72 h, spleen (724.6 ± 156.2) and liver (142.4 ± 60.9). There is significantly higher Au content in spleen at 72 h (724.6 ± 156.2) relative to 6 h (210.9 ± 88.3) which is statistically significant ($p<0.05$), demonstrating AuNS mostly clears through the spleen. Clearance of nanoparticles through MPS is not surprising and has been reported previously for other gold nanoparticles.[188-191] The presence of Au in kidneys (20.7 ± 6.7) was minimal since nanoparticles >10 nm are less likely to have renal clearance via glomerular filtration in mice.[192-194] However, deviation to this trend has been observed previously where PEG coated Au nanoparticles were targeted to the mesangium of the kidney, the thin membrane of cells that supports glomerular capillaries, and accumulation in kidneys was observed for ~75 nm nanoparticles.[195] The nanoparticle morphology, including size, shape, and aspect ratio, has been shown to play a strong role in their clearance pathways, where anisotropic nanostructures with

optimized aspect ratio have been shown to have renal clearance.[196-198] Whereas clearance of AuNS through the MPS is expected in mice, this should not hinder clinical translation of AuNS as sub-micron and micron-sized particles have been shown to have renal clearance through the kidney in large animals and humans.[199-200] We also compared the Au content in tumors from the experimental group with the pre-blocked control tumors at maximum accumulation time-point (6 h post functionalized AuNS injection) and observed statistically significant differences in Au content ($p<0.05$) (Figure 3.10c). Moreover, significantly higher AuNS uptake was observed at the maximum accumulation time (6h) than at the end of the study (72h) for the experimental group ($p<0.05$). The differences in AuNS content indicates the clearance of AuNS at the end of the study. The trends observed in IC-PMS correlate well with our *in vivo* endpoints where a significant difference in Raman signal was detected at 6h time-point and rapid decrease in signal was observed by 72h. Lastly, AuNS content in major organs were also compared between the experimental group with the pre-blocked control at the end of the study and no significant difference was found (Figure A. 3.6).

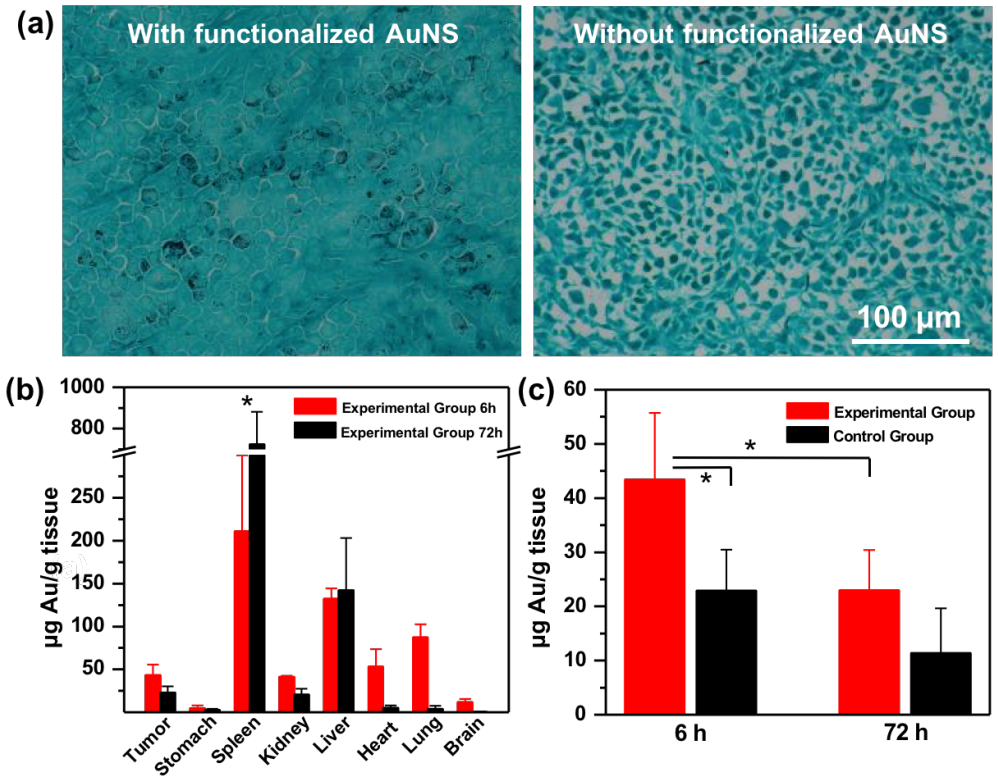

Figure 3.10 Biodistribution of AuNS functionalized with Raman tags, antibodies, and PEG. (a) Silver enhancement stain showing AuNS accumulation in tumors vs. tumors that did not receive AuNS. (b) IC-PMS results of Au content in tumor and major organs at 6 h (n=3) and 72 h (n=4) post IV delivery of functionalized AuNS showing AuNS presence in tumor and in the mononuclear phagocyte system. The difference in Au content of spleen at 6 h and at 72 h is statistically significant ($p<0.05$). (c) IC-PMS analysis of AuNS accumulation in tumors compared at 6 h and 72 h. Differences in Au content between experimental and control groups was statistically significant for tumors retrieved at 6h post AuNS delivery ($p<0.05$).

Further, we obtained transmission electron microscopy (TEM) images of tumors and major organs to understand the internalization and localization of functionalized AuNS in the tumor microenvironment and in MPS of liver and spleen (Figure 3.11). Tumor xenografts were retrieved at 6h post AuNS delivery *in vivo*, then fixed and sectioned for TEM imaging. Functionalized AuNS were observed in intracellular vesicles in the tumor but were not found in the mitochondria, the nucleus, or other cellular organelles. AuNS uptake and internalization in tumors is facilitated both by the EPR effect as well as receptor-mediated endocytosis enabled by targeting antibodies on the

AuNS surface.[170, 201-203] Liver and spleen were retrieved at the end of the study i.e. 72h time-point. Functionalized AuNS were found in the Kupffer cells of the liver and macrophages of the spleen. Nanoparticle uptake in Kupffer cells and macrophages have been previously reported in the literature.[204-208] In addition, AuNS were also found in lysosome-like structures within the macrophages, indicating endocytosis was the major mechanism for particle uptake. Lastly, we also retrieved the mouse hearts at the end of the study and did not find any AuNS which corroborates literature findings that gold nanoparticles cannot penetrate through the continuous endothelium cells in the arteries.[209-211] Notably, TEM images also clearly demonstrated that the functionalized AuNS maintained their structural and morphological integrity after IV delivery.

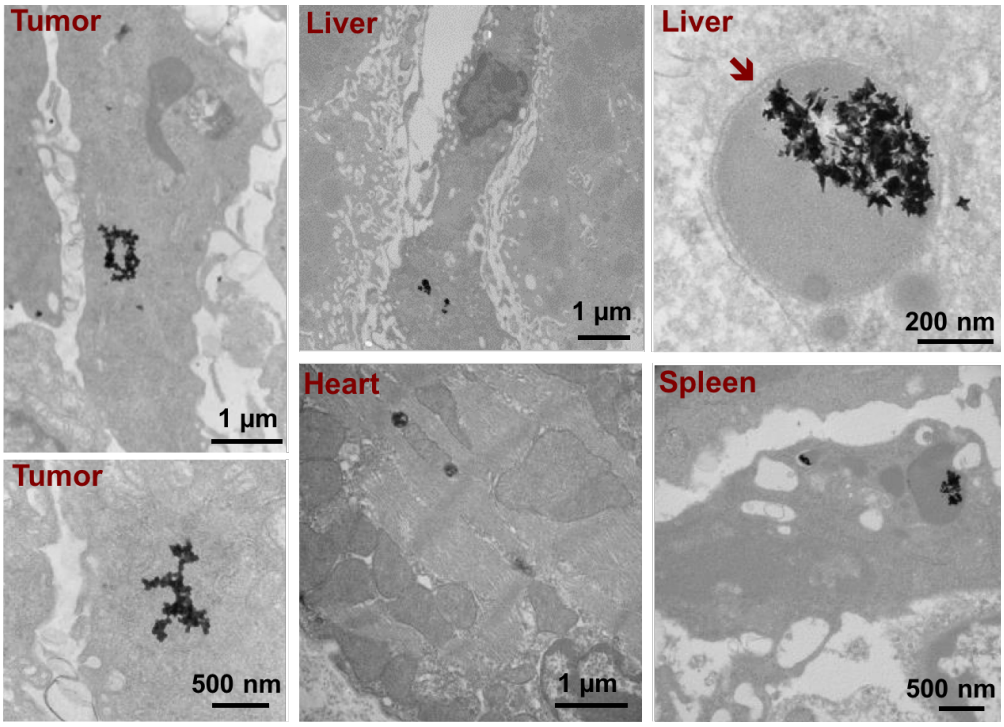

Figure 3.11 Transmission electron micrographs showing accumulation of functionalized AuNS in breast cancer tumors and major organs. The functionalized AuNS maintained their structural integrity after circulation in the body and were found in the tumor, in macrophages of the spleen, and in Kupffer cells of the liver via intracellular vesicles (indicated by the red arrow). Functionalized AuNS were not observed in the heart of the mouse.

3.5 Conclusion

In summary, in this work we demonstrate the utility of AuNS labeled with Raman tags and antibodies to diagnose immunomarker PD-L1 and concurrently detect EGFR in MDA-MB-231 breast cancer tumors *in vivo* and *ex vivo* with noninvasive surface-enhanced Raman spectroscopy (SERS). Tracking of AuNS *in vivo* provide a longitudinal analysis of AuNS accumulation in tumors and simultaneous detection of PD-L1 and EGFR. Furthermore, SERS spatial maps of tumor sections *ex vivo* showed excellent correlation of AuNS distribution to vascular density, and enabled both qualitative and quantitative assessment of biomarker status in tumors. The bioavailability and clearance of AuNS was evaluated both with IC-PMS and TEM imaging which revealed AuNS accumulate in the tumors likely via receptor-mediated endocytosis and cleared by MPS. This study highlights the potential of SERS with dose-controlled AuNS to transform the diagnosis of cancer patients and enable patient-tailored immunotherapies. We anticipate that early monitoring with SERS will allow practitioners to determine the optimal treatment regimen of single checkpoint blockade or combination therapies to enable remission-free survival. Since PD-L1 and EGFR upregulation has been correlated to many cancers including non-small cell lung, renal, and colon cancer, multiplexed SERS with AuNS will also benefit patients beyond breast cancer. The utility of SERS as both a powerful *in vivo* and *ex vivo* diagnostic tool will ultimately eliminate the need for unpredictable immunohistochemistry, and allow assessment of multiple immunomarkers within the same biopsy, minimizing repeated invasive procedures and patient discomfort. We expect this work will enable a path forward to clinically translate engineered gold nanostructures for both detection of immunomarkers and for therapeutic delivery of immunomodualtors and vaccines.[14-15, 34, 212]

3.6 Appendix

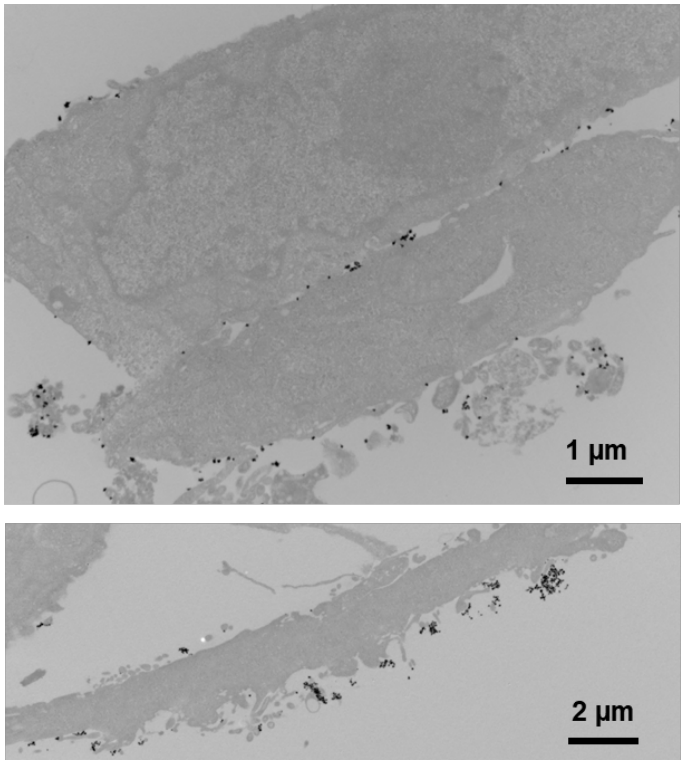

Figure A. 3.1 TEM images of MDA-MB-231 incubated with functionalized AuNS for 16 h. AuNS were bound to the surface of the cells via receptor-antibody interactions.

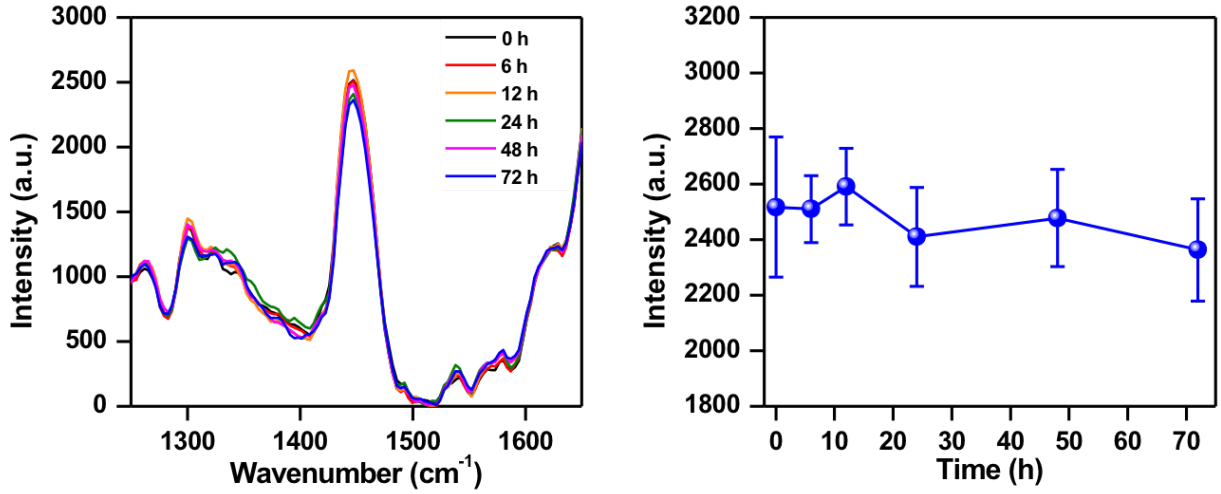

Figure A. 3.2 Raman spectra of tumor xenograft without functionalized AuNS injection showing the intensity of the lipid peak (1440 cm^{-1}) remains consistent over time.

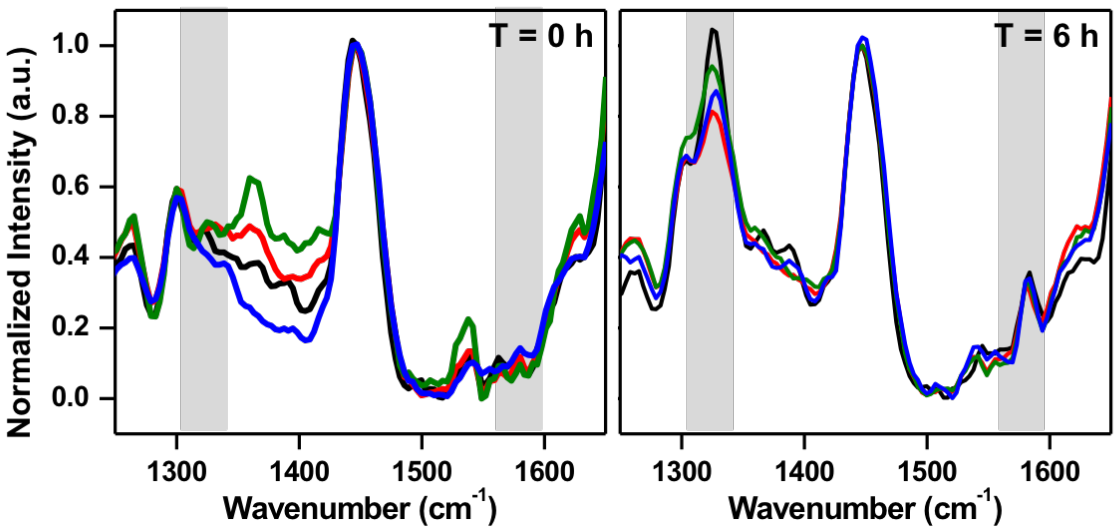

Figure A. 3.3 Mammary tumor xenografts were imaged before functionalized AuNS injection (0 h). Each color indicates averaged Raman spectrum of a single mouse (n=4). Both DTNB (at 1325 cm^{-1}) and pMBA's (at 1580 cm-1) signature peaks, indicated by the grey box, were not observed at 0 h. Mice were then injected with 1.2 mg of a 2:1 mixture of anti-EGFR-pMBA-AuNS and antiPD-L1-DTNB-AuNS. The tumors were imaged at 6 h post particle injection.

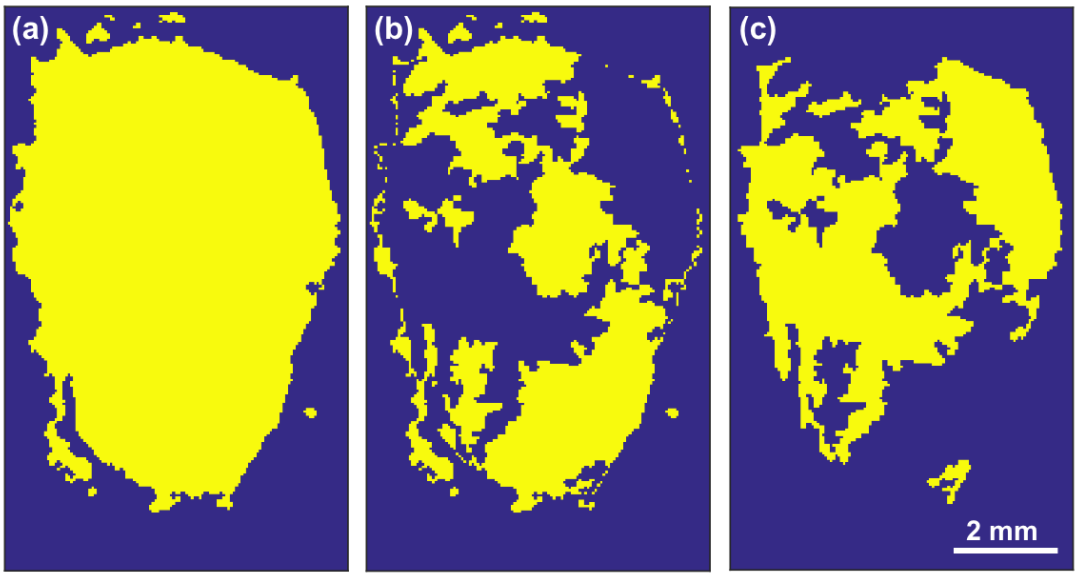

Figure A. 3.4 (a) Tissue mask and (b, c) sub-masks of the lipid peak at 1440 cm^{-1} were used to quantify *ex vivo* mapping.

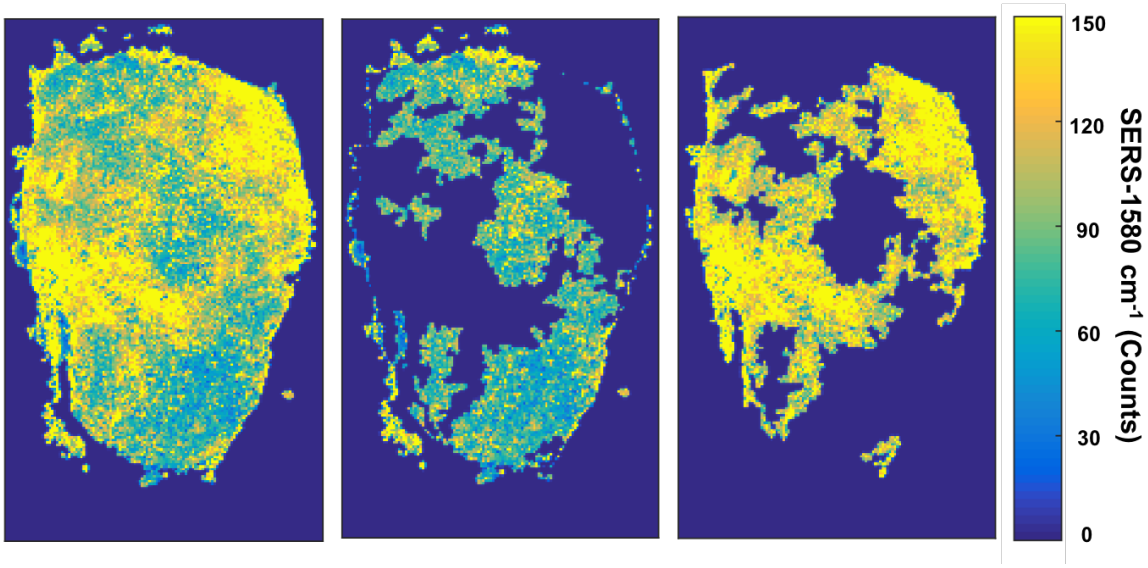

Figure A. 3.5 Quantitative analysis of *Ex vivo* Raman mapping at 1580 cm^{-1} (pMBA).

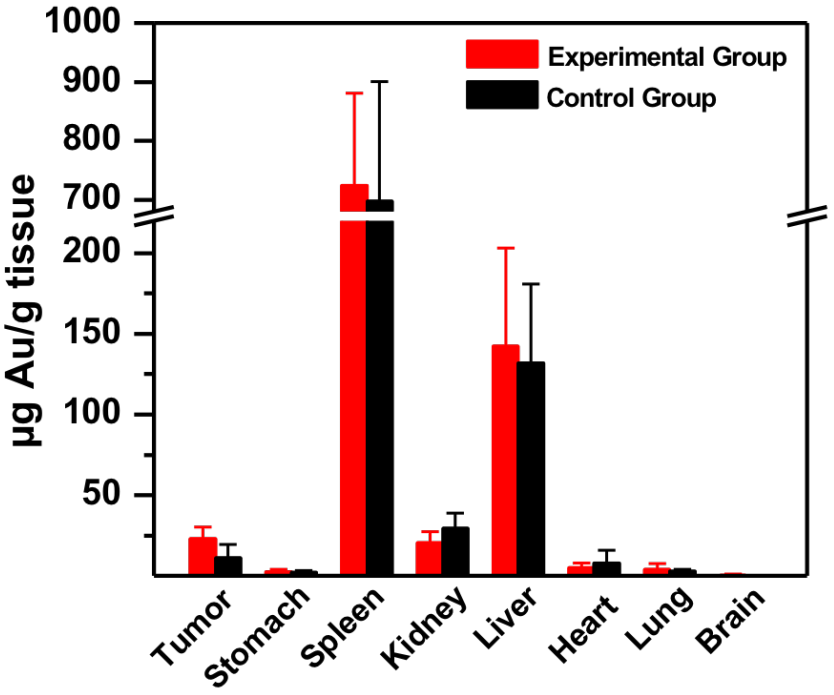

Figure A. 3.6 Biodistribution of AuNS functionalized with Raman tags, antibodies, and PEG at the end of the study, 72 h time point in experimental group mice (n = 4). The control group (n=3) was pre-blocked with IP delivery of anti-EGFRa + anti-PD-L1a prior to functionalized AuNS injection.

Chapter 4

MULTIMODAL MULTIPLEXED IMMUNOIMAGING WITH GOLD NANOSTARS FOR DETECTION OF IMMUNOMARKERS AND TO MONITOR RESPONSE TO IMMUNOTHERAPIES

4.1 Summary

Checkpoint blockade immunotherapy has driven a paradigm shift in the treatment of melanoma. Immunohistochemistry (IHC) is currently the gold standard to predict checkpoint receptor expression; however, IHC requires the collection of invasive biopsies, and the results are often biased due to tumor heterogeneity. This underscores the critical need for accurate, noninvasive diagnostic tools that can identify immunomarkers that engage in tumor microenvironment (TME) to enable patient-tailored immunotherapies. Our lab developed a multimodal imaging platform to simultaneously detect programmed death ligand 1 (PD-L1) on tumor cells and CD8 on T cells. By combining positron emission tomography (PET) with surface-enhanced Raman spectroscopy (SERS) using gold nanostars (AuNS), depth-resolved whole-body imaging can be achieved with spatiotemporal resolution. AuNS were functionalized with radioactive isotope Cu64, PD-L1 and CD8 antibodies, and corresponding Raman molecules (anti-PD-L1 with pMBA and anti-CD8 with DTNB). PET images showed high tumor-to-muscle ratio in signal, indicating the specificity of the AuNS. Strong increases in SERS signals for both Raman tags corresponding to PD-L1 and CD8 antibodies were also observed. Furthermore, using AuNS and PET/SERS, responses to immunotherapy can be monitored by tracking changes in PD-L1 and CD8 levels. Mice treated with CD137 and PD-L1 antibody combination therapy were imaged. DTNB signal corresponding to CD8 expression was increased threefold after the therapy, indicating the success of CD8+ T cell infiltration into TME. We showed the combination of PET and SERS with AuNS can not only accurately identify PD-L1 and CD8 expression for

immunotherapy patient selection, but also provide accurate prediction on responses to immunotherapy.

4.2 Introduction

Upregulation of immune checkpoint programmed cell death protein-1 (PD-1) and subsequent binding of PD-1 to its ligand, PD-L1, impedes effector T cell function contributing to immunosuppression.[133, 213] Inhibition of the PD-1/PD-L1 axis with immunotherapies has recently transformed the therapeutic landscape for a broad array of cancers. However, despite the clinical activity of these agents, only a fraction of patients respond in most tumor types and identifying patients likely to benefit from these therapies remains challenging.[214-216] Current predictive technologies rely on static measure of PD-L1 status in biopsies which cannot adequately distinguish responders from nonresponders. This could be in part due to limited tissue sampling or the spatial and temporal heterogeneity of PD-L1 among patients, and within the same patient's primary and metastatic lesions.[217-219] Therefore, noninvasive molecular imaging is critical in the immunotherapy drug development pipeline to (i) enable accurate and dynamic measure of PD-L1 status *in vivo* and identify those who will respond to immunotherapies even before treatment begins, (ii) allow multiplexed recognition of other immunomarkers that show engagement of the immune tumor microenvironment (TME) to determine alternative therapies for nonresponders, and (iii) establish new surrogate end points for monitoring treatment efficacy early in the immunotherapy regimen and reflect the dynamic changes in immunomarker localization during therapeutic intervention.[220-222]

The dynamic profiling of both PD-L1 and cytotoxic $CD8^+$ T cells *in vivo* is highly relevant both pre- and post-treatment to predict the complex interplay between the immune system and

TME. $CD8^+$ activated T cells both within the tumor and at the invasive margin is a positive prognostic marker and demonstrate active engagement of antitumor immunity.[223-225] Studies have shown tumors infiltrated with $CD8^+$ T cells and expressing PD-L1 are most likely to benefit from PD-L1 blockade.[226-227] The strong correlation between PD-L1 inhibition, and $CD8^+$ activation of T cells motivates multiplexed detection of both markers to ultimately provide translatable methods for predicting clinical responses to immunotherapies.

In this work, we simultaneously detect both PD-L1 and CD8 *in vivo* (Figure 4.1a) and monitor response to checkpoint blockade with an innovative probe, immunoactive gold nanostars (AuNS), which combine positron emission tomography (PET) with surface-enhanced Raman spectroscopy (SERS). PET and SERS are complimentary imaging techniques seamlessly integrated with AuNS, allowing depth-resolved whole-body imaging with PET to locate the macroscopic distribution of tumors to tissue depths of many centimeters. This is followed by multiplexed detection with SERS identifying immunomarkers that dynamically control local and systemic immunity in the TME. We have shown SERS enables quantitative biomarker screening where gold nanostars amplify the signal of Raman molecules by 10^9 allowing high signal-to-noise data and enhanced spatiotemporal resolution.[63] Our group has also shown multiplexing with SERS *in vitro* and *in vivo* is facilitated by the narrow linewidths of vibrational signature of Raman tags allowing minimal spectral overlap.[169, 228] Further, the straightforward surface chemistry of gold allows to conjugate multiple molecules on AuNS surface. Here we show AuNS labeled with antibodies, Raman tags, and ^{64}Cu radiolabel honed in the tumors after systemic delivery *in vivo* in immunocompetent tumor-bearing mice. AuNS detected both PD-L1 expressing tumor cells and $CD8^+$activated T cells simultaneously in the TME with high specificity and sensitivity. Further we demonstrate AuNS are effective in monitoring response to immunotherapy in mice treated with

combination antiPD-L1+antiCD137 mAbs. CD137 is a costimulatory receptor expressed on activated T cells and shown to have synergistic therapeutic benefits with PD-L1 blockade.[229-230] ImmunoPET-SERS with AuNS demonstrated both inhibition of PD-L1, and infiltration of $CD8^+$ T cells into tumors of treatment mice that correlated well with decrease in tumor growth. Immunohistochemistry (IHC) analysis of tumors confirmed CD8+ expansion in treatment mice relative to control mice that received isotype-matched IgG mAbs. We envision the findings of this work will enable a clinically translatable technology that will ultimately enable image guided interventions ranging from noninvasive treatment planning to predicting therapeutic effectiveness to allow remission-free survival of cancer patients.

4.3 Materials and Methods

4.3.1 Synthesis of Gold Nanostars (AuNS)

AuNS were synthesized with a biological buffer, (4-(2-hydroxyethyl)-1-piperazineethanesulfonic acid) (HEPES) though a one-step and seedless mediated method that was previously described by our group. Briefly, 18 ml of ultrapure water at 18 MΩ was added to 12 ml of 270 mM HEPES buffer at pH 7.40 ± 0.2. Next, 300 μL of 20 mM chloroauric acid was added. The solution was then mixed by gentle inversion and reacted for 75 minutes at room temperature. Both AuNS synthesis materials, gold(III) chloride trihydrate (HAuCl4), and HEPES were purchased from Sigma-Aldrich.

4.3.2 Functionalization of AuNS

Raman tags, 4-mercaptobenzoic acid (pMBA) and 5,5'-Dithiobis(2-nitrobenzoic acid) (DTNB) were purchased from TCI America. Bifunctional linker, orthopyridyl-disulfide poly(ethylene glycol)-N-hydroxysuccinimide ester (OPSS-PEG-NHS ester, M_w 2000) was

purchased from JenKem Technology. To conjugate Raman tags to the AuNS surface, 6 µL of 10 mM pMBA or DTNB (in 100% ethanol) were added to 60 mL of AuNS and reacted for 15 minutes at 4 ^{0}C. To remove excess Raman tags, the AuNS was centrifuged at 6000 rpm for 10 minutes. To functionalize targeting antibodies to AuNS, OPSS-PEG-NHS ester linkers were first reacted with anti-PD-L1 (Bio X Cell, clone 10F.9G2) and anti-CD8 (Bio X Cell, clone 53-6.7) antibody. Briefly, 8 µL of 80 mg/ml OPSS-PEG-NHS was added to 72 µL of 1 mg/mL antibody and allowed to react in 100 mM pH 8.4 ± 0.1 sodium bicarbonate ($NaHCO_3$) buffer at 4 °C for 24 h. After, 80 µL of OPSS-PEG-anti-CD8 or OPSS-PEG-anti-PD-L1 was then added to 6 ml of Raman-labeled-AuNS at 1.14 mg/mL. The AuNS solution was then mixed on an inverter for another 24 h. Next, to conjugate chelator, 1,4,7,10-Tetraazacyclododecane-1,4,7,10-tetraacetic acid (DOTA) to gold, OPSS-PEG-NHS ester linkers were reacted with 1.4 mg of DOTA-amine (Macrocyclics) at 1 : 1 ratio for 10 hours. OPSS-PEG-DOTA was then reacted with AuNS for 12 h. Lastly, the fully functionalized AuNS (anti-PD-L1-pMBA-AuNS or anti-CD8-DTNB-AuNS) were centrifuged at 4000 rpm for 10 minutes twice and resuspended at a concentration of 5 mg/ml.

4.3.3 Characterization of Functionalized AuNS

The plasmon resonance of 1.5:1 mixture of anti-PD-L1-pMBA-AuNS and anti-CD8-DTNB-AuNS was measured with a Varian Cary 5000 UV-Vis NIR spectrophotometer. The size and shape of AuNS were visualized with an Osiris transmission electron microscope (TEM) at 200 keV. The Raman spectra of AuNS mixture at 1.5:1 (anti-PD-L1-pMBA-AuNS and anti-CD8-DTNB-AuNS) was obtained with a custom Raman setup with a 785 nm laser at 80nW. A Malvern Nano ZS dynamic light scattering apparatus was used to measure both the hydrodynamic size and the zeta potential of AuNS before and after functionalization.

4.3.4 YUMM 2.1 Xenograft Model and in vivo Multimodal Multiplexed Imaging

YUMM 2.1 cells were provided by Dr. Ann Richmond (Vanderbilt University Medical Center, Department of Pharmacology and Tennessee Valley Healthcare System, Department of Veterans Affairs). YUMM 2.1 cells were cultured in Dulbecco's Modified Eagle's medium (DMEM, Gibco), supplemented with 10% fetal bovine serum (FBS, Sigma Aldrich), 1% penicillin streptomycin (Gibco), and 1x MEM non-essential amino acid (Sigma Aldrich). YUMM 2.1 cells were cultured at 37 ^{0}C and 5% CO_2. To develop xenografts in B6 (C57BL/6J, Jackson laboratory) mice, 1.5 million YUMM 2.1 cells per 100 µl were injected into the right flank of each mouse. The xenografts were monitored with a caliper every two days. Once the tumor reached 5 mm in diameter, functionalized AuNS, anti-PD-L1-pMBA-AuNS and anti-CD8-DTNB-AuNS at 1.5:1 ratio was administrated into mice intraperitoneally (i.p.) for PET and SERS imaging experiments. Each mouse was injected with 1.2 mg of AuNS with 800 µCi of Cu64 activity. For blocked control, 200 µg anti-PD-L1 (Bio X Cell, clone 10F.9G2) and 200 µg of anti-CD8 (Bio X Cell, clone 53-6.7) antibodies were injected (i.p.) concurrently with AuNS at the other side of abdominal cavity. Note, the antibodies utilized for pre-blocked control were the same clone as the antibodies used to functionalized AuNS.

Mice bearing YUMM 2.1 xenograft (for both experiment and pre-blocked control groups) were first placed in a small animal imaging PET/CT machine (Inveon microPET/CT from Siemens Preclinical, Knoxville TN). Mice were imaged at 6, 18, and 42 h post AuNS administration. The images were uploaded in the imaging software Amide and three dimensional regions-of-interest (ROIs) were drawn around the tumors, liver, kidneys, and muscle. Once the tumor xenografts were identified with PET, SERS imaging was then performed at 5 different sites of the tumor xenograft with a custom portable Raman imaging setup. The Raman fiber optic probe was gently placed on on the xenograft. Measurements were taken for 10 s with a 785 nm laser (Innovative Photonics

Solutions) at 80 mW. Raman measurements were done at the same time points as PET imaging (6, 18, and 42 h post AuNS administration). To calibrate the Raman spectrometer, acetaminophen, naphthalene, and a neon-argon lamp were used as standards to determine the Raman shift from the absolute and relative wavenumber axis of the system. Raman scattering from the samples were first collected from the fiber optic probe, then by an imaging spectrograph (Kaiser Holospec). CCD camera (Princeton Instruments) was used to capture the obtained spectrum.

Raman spectra were first processed for spectral response calibration with a National Institute of Standards and Technology (NIST) calibrated lamp. Savitzky-Golay filter (2,7) was then applied for spectra smoothing and background subtraction was performed with a modified (7^{th} order) polynomial fit method. At each time point, both DTNB and pMBA peaks, 1325 cm^{-1} and 1580 cm^{-1} were normalized to 1440 cm^{-1} biological peak, which does not change over time.

4.3.5 In vivo Multimodal Multiplexed Imaging to Monitor Treatment Responses

1.5 million YUMM 2.1 cells per 100 µl were injected into the right flank of each mouse to develop tumor xenografts. Once the tumor reached 5 mm in diameter, immunotherapy treatment or IgG control injection commenced. Each treatment mouse received 3 doses of 115 µg of anti-CD137 antibodies (Bio X Cell, clone 3H3) and 200 µg of anti-PD-L1 (Bio X cell, clone 10F.9G2) antibodies every 3 days. Each IgG control mouse received 3 doses of 115 µg of IgG2a isotope control (Bio X Cell, BE0089) and 200 µg of IgG2b isotope control (Bio X cell, BE0090) every 3 days. Tumor sizes were measured with a caliper every 2 days. Mice weight was also monitored to ensure the therapy did not cause any extraneous side effects. A day after the last treatment, mice were administrated with functionalized AuNS, anti-PD-L1-pMBA-AuNS and anti-CD8-DTNB-AuNS at 1.5:1 ratio for PET/SERS imaging. PET imaging and Raman measurement were performed in the same manner as previously described.

4.3.6 Toxicity Study of AuNS in vivo

1.5 million YUMM 2.1 cells per 100 µl were injected into the right flank of each mouse to develop tumor xenografts. Once tumor reached 5 mm in diameter, functionalized AuNS, anti-PD-L1-pMBA-AuNS and anti-CD8-DTNB-AuNS at 1.5:1 ratio was administrated into mice intraperitoneally (i.p.). Mice were sacrificed either 5 or 15 day post particle injection. Cardiac puncture was performed as soon as the mice were euthanized to obtain 500 µl of blood per mouse for both complete blood count (CBC) and serum liver/kidney metabolite study. In addition, tumor, heart, liver, kidney and spleen of each mouse were retrieved and fixed in 6% formalin for Hematoxylin and eosin (H&E) staining. The toxicity study was performed at Vanderbilt University Medical Center – Translational Pathology Shared Resources. Complete blood counts were performed in the Forcyte Veterinary Hematology Analyzer manufactured by Oxford Science. Blood chemistries were performed on the Vet Axcel Chemistry Analyzer manufactured by Alfa Wassermann.

4.3.7 Inductively Coupled Plasma-Mass Spectrometry (ICP-MS)

Mice bearing YUMM 2.1 xenograft were injected with functionalized AuNS, anti-PD-L1-pMBA-AuNS and anti-CD8-DTNB-AuNS at 1.5:1 ratio. For each mouse, the tumor, stomach, liver, spleen, kidneys, heart, lungs, brain and muscle were retrieved either 5 or 15 days post particle injection. After dissection, the tissues were frozen immediately in liquid nitrogen. Lyophilizer was first used to remove any water in the tissues. Next, dried tissues were then place in 75 vol. % traced metal grade aqua regia (HCl from Fisher Scientific, A508-P500 and HNO_3 from Fisher Scientific, A509-P500) for 72 h. Aqua regia was then boiled off and the tissue samples were then redissolved in 10 ml of 2 vol. % aqua regia. Filters (0.4 µm) were used to remove any impurities prior to ICP-MS readings.

ICP-MS measurement and analysis were performed at Vanderbilt University, Department of Civil and Environmental Engineering. Perkin Elmer model ELAN DRC II was operated in standard mode for all readings. The setting of the instrument was 1.5 kW radio frequency power, 15 L/min argon plasma flow, 1 L/min nebulizer flow, and 1 s integration time for 3 replicates. Six-point calibration curve was performed for gold isotope 197 between 0.05 μg/L and 500 μg/L. Analytical blanks and check standard (0.5 μg/L) were measured for every 3-5 samples to ensure the readings were within 15% of the specified value.

4.3.8 Transmission Electron Microscope Imaging of Tissues

Mice bearing YUMM 2.1 tumor xenograft were injected with functionalized AuNS, anti-PD-L1-pMBA-AuNS and anti-CD8-DTNB-AuNS at 1.5:1 ratio. The mice were sacrificed at 6h post particle administration, and the tumor xenograft, liver, and spleen were retrieved. All samples were sectioned into 1 mm by 1 mm pieces with razor blades and fixed in 2.5% gluteraldehyde in 0.1M cacodylate buffer (pH 7.4 ± 0.1) first at room temperature for 1 h then 24 h at 4 ºC. The specimens were further processed for transition electron microscopy imaging by the Vanderbilt Cell Imaging Shared Resource facility. The tissue samples were further fixed with 1% osmium tetraoxide and washed with 0.1 M cacodylate buffer. Sample dehydration was done serially with graded ethanol. Three 100% ethanol exchanges and two exchanges of pure propylene oxide (PO) were performed. The samples were then filtrated with 25% Epon 812 resin and 75% PO for 30 minutes at room temperature then with 50% Epon 812 resin for 1 h and 50% PO overnight. Subsequently, all samples went through a Epon 812 resin and PO (3:1) exchange and incubated with pure epoxy resin overnight. Before sample embedding, two exchanges of pure epoxy resin were performed. Lastly, polymerization was done at 60 °C for 48 h. Once the embedding process was complete, the samples were first sectioned at 500-1000 nm then were cut for 70-80 nm ultra-

thin sections. The samples were placed on copper grids and stained with uranyl acetate (2%) and Reynold's lead citrate. TEM imaging was performed with the Philips/FEI Tecnai T12 electron microscope.

4.4 Results and Discussion

Gold nanostars were synthesized with a biological buffer, HEPES (2-[4-(2-hydroxyethyl)piperazin-1-yl]ethanesulfonic acid), as previously described by our group.[25, 168-169] HEPES binds weakly to gold surface allowing straightforward surface modification with chelated radiolabel, Raman tags, and antibodies for targeted detection. Two sets of AuNS were synthesized: (i) PD-L1 detection nanostars were functionalized with antiPD-L1 mAbs, Raman tag para-mercaptobenzoic acid (pMBA), and DOTA chelated ^{64}Cu radiolabel; (ii) for CD8 detection, nanostars were functionalized with antiCD8 mAbs, Raman tag 5,5-dithio-bis-(2-nitrobenzoic acid) (DTNB) and ^{64}Cu. Since PET cannot distinguish signals between radiolabels, the different Raman tags covalently bound to AuNS surface enabled multiplexed detection. To ensure stability of AuNS *in vivo*, mAbs and chelated radiolabel were covalently conjugated to AuNS via a bifunctional linker, OPSS-PEG2000-NHS which formed amide bonds with the primary amines on the mAbs and DOTA (Figure 4.1bi). The polyethylene glycol (PEG) in the linker stabilized the mAbs and DOTA, and then covalently attached to the nanostars via a thiol in the orthopyridyl disulphide (OPSS) group resulting in multimodal AuNS (Figure 4.1bii).

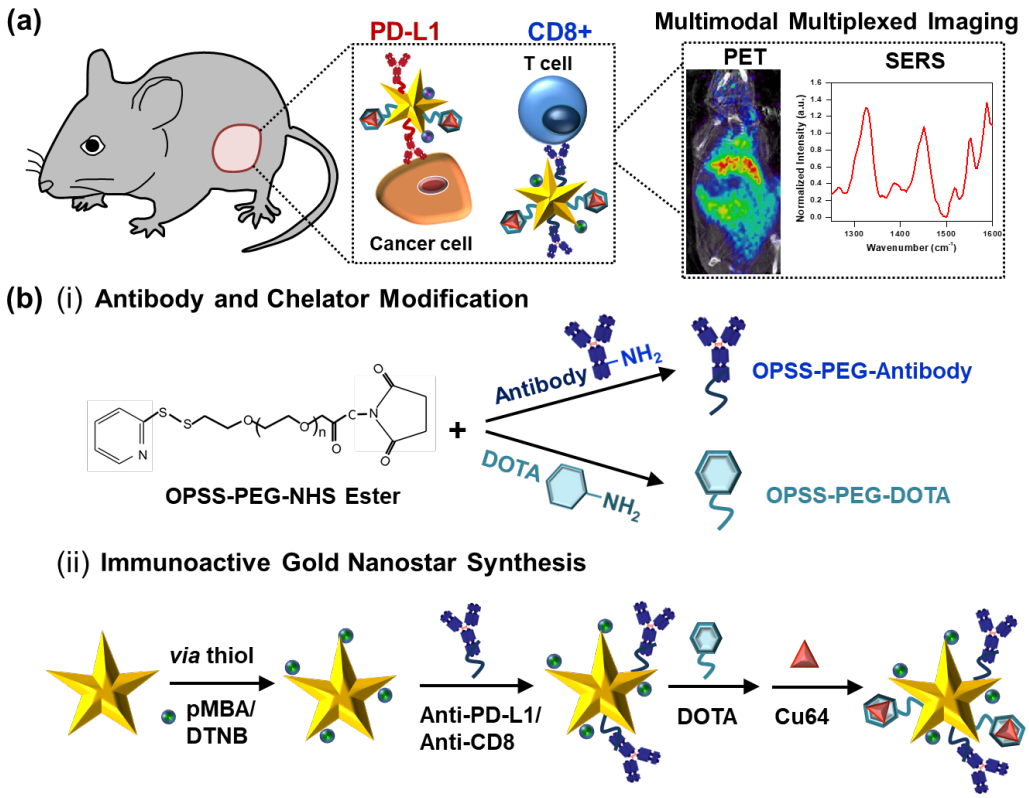

Figure 4.1 (a) Schematic representation of AuNS-mediated multimodal multiplexed ImmunoPET-SERS imaging to detect PD-L1 and CD8+ T cells in YUMM 2.1 melanoma tumors. (b) Schematic describing the synthesis of AuNS. (i) Antibodies and DOTA chelator were modified with a bifunctional linker OPSS-PEG2000-NHS ester forming an amide bond and terminating the PEG stabilized antibodies and chelator with a thiol via the orthopyridyl disulphide (OPSS) group. (ii) Gold nanostars were functionalized with Raman tags (pMBA or DTNB) via a thiol-Au reaction followed by conjugation with PEG stabilized antibodies and DOTA, and finally ^{64}Cu radiolabels were chelated to give rise to AuNS.

The physicochemical properties of AuNS were characterized with electron microscopy (Figure 4.2a) showing star-shaped morphology, and dynamic light scattering (Figure 4.2b) indicating <100 nm dimension which is ideal for accumulation in the TME through the enhanced permeability and retention (EPR) effect.[194, 231] The increase in size of nanostars post-functionalization results in a ~30 nm red shift in the plasmon resonance (Figure 4.2c) allowing them to absorb tissue-penetrating near-infrared light that has a 3-5 cm penetration depth[232-234], ideal for *in vivo* SERS. Our previous work also show nanostars generate intense electromagnetic

fields when illuminated with resonant light amplifying the vibrational signal of Raman molecules by 10^9 amenable for high resolution SERS.[63, 228] The SERS spectra of an equimolar mixture of AuNS consisting of AuNS/antiPD-L1/pMBA/^{64}Cu + AuNS/antiCD8/DTNB/^{64}Cu show the Raman tags have minimal spectral overlap (Figure 4.2d) enabling multiplexed immunomarker detection. We also validated Cu chelation to AuNS with inductively coupled plasma mass spectrometry (ICP-MS) and quantified 0.99±0.04 µg Cu/mg Au in the presence of DOTA relative to 0.035±0.02 µg Cu/mg Au for bare nanostars control indicating successful radiolabeling of AuNS (Figure 4.2e). In addition, zeta potential measurements confirmed (Figure 4.2f) PEG conjugation on AuNS results in near neutral surface charge necessary to minimize uptake by the mononuclear phagocyte system (MPS).

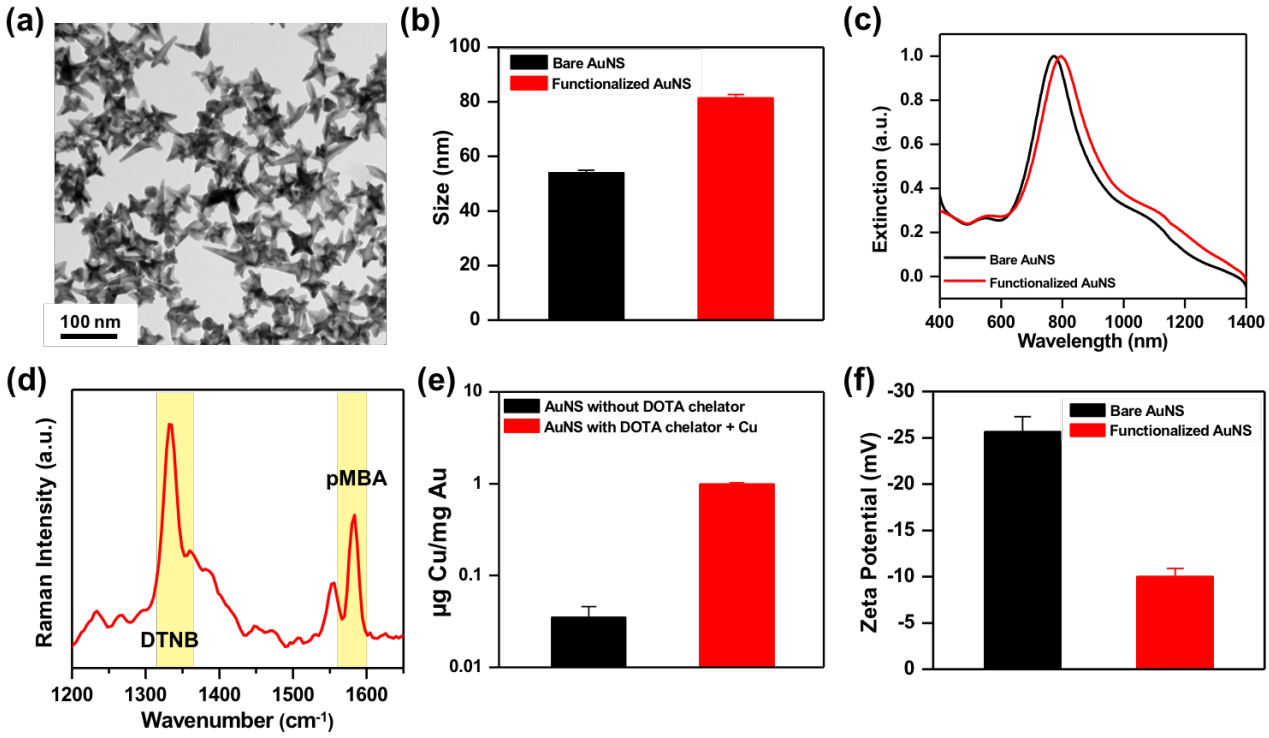

Figure 4.2 Physicochemical properties of AuNS. (a) TEM micrograph of AuNS showing their star shape. (b) Hydrodynamic size and (c) extinction spectra of bare gold nanostars (AuNS) and functionalized AuNS. (d) Raman spectra of a mixture of AuNS targeting CD8 and PD-L1 via DTNB (1325 cm^{-1}) and pMBA (1580 cm^{-1}) tags respectively; the signature peaks of the tags are

highlighted. (e) Amount of Cu chelated per mg AuNS quantified via ICP-MS. (f) Zeta potential of the bare AuNS and functionalized AuNS.

Multiplexed immunomarker detection was achieved in a murine model of melanoma with Yale University Mouse Melanoma cell line variant 2.1 (YUMM 2.1) tumors which are highly immunogenic with intrinsically upregulated PD-L1 expression and high infiltration of CD8+ T cells.[235] We evaluated the biocompatibility and toxicity profile of AuNS in YUMM 2.1 tumor-bearing mice at 5, and 15 days post IP delivery of AuNS (60 μg/g) to examine both near-term and longer-term impact. Standard serum inflammatory markers were evaluated to determine if AuNS elicit any immune response or toxicity in mice. Alanine aminotransferase (ALT) and aspartate aminotransferase (AST) were used as indicators of liver function (Figure 4.3a) and total bilirubin (TBIL), creatinine (CREA), and blood urea nitrogen (BUN) were used to measure renal function (Figure 4.3b).[236-237] Further, the complete blood count (CBC) including hemoglobin, red blood cell, white blood cell, and platelet concentration (Figure 4.3c-e) were also examined in mice sera. These serum biochemical markers were comparable for mice that received AuNS relative to control mice without AuNS indicating minimal inflammatory response or toxicity from AuNS. The monocyte and lymphocyte counts were evaluated in mice (Figure 4.3f) which shows no obvious immune response was elicited with AuNS post-delivery. These observations were confirmed with hematoxylin and eosin (H&E) stain of major organs and tumor of mice that received AuNS and no noticeable abnormalities or histopathological changes were observed (Figure 4.4).

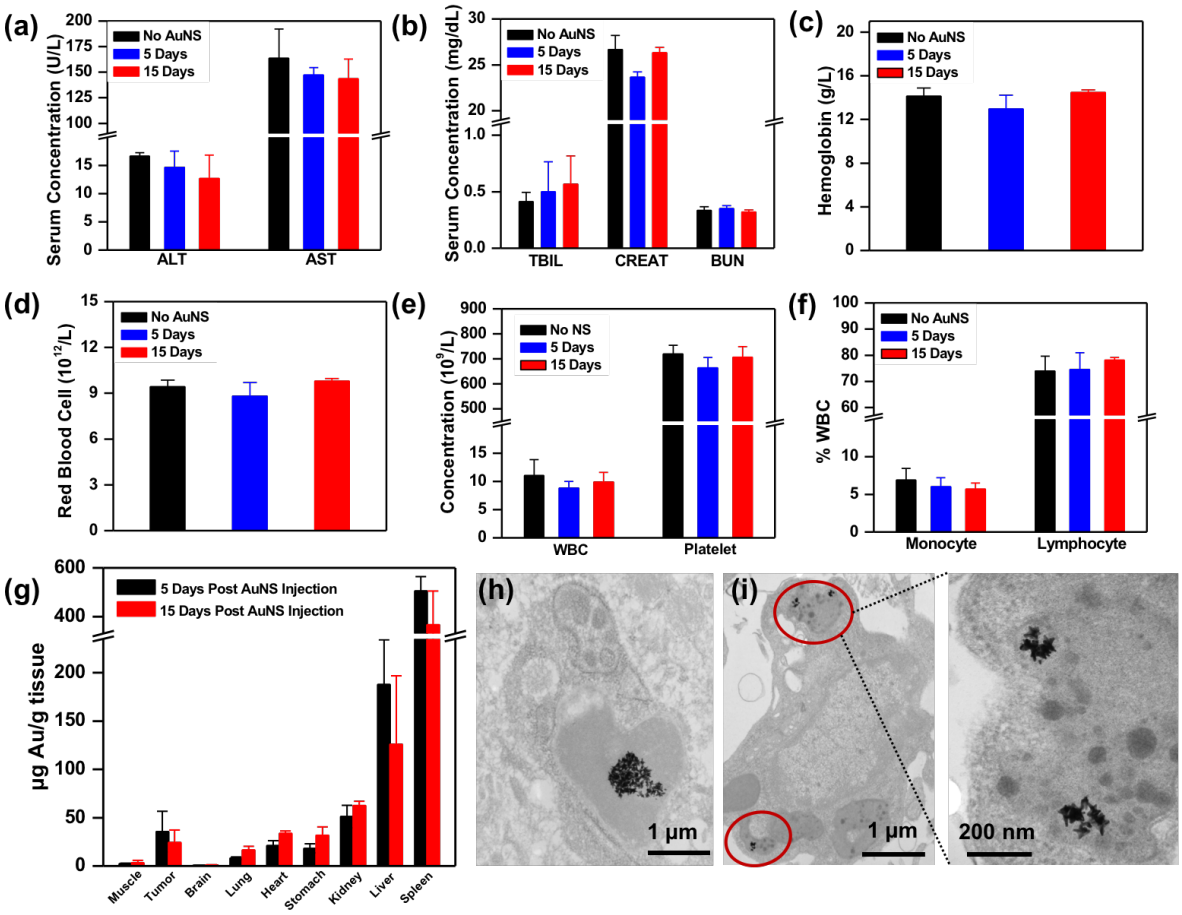

Figure 4.3 Toxicity and Biodistribution of AuNS. Serum inflammatory markers and complete blood count of control mice without AuNS (n=3) and mice that received IP delivery of AuNS (n=3 for both 5 and 15 days post-delivery). Inflammatory markers including (a) liver enzyme, alanine aminotransferase (ALT) and aspartate aminotransferase, (AST), and (b) kidney markers, total bilirubin (TBIL), blood urea nitrogen, CREAT (creatinine), and blood urea nitrogen (BUN) shown no significant differences in control and mice that received AuNS. Complete blood analysis also shows no abnormality in hematology parameters including (c) hemoglobin, (d) red blood cell, (e) WBC (white blood cell) and platelet, and (f) white blood cell profile, % monocyte and % lymphocyte. (g) Biodistribution and clearance of AuNS confirmed with ICP-MS showing Au in tumor, muscle, and major organs both 5 days (n=3) and 15 days (n=3) post AuNS delivery. TEM micrographs of AuNS in (h) Kupffer cells in liver and (i) intracellular vesicles in tumors.

Understanding the biodistribution and clearance of AuNS *in vivo* is necessary to understand their pharmacokinetics, bioavailability, and stability. Quantitative ICP-MS analysis of Au in tumor and major organs that were retrieved 5 and 15 days post IP delivery of AuNS (Figure 4.3g)

demonstrate both near-term and long-term clearance pathway of AuNS. AuNS amounts in all organs are provided in detail in supporting information (Table 4.1). AuNS were retained in tumors even at 5 and 15 days post-delivery indicative of active targeting in TME as well as accumulation through EPR effect. Trace Au was found in brain tissue since the blood brain barrier prevents the entry of nanoparticles larger than 10 nm, and minimal Au was found in muscles, lungs, and stomach, as expected. Whereas the size of AuNS limits their filtration through the glomerular capillary wall of kidneys in mice, this should not impede clinical translation of AuNS as micron-sized particles have shown renal clearance in large animals and humans.[199-200] Here, AuNS were predominantly cleared through the MPS organs the of spleen and liver via internalization by macrophages as expected for gold nanoparticles.[204-205] TEM micrographs confirm that AuNS were localized in Kupffer cells in the liver (Figure 4.3h). In the tumor, AuNS were observed in intracellular vesicles or lysosome-like structures (Figure 4.3i) suggesting internalization through receptor-mediated endocytosis.

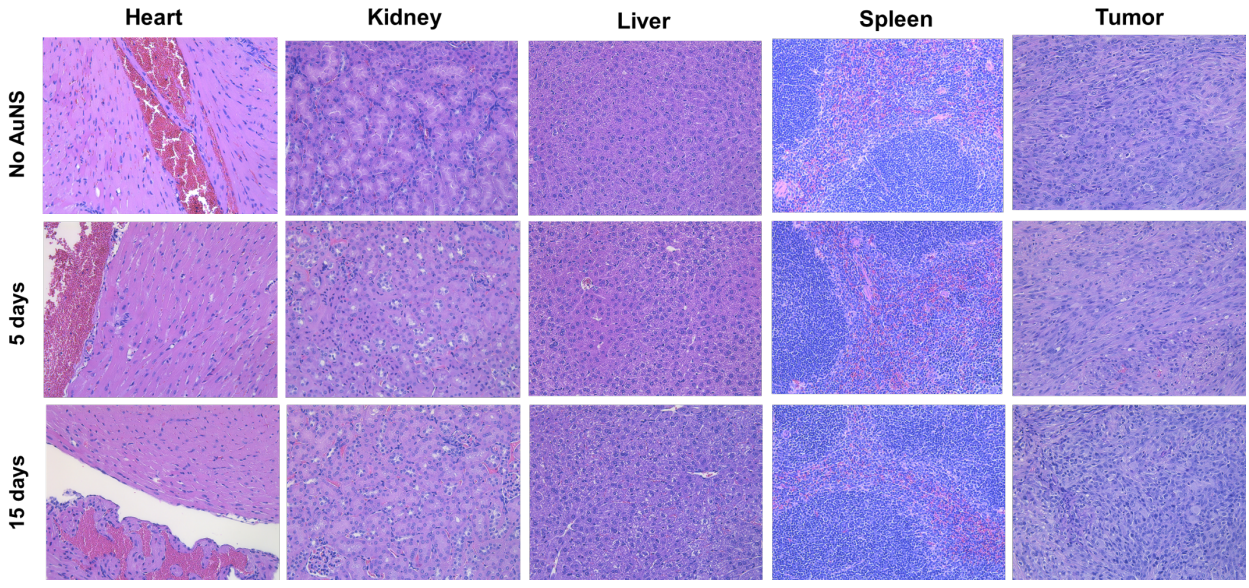

Figure 4.4 Hematoxylin and eosin (H&E) stain of heart, kidney, spleen, liver and tumor for AuNS toxicity study. H&E stain of mice tissues shows AuNS does not impose any toxicity to the animal.

Table 4.1 Quantitative ICP-MS analysis of biodistribution of AuNS in YUMM 2.1 tumor-bearing mice 5 and 15 days post AuNS delivery.

Organ	*Days After AuNS Injection*	
	5	15
Muscle	2.1± 0.8	3.1 ± 2.6
Tumor	35.6 ± 21.0	24.3 ± 12.9
Brain	0.5 ± 0.2	0.9 ± 0.5
Lung	8.1 ± 1.2	16.5± 4.0
Stomach	18.3 ± 4.6	31.7 ± 8.8
Heart	21.2 ± 5.2	33.6 ± 2.6
Kidney	51.2 ± 11.5	62.4 ± 4.8
Spleen	505.0 ± 59.0	366.4 ±138.2
Liver	187.9 ± 46.2	125.9 ±71.0

Next, we demonstrated biocompatible AuNS detect both PD-L1 and CD8 *in vivo* in the TME via longitudinal ImmunoPET-SERS imaging after IP delivery of AuNS (60 μg/g) in YUMM 2.1 tumor-bearing mice. First, PET and CT images were acquired in mice at 6, 18, and 42h post AuNS administration to observe their accumulation in tumors and major organs via whole body scans. Both coronal (Figure 4.5a) and transverse views (Figure 4.5b) indicate AuNS accumulate in tumors but also in spleen and liver. To account for the decay of ^{64}Cu (half-life ~12 h), tumor-to-muscle (T/M) ratio was obtained (Figure 4.5c) which quantitatively showed an increase in PET signal even at 42h. The continuous increase in PET signal over time in experimental group indicates a lower background (muscle) signal which suggests that AuNS are retained in tumors over a long period. AuNS have longer plasma half-time compared to radiolabeled antibodies which enables an extended longitudinal imaging and immunomarker detection as shown here. The specificity of AuNS in PD-L1 and CD8 detection in TME was demonstrated by blocking both immunomarkers in control mice and administering a saturating dose of antiPD-L1 and antiCD8

mAbs (200 μg each). T/M ratio showed statistically significant differences between experimental and blocked control group demonstrating the high specificity of AuNS in detecting immunomarkers in the TME. However, multiplexing cannot be achieved with PET to distinguish the signal between the two immunomarkers, which was achieved with SERS. SERS measurements were acquired immediately after imaging using a custom portable Raman setup equipped with a 785 nm continuous-wave laser at 80 mW power and a fiber optic probe. SERS spectra was acquired by placing the probe at eight different locations on the tumor; spectra were then averaged and background subtracted using a Savitzky-Golay filter.[238] The SERS peaks corresponding to detection of CD8+ T cells (DTNB, 1325 cm^{-1}) and PD-L1 tumor cells (pMBA, 1580 cm^{-1}) were normalized to the biological peak at 1440 cm^{-1} (corresponding to lipids and proteins) which remains consistent within the same mouse over time. The SERS spectra (Figure 4.5d) before AuNS delivery (0h) and at 6h time-point clearly shows AuNS accumulate in tumors enabling highly specific multiplexed detection of PD-L1 and CD8 in experimental tumors relative to blocked control. Longitudinal SERS (Figure 4.5e) showed the maximum accumulation of AuNS occur at 6h post AuNS delivery and a decrease in SERS intensity at 42h time-point indicates clearance of AuNS. Quantitative SERS analysis at 6h indicated a statistically significant difference in CD8 (49% lower DTNB signal) and PD-L1 (38% lower pMBA signal) detection between experimental and receptor-blocked control mice (Figure 4.5f).

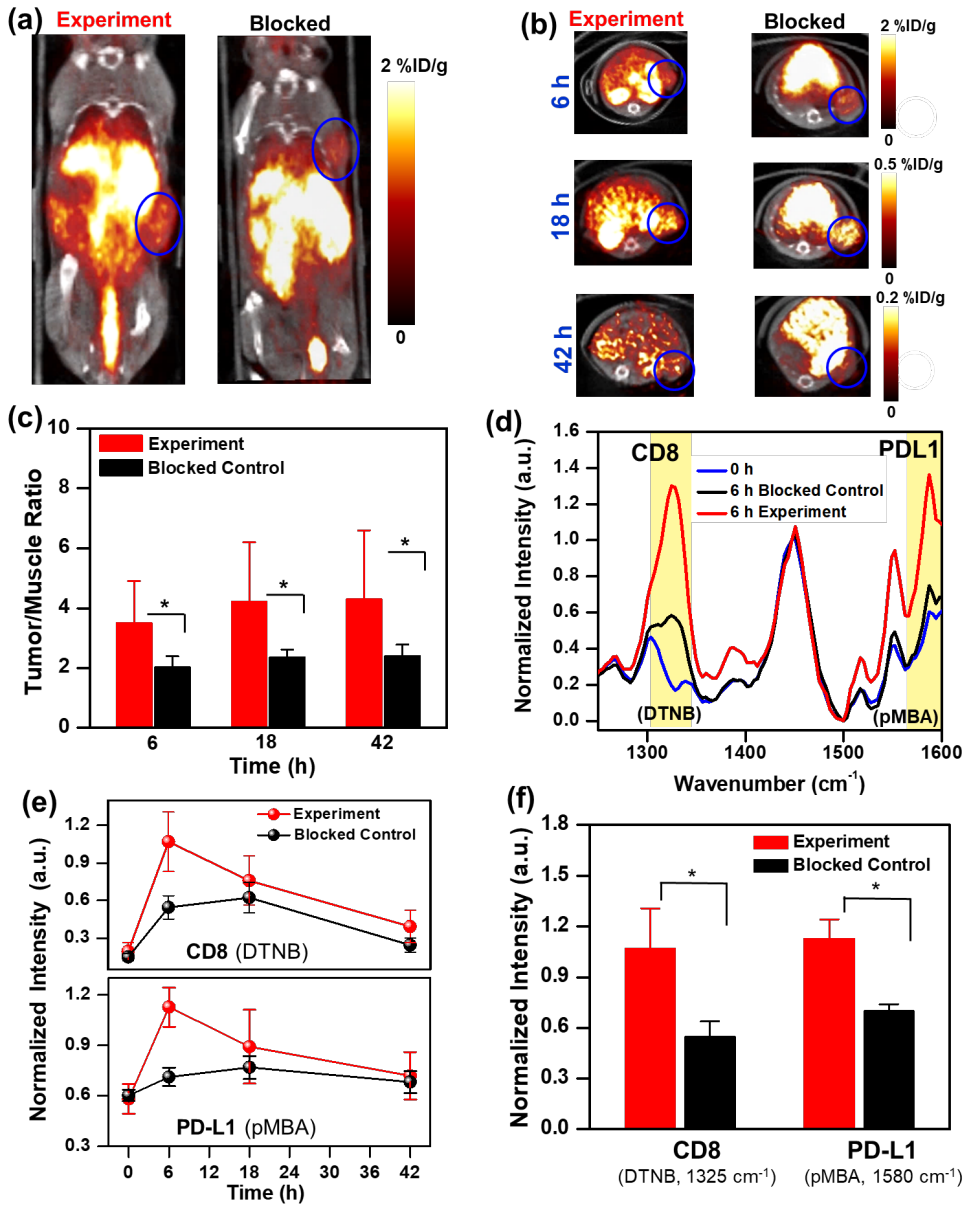

Figure 4.5 ImmunoPET-SERS detection of PD-L1 and CD8 with AuNS. (a) Whole body PET/CT images of mouse bearing YUMM 2.1 tumors at 6 h post AuNS delivery. In control receptors were blocked with mAbs prior to AuNS delivery. (b) Transverse PET/CT images at 6h, 18 h, and 42 h post AuNS delivery. In (a) and (b) tumors are indicated in circle. (c) Longitudinal PET by examining tumor to muscle (T/M) ratio showing statistically significant differences ($p<0.05$) in uptake of AuNS in experimental tumors (n=7) relative to blocked control (n=5). (d) Normalized SERS spectra of tumors before AuNS delivery (0 h) and at maximum accumulation time (6 h) of experimental and blocked control mice. The dominant peak for Raman tags DTNB (1325 cm^{-1}) and pMBA (1580 cm^{-1}) are highlighted in yellow. (e) Longitudinal SERS analysis where pMBA and DTNB peaks were normalized to intrinsic lipid peak at 1440 cm^{-1}. (f) SERS quantification of PD-L1 and CD8 at maximum accumulation time indicating statistically significant differences (~49% difference in DTNB and ~38% in pMBA) between experiment and blocked control groups ($p<0.05$).

We further validated our *in vivo* ImmunoPET-SERS results by examining the tumors of experimental and blocked control mice with flow cytometry. Quantitative flow (Figure 4.6) showed a decrease in PD-L1 positive tumor cells (42.6% to 0.34%) and CD8 positive T cells (7.47% to 0.086%) confirming both the high sensitivity and specificity of AuNS in multiplexed immunomarker detection. This confirms that endpoints generated with ImmunoPET-SERS enable an accurate screening tool for immunomarker detection and treatment planning.

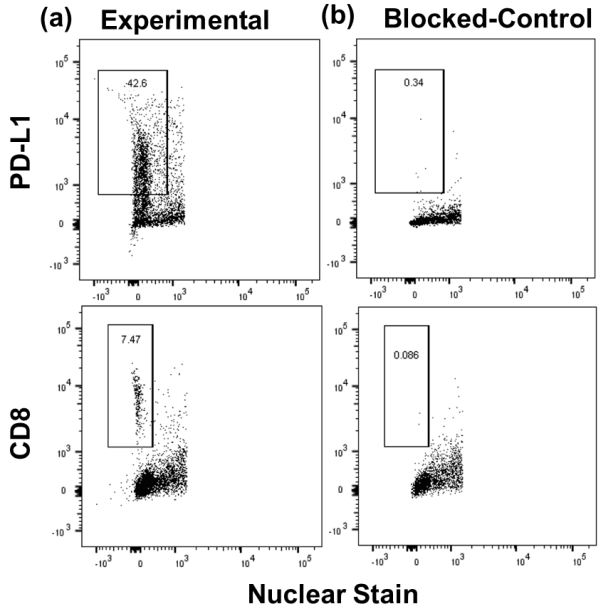

Figure 4.6 Flow cytometry of Yumm 2.1 tumor. Experimental tumors are both PD-L1 and CD8 positive. Blocked-control animals were introduced with blocking anti-PD-L1 and anti-CD8 antibodies. Blocked-control tumors show significantly less PD-L1 and CD8 positive cells as the surface receptors were saturated by the blocking antibodies.

We also demonstrate that AuNS are effective in monitoring response to immunotherapies (Figure 4.7) in YUMM 2.1 tumor-bearing mice treated with 3 doses of combination immunoagents of antiPD-L1 (200 μg/mouse) + antiCD137 (110 μg/mouse). CD137, a member of tumor necrosis factor receptor super family, is expressed on activated T cells. Co-stimulation of CD137 results in expansion of effector T cells, production of cytokines, and resistance to suppression by regulatory

T cells. The utility of CD137 agonist mAbs with PD-L1 blockade has demonstrated synergistic antitumor effect.[239-240]

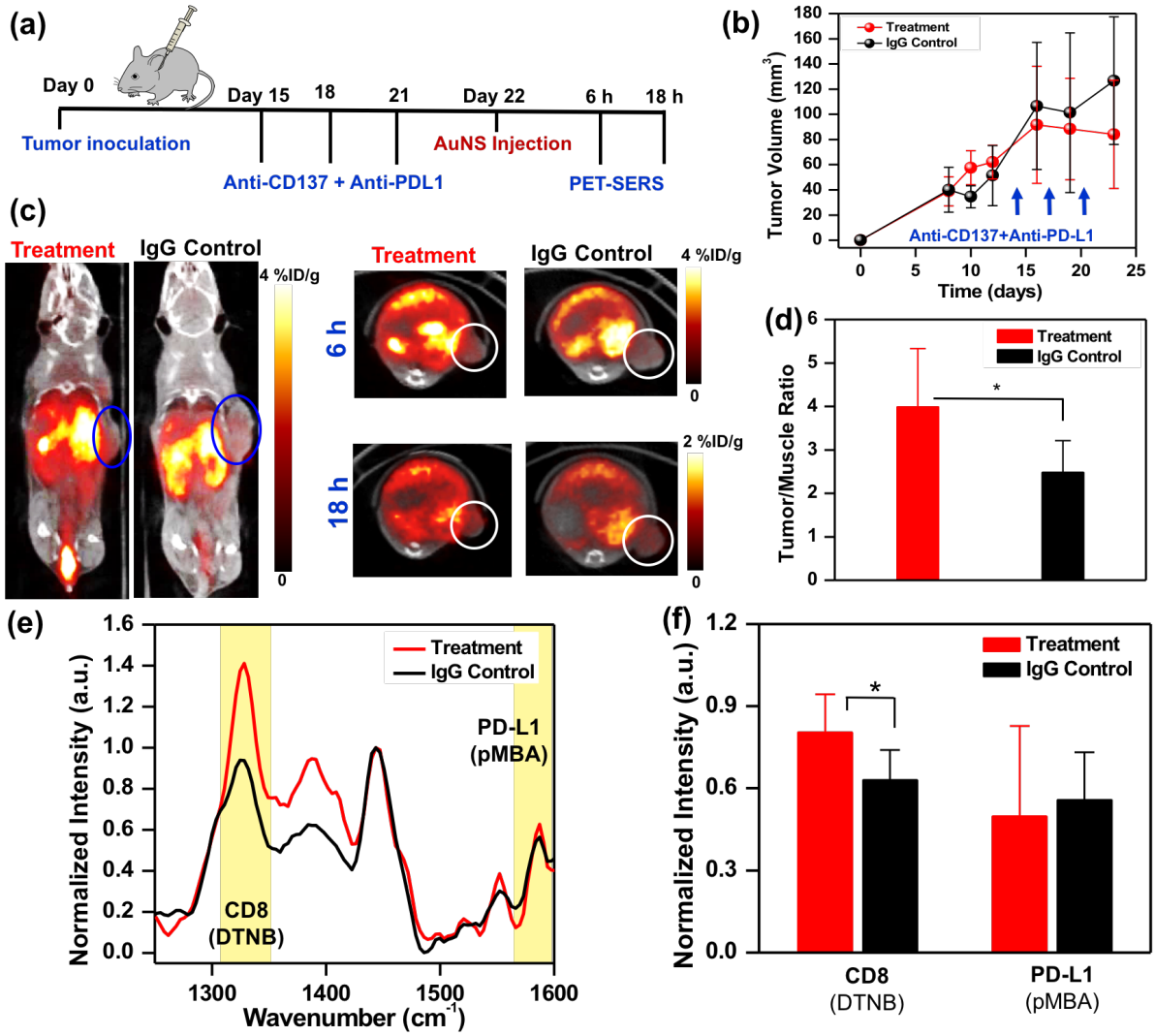

Figure 4.7 ImmunoPET-SERS imaging to monitor response to immunotherapy. (a) Mice bearing YUMM 2.1 tumors were treated with 3 doses of combinatorial immunotherapy of anti-CD137 + anti-PD-L1 followed by AuNS delivery and imaging 24 h after the last treatment. Control mice received isotype-matched IgG treatment. (b) Tumor volumes indicated a decrease in tumor size with immunotherapy. (c) Coronal (left) and transverse (right) PET images of mouse reveal a higher localization of AuNS in tumors of treatment group relative to IgG control. (d) Corresponding quantitative PET analysis showing tumor/muscle ratio. (e) Averaged SERS spectra shown for immunotherapy group and IgG control group. (f) Corresponding SERS quantification showing a statistically significant increase in CD8+ tumor infiltrating lymphocytes in immunotherapy group, but minimal change in PD-L1 status.

AuNS were delivered 24 hours after the last treatment followed by ImmunoPET-SERS to monitor alterations in CD8 and PD-L1 status (Figure 4.7a). The body weight of the mice was monitored to ensure minimal extraneous effects in mice during the course of their therapy (Figure A. 4.1). A decrease in tumor volumes (Figure 4.7b) indicated response to combinatorial immunotherapy by YUMM 2.1 tumor-bearing mice relative to control mice that received isotype-matched anti-IgG (310 μg/mouse). Co-registered PET-CT images of mice (Figure 4.7c) show AuNS accumulate in both tumors and major organs supporting our biodistribution studies. Quantitative PET analysis of tumor to muscle ratio showed statistically significant differences between treatment and control mice (Figure 4.7d) indicative of response to combination immunotherapy by YUMM 2.1 tumors. However, PET cannot delineate if the observed differences in PET intensities correspond to PD-L1 inhibition or infiltration of activated CD8+ T cells. Multiplexed treatment response with SERS (Figure 4.7e) clearly showed proliferation and infiltration of CD8+ T cells in tumors of treatment group mice (indicated by 1325 cm^{-1} DTNB peak) which corresponds well with the trends observed in PET and decrease in tumor volumes in treatment group. However, SERS spectral analysis of PD-L1 (indicated by 1580 cm^{-1} pMBA peak) showed minimal difference between treatment and control mice (Figure 4.7f). This is not surprising as YUMM 2.1 tumors have a constitutionally high expression of PD-L1, and further infiltration of CD8+ T cells in tumors results in interferon gamma (IFN-γ) induced upregulation of PD-L1. Our results further emphasize the importance of multiplexed imaging *in vivo* to identify multiple immunomarkers that are engaged in the immune TME and provide an accurate measure of response to immunotherapies.

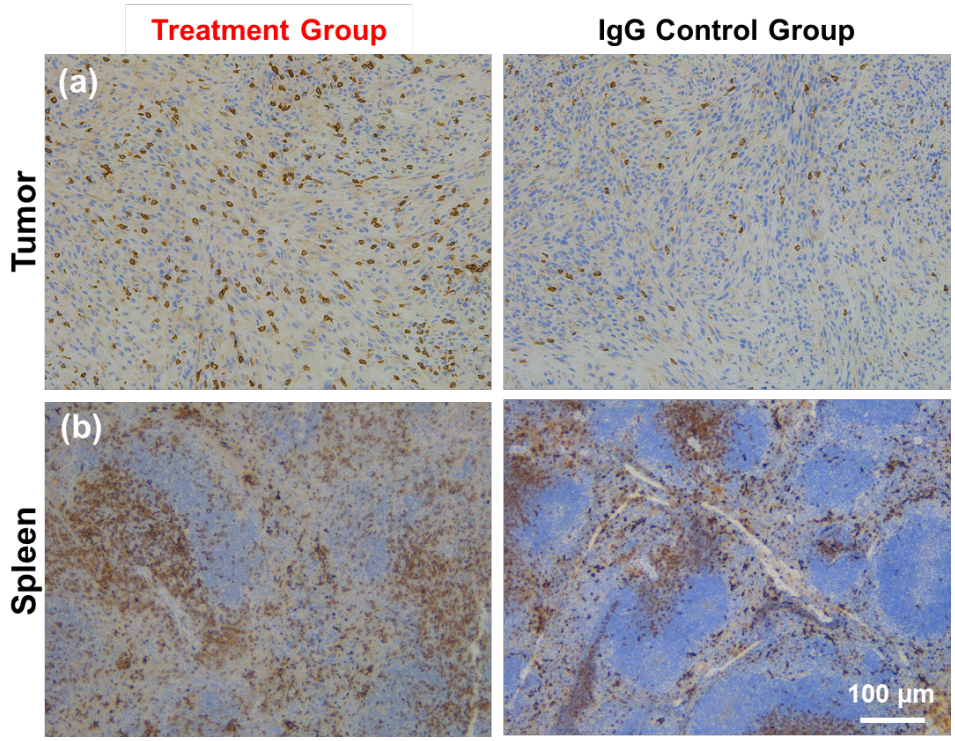

Figure 4.8 Immunohistochemistry of (a) tumor and (b) spleen show combination immunotherapy results in expansion and infiltration of CD8+ tumor infiltrating lymphocytes (clone 4SM15, brown spots). Hematoxylin is counter stain (light blue).

In vivo ImmunoPET-SERS imaging endpoints were validated *ex vivo* with immunohistochemistry analysis of tumor (Figure 4.8a) and spleen (Figure 4.8b) stained for CD8+ T cells. IHC clearly shows expansion of activated CD8+ tumor infiltrating lymphocytes in mice treated with combinatorial immunotherapy relative to IgG control (Figure 4.9). Localization of CD8+ T cells in the splenic T cells zones (Figure A. 4.2) also suggests systemic T cell activation and expansion at the peripheral organ. *In vivo* endpoints were further verified with standard H&E staining of tumor sections, which showed no apparent alteration in tissue histomorphology in both immunotherapy and control group (Figure A. 4.3).

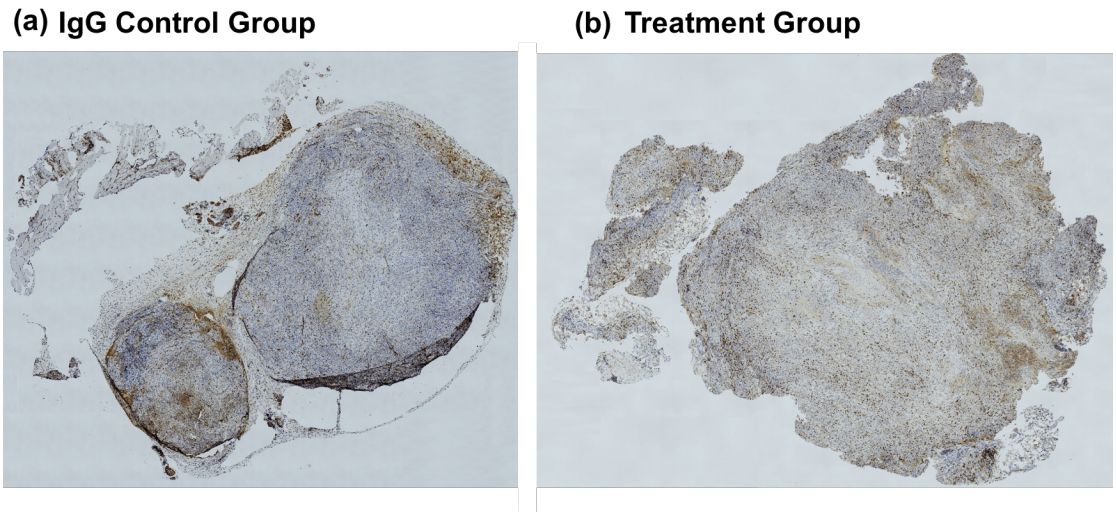

Figure 4.9 Immunohistochemistry of CD8 marker for (a) control tumor and (b) therapy tumor (anti-CD137+anti-PD-L1 combination therapy).

4.5 Conclusion

In summary, we demonstrate the design and *in vivo* validation of an innovative and ultimately clinically-translatable nanoprobe, AuNS, that integrates the merits of PET and SERS imaging on a single multimodal platform providing real time immunological tumor profiling of multiple immunomarkers engaged in the immune TME. Our results, validated in a murine melanoma model in immunocompetent mice, show AuNS provide dynamic status of PD-L1 and CD8 *in vivo* combining the depth-resolved whole body imaging of PET with high resolution multiplexing of SERS. ImmunoPET-SERS therefore facilitates both; (i) screening before treatment to identify targetable pathways, and (ii) monitoring response to immunotherapies to improve the objective response rate of PD-1/PD-L1 blockade. Our imaging platform also distinguish mice that were responders (YUMM 2.1 tumors) from nonresponders (YUMM 10.1) to immunotherapies combining antiPD-L1 + antiCD137 to both block PD-L1 and proliferate and activate CD8+ T cells. The results of this work will ultimately allow us to translate ImmunoPET-SERS from preclinical mouse models to humanized mice that recapitulate primary human tumors

and validate the efficacy of our approach for immunomarkers detection in clinically relevant models. Further, our platform can be expanded beyond melanoma to a multitude of malignancies by targeting other inhibitory ligands (TIM3, LAG3, PSGL-1) and other immune cell population (CD4+ T cells, NK cells). Moreover, whereas in this proof of concept study multiplexed SERS enabled us to track two immunomarkers PD-L1 and CD8, future work will develop cutting-edge AuNS to detect >5 biomarkers simultaneously *in vivo* enabling a powerful tool for immunoprofiling heterogeneous tumors, and monitoring response to immunotherapies.[241-242]

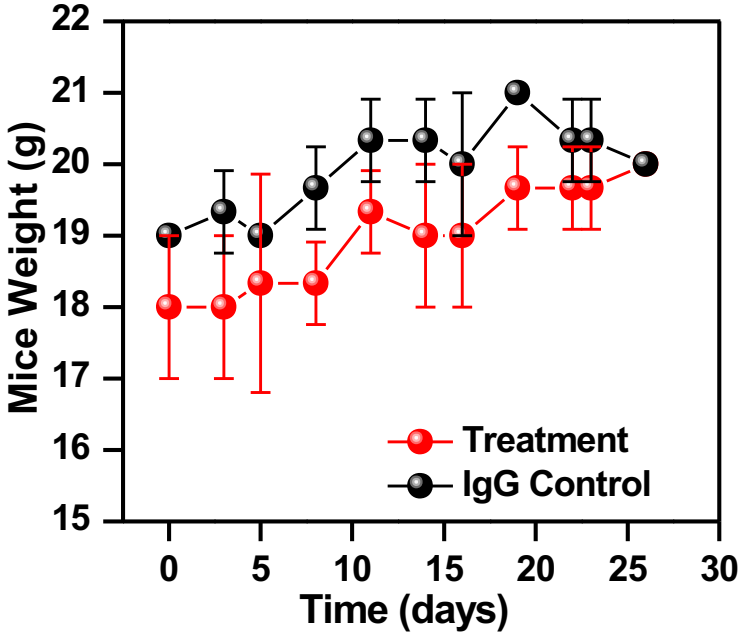

Figure A. 4.1 Mice weight and tumor volume for both control group and therapy group (anti-CD137+anti-PD-L1 combination therapy).

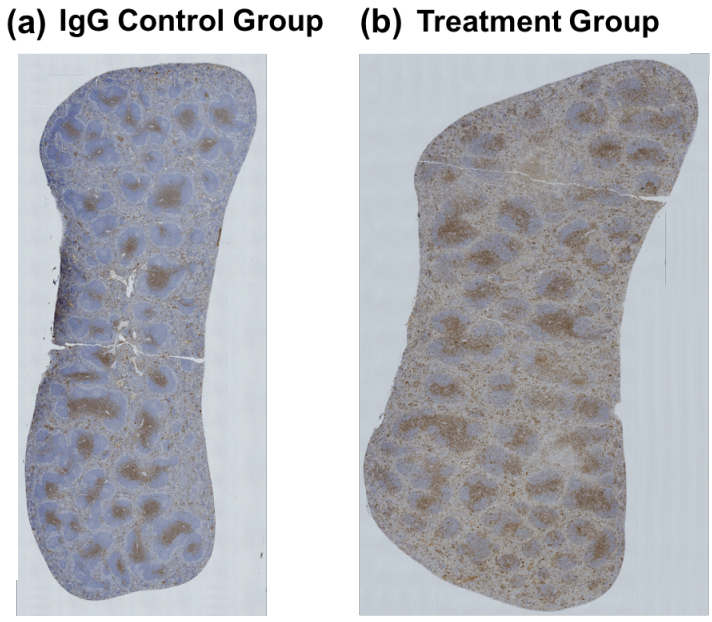

Figure A. 4.2 Immunohistochemistry of CD8 marker for (a) control spleen and (b) therapy spleen (anti-CD137+anti-PD-L1 combination therapy).

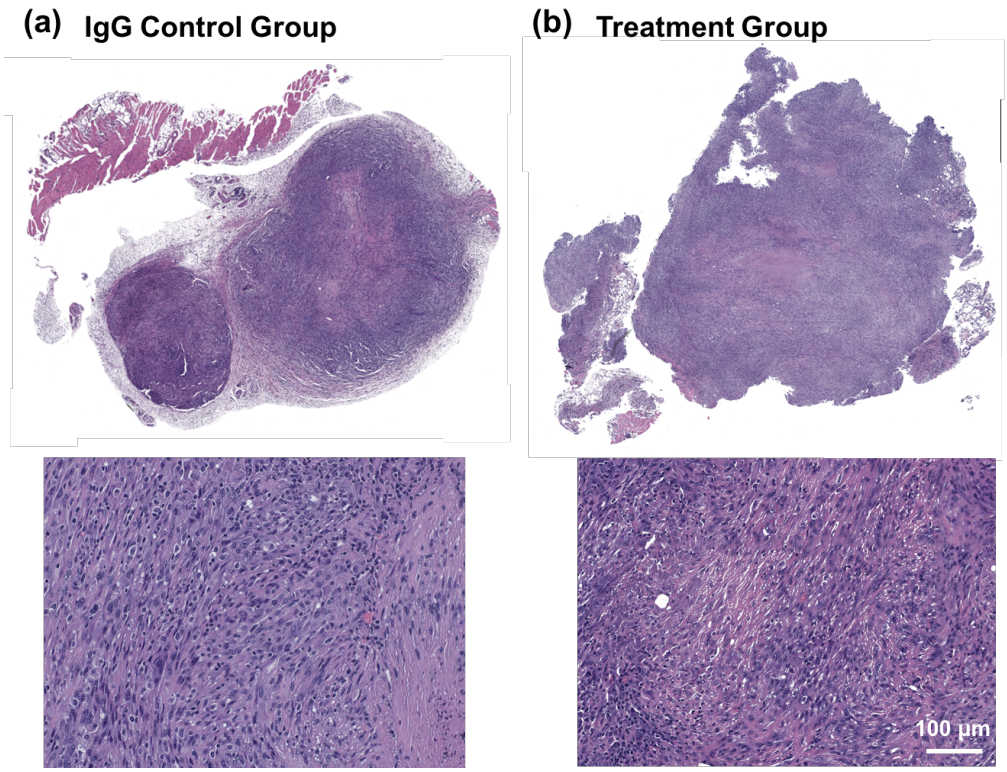

Figure A. 4.3 Hematoxylin and eosin (H&E) stain of tumor section for (a) IgG control group and (b) treatment group (anti-CD137+anti-PD-L1 combination therapy)

Chapter 5

LABEL-FREE RAMAN MAPPING TO MONITOR TREATMENT RESPONSE IN BREAST CANCER

5.1 Summary

Small molecule inhibitors that target oncogenes have gained tremendous interest in cancer therapy. Mek inhibitor (MEKi) in MAPK/ERK pathway and PI3K inhibitor (PI3Ki) in PI3K/AKT/mTOR pathway have shown promising antitumor responses by hindering tumor progression. To monitor treatment responses, magnetic resonance imaging and computed tomography are used to determine changes in tumor size. Positron emission tomography can be used to observe the changes in tumor metabolism. However, the imaging methods above are extremely expensive. Here, we show the use of Raman spectroscopy to detect metabolic and biochemical changes rapidly and inexpensively. Triple negative breast cancer (MDA-MB-231) cells that are known to be responsive to MEKi but not to PI3Ki were treated with different concentrations of each inhibitor then Raman maps were acquired. Averaged spectra of the cells show DNA, protein, and lipid Raman footprints. To further differentiate changes in cellular metabolism and biomolecular content post-treatment, principal component analysis (PCA) was used. PC scores of PC1-PC3 were plotted. PC2 score for cells treated with different MEKi concentrations showed clusters in individual boundaries while no discrimination in PC scores was observed for cells treated solely with PI3Ki. PC2 showed cells treated with MEKi varied in choline peaks (both phosphatidylcholine and phosphatidylinositol), indicating the responses to the treatment since inhibition in MAPK/MEK leads to a decrease in choline transporter. However, cells treated with PI3Ki do not show significant changes in Raman footprints or clustering in PCA.

The results showed the ability of Raman spectroscopy to differentiate cells that are responsive versus non-responsive to small molecular drugs.

5.2 Introduction

Small molecule inhibitors have shown promising anti-tumoral outcomes by blocking the signaling cascade of oncogene activation. KRAS and BRAF oncogenes are two of the most commonly mutated pathways in human cancer. Gain-of-function gene alteration such as receptor mutation, upregulation, or amplification in intermediate signal transducers can lead to constitutive activation of pathways that leads to cancer proliferation, survival, motility and angiogenesis.[243] Several small molecule inhibitors were approved by the FDA to target the mTor (mechanistic target of rapamycin) and MAPK (mitogen-activated protein kinase)/ERK (extracellular signal-regulated kinases) pathways. PI3K (Phosphoinositide 3-kinases) inhibitor was first approved in 2014 to treat leukemia and lymphoma while MEK (mitogen-activated protein kinase) inhibitor was first approved in 2013 to treat melanoma.[244] Several clinical trials are currently evaluating the therapeutic outcomes of combining different small molecule inhibitors or combining small molecule inhibitors with immunotherapy. Combining MEK inhibitor (MEKi) with checkpoint blockage therapy results in reliable therapeutic response to treat melanoma by stimulating immunity at the tumor microenvironment and increasing lymphocyte infiltration.[245] The recent success of small molecule inhibitors emphasize the significance of such targeted therapies in combating cancer.

Clinical standards to evaluate the efficacy of small molecular inhibitors or other anticancer treatments is to monitor the change in tumor size by using magnetic resonance imaging (MRI) or computed tomography (CT). While tumor size is an important criterion to predict the outcome and

efficacy of anti-cancer treatments, it is not always accurate. Some tumors can experience pseudo-progression, which is an initial enlargement of the tumor before a decrease in size.[246] Moreover, changes in tumor size is usually a downstream effect of cancer therapy. Thus, there is a clinical need to accurately predict patient responses to cancer therapy during the early stages of treatment. Probing metabolism changes of cancer cells after treating patients with small molecule inhibitor can provide accurate therapeutic outcome prediction before a visible reduction in tumor size is observed. For example, MEK inhibition is known to reduce choline metabolism. Choline is a precursor major cell membrane phospholipids, phosphatidylcholine and phosphatidylinositol. Since the ERK/MAPK pathway is linked to fatty acid metabolism, inhibition me MEK also has shown to decrease fatty acid content.

The primary clinical imaging modalities to monitor metabolism changes are PET imaging, mass spectroscopy, and magnetic resonance spectroscopy (MRS) but certain drawbacks exist in their current form when tracking metabolism changes. PET imaging is an established technique, but can be cost prohibitive and can only observe one metabolite at a time. Mass spectroscopy can measure multiple metabolites simultaneously; however, this imaging method is destructive to tissues and time consuming. Mass spectroscopy also requires a significant amount of tissue and cells samples, which is challenging to obtain from clinical biopsies. Lastly, MRS can also evaluate multiple metabolites, but each metabolite requires its own separate and specific label. To overcome the described challenges, we propose to use label-free Raman spectroscopy to monitor metabolism changes during small molecule inhibitor treatment. Raman scattering is an inelastic scattering of light which reveals the vibrational states of a molecule. Raman spectroscopy can be used to characterize and identify chemical composition of samples. Thus, biological information can be extracted in a single Raman spectrum. The quantity of patient samples required for accurate Raman

analysis is significantly less than what is needed for mass spectroscopy. Raman spectroscopy is an inexpensive and non-destructive technique that is capable of monitoring multiple metabolites simultaneously without the need for labels.

Due to its efficiency and flexibility, label-free Raman spectroscopy has been used in many different biological applications. Raman signatures can distinguish different immune cells such as B cells and T cells. The technique is sensitive enough to differentiate breast cancer cell lines,[247-249] and specific enough to track the delivery and cellular uptake of chemotherapy drugs.[250-251] Raman spectroscopy is also utilized to delineate tumor margins in real time brain surgery and to even monitor the changes in a uterus and accurately predict preterm labor.[177, 252] Here, we apply label-free Raman platform to monitor metabolic changes and treatment responses in triple negative breast cancer cells after treatment with small molecule inhibitors. Further, by using principle component analysis, treatment responder groups can be easily identified.

5.3 Materials and Methods

5.3.1 In vitro Raman Mapping to Monitor Metabolic Changes

MDA-MB-231 breast cancer cells were purchased from ATCC (HTB-26) and cultured in DMEM supplemented with 10% FBS. Cells were maintained at 37 $^{\circ}$C and 5% CO_2. Cells were seeded on 6 well plate at approximately 60% confluence. Once the cells have attached on the plate, different concentrations of MEKi (Selleck Chemical, Trametinib), PI3Ki (Selleck Chemical, Alpelisib), Taxol (Invitrogen, Paclitaxel) or a combination of two in complete DMEM were added. After 3 days of incubation, old media was removed and the cells were trypsinized. Detached cells were centrifuged at 200 g for 7 min to remove dead cells and then re-seeded on poly-l-lysine coated calcium fluoride windows. Once the cells have reattached on the CaF_2 disks, media was removed.

Next, cells were washed with phosphate buffer saline (PBS) three times, fixed in 4% formaldehyde (methanol-free) at room temperature for 10 minutes, washed with PBS three times again then finally dried at room temperature prior to Raman mapping.

Cells on CaF_2 disks were visualized using a Raman microscope. Brightfield image of the cells were captured with 100x objective. A rectangular area capturing 3-4 cells was selected for Raman mapping at 2 μm by 2 μm resolution. Raman spectral requisition was obtained with a 785 nm laser with 1200 lines/mm grating with 10 s acquisition time. Using the Renishaw WiRE 3.4 software, cosmic ray removal was first performed with nearest neighbor method. A custom MATLAB code was used to perform smoothing and background correction. The spectra first underwent smoothing by using the Savitzsky and Golay filter (order of 5 and coefficient value of 61). An automated, modified polyfit method was applied to remove fluorescent background by using a 7^{th} order polynomial with a threshold of 0.0005. To eliminate non-cell pixels from the rectangular map, biological peak at 1440 cm^{-1} was selected to generate the cellular masks. The pixels were considered cell, or "mask" when the intensities were higher than the set threshold. A Gaussian function was utilized to the mask images to smooth the edges of the cell. The brightfield optical images were used to ensure the accuracy of the final cell masks. Clusters of pixels (as one cell) in the Raman map were then averaged and defined as one cell for further principle component analysis (PCA). PCA was performed by using custom MATLAB code. First three principle components were plotted to discriminate each treatment group.

5.3.2 Viability Assay

MDA-MB-231 cells were passaged and seeded on 96 well plates. Once the cells were attached on the plates (~ overnight), different concentrations of MEKi, PI3Ki, and Taxol in complete media were added to the wells. After 72 h of treatment, old media was removed and

replaced with 100 µl of fresh media mixed with 10 µl of 12 mM 3-(4,5-dimethylthiazol-2-yl)-2,5-diphenyltetrazolium bromide (MTT, ThermoFisher Scientific). After 3 h of incubation, 85 µl of the media solution was removed and 50 µl of dimethyl sulfoxide (DMSO) was added to solubilize and dissolve the formazan. A Biotek Synergy H1 plate reader was used to read the absorbance at 540 nm.

5.3.3 Western Blot

MDA-MB-231 cells were passaged, counted, and seeded on 6 well plates. The number of cells seeded on each well was counted by a scepter to ensure each sample contained the same number of cells and proteins. Once the cells were attached on the plates (~ overnight), different concentrations of MEKi and PI3Ki in complete media were added to the wells. After 6 h of treatment, lysis buffer was added to the cells and incubated for 30 min at 4°C. Lysates were then centrifuged at 18,000 *g* for 15 min at 4°C. Equal amounts of proteins were mixed with Laemmli buffer and boiled for 5 min. The samples were then loaded on 10% SDS-PAGE, and subsequently transferred onto nitrocellulose membranes through electrophoresis overnight at cold room. The membranes were blocked before adding primary antibodies. Primary and secondary antibodies were prepared in the blocking buffer. All antibodies were purchased from Cell Signaling Technology. Primary antibodies were against Akt (9272S), phospho-Akt (9271S), Erk 1/2 (9102S) and phosphor Erk ½ (9101S).

5.4 Results and Discussion

Raman mapping of MDA-MB-231 was performed with a NIR 785 nm laser with 100x objective. Three cells were mapped in a single rectangular requisition at 2 µm by 2 µm. As a result, each cell contains between approximately 50 to 500 pixel or spectra per cell, depending on the size

of the cell. Bright filed image showed cells maintained their morphology after seeding and fixing on calcium fluoride disks (Figure 5.1a). Averaged Raman spectra of the cells is plotted (Figure 5.1b). Biological peaks can be easily identified by comparing the values to literature findings.[175] The strongest biological peak is at 1440 cm^{-1}, which comes from CH_2 bending and deformation mode for lipids and collagen. The strong and sharp peak at 1000 cm^{-1} indicates the phenylalanine of collagen and protein. Other Raman features include readings at 1300 cm^{-1} (CH_2 twisting modes from fatty acid at), 1250 cm^{-1} (Amide III, protein and collagen bands), and 1090 cm^{-1} DNA peak (symmetric phosphate stretching vibration mode). Further, multivariate analysis and principle component analysis (PCA) were performed (Figure 5.1c) to show a high-resolution Raman map can provide information regarding cytoplasmic component of the cells. PC1 map identified mainly the proteins and lipids of the overall cell (indicated by bends between 1200 to 1500 in Figure 5.1d). PC2 map reveals the localization of nucleus, identified by the negative features at 800 cm^{-1} (O-P-O stretching of DNA and RNA backbones and ring breathing modes in DNA and RNA bases).

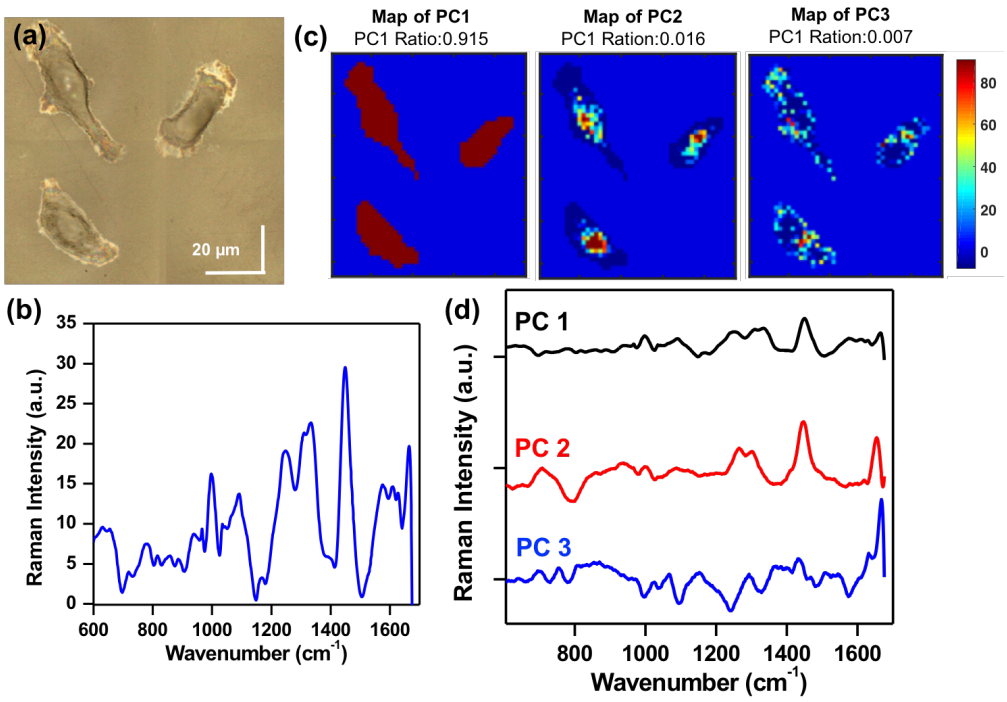

Figure 5.1 Raman mapping of MDA-MB-231 cells. (a) Bright filed image of three fixed MDA-MB-231 cells on CaF_2 disk imaged Renishaw Raman Spectroscopy at 100x objective. (b) Averaged spectra of MDA-MB-231 cells. (c) Principle component analysis (PCA) maps of cell. (d) Each PCs spectrum is plotted.

To show the capability of label-free Raman spectroscopy to observe metabolism changes after inhibition of MAPK/ERK pathway, MDA-MB-231 was treated with Trametinib for 72 hours. Cells were then reseeded and fixed on CaF_2 disk for Raman mapping. Averaged cell spectra treated with (50 nM) and without Trametinib was plotted (Figure 5.2a). Several differences can be visualized, for example, peak intensities of the lipid and proteins peaks between 1200 cm^{-1} to 1500 cm^{-1} decreased for cells treated with 50 nM MEK inhibitors. However, it is extremely difficult to identify all the subtle changes in Raman peaks without using a multivariate analysis; thus, PCA was performed (Figure 5.2b). Cells treated with different concentrations of MEKi clustered in a concentration/linear dependency by PC2. Since 1 nM MEKi is outside the working therapeutic range, cells treated with 1 nM MEKi grouped closely with cell that did not receive any treatment. PC2 consists of several important peaks such as phosphotidylcholine (890 cm^{-1}, blue box on Figure

5.2c) and phosphatidylinositol (780 cm^{-1}, green box on Figure 5.2c). The two phospholipids have been identified to be strongly affected by MEK inhibition. Other major peaks in PC2 include mostly protein peaks such as 1655 cm^{-1} amide I and 1230 cm^{-1} amide III. MTT cellular viability assay was then carried out to correlate our findings until cell death. Figure 5.2d showed MDA-MB-231 cells activated apoptosis in concentration dependent manner. Western blot was also performed to confirm the cell death observed in MTT assay was attributed to the inhibition of MEK. Activation of ERK pathway produces an abundance of phospho-ERK, which transduce the downstream signaling pathway. As a result, western blot showed that as MEK inhibitor concentration increases, the bend for phospho-ERK reduced and disappeared (Figure 5.2e).

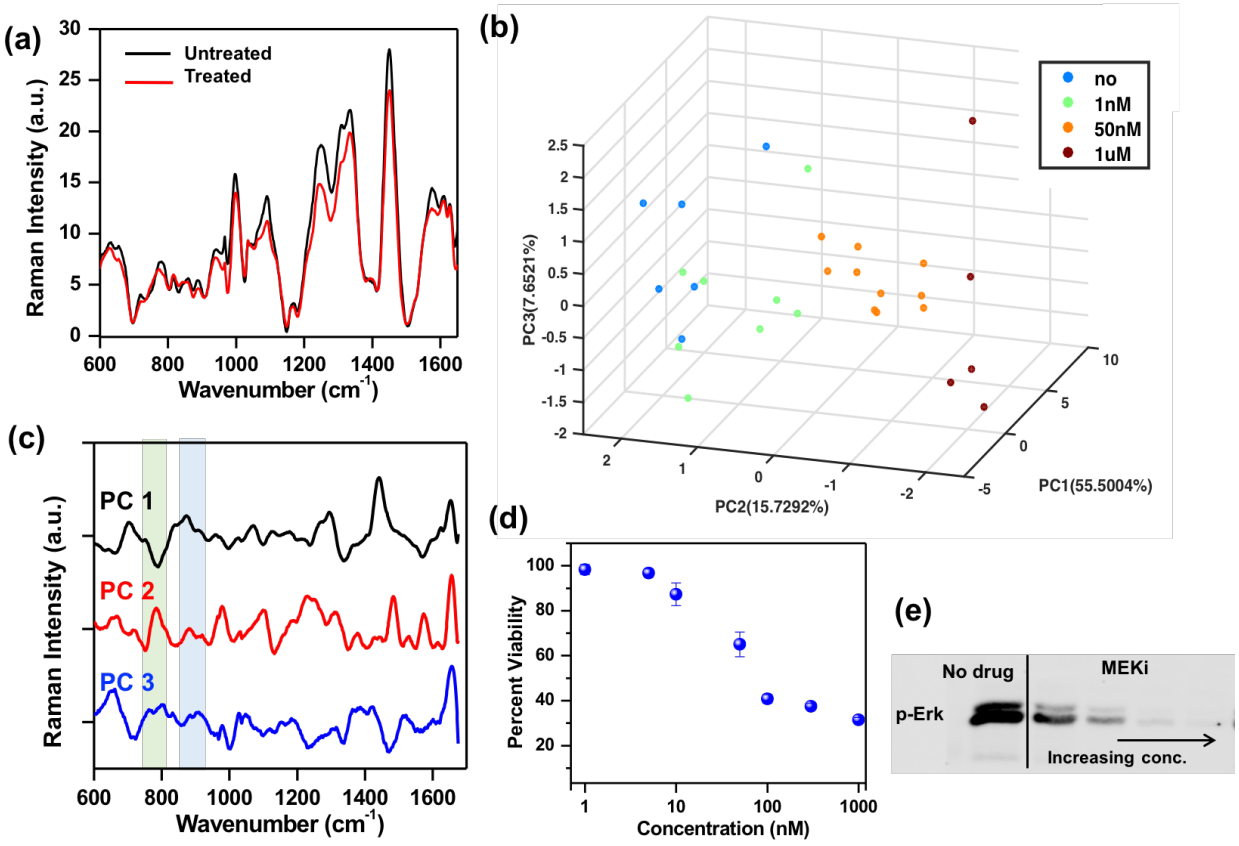

Figure 5.2 MDA-MB-231 cells treated with Trametinib (MEKi) (a) Raman spectra of cells treated with (red) or without (black) MEKi at 50 nM. (c) PCA analysis of cell treated with various concentration of MEKi. (d) PC1-3 of PCA analysis. Green box indicated phosphatidylinositol peak

at 780 cm^{-1} and blue box indicated phosphotidylcholine peak at 890 cm^{-1}) (d) MTT viability assay and (e) western blot of cells treated with different concentration of MEKi.

Next, MDA-MB-231 cells were treated with two different control drugs, PI3K inhibitor and the chemotherapy drug, Paclitaxel. MDA-MB-231 cells do not respond to PI3K inhibitor as shown in MTT assay (Figure 5.3a). As a result, PCA showed no discrimination between cells treated with or without PI3Ki (Figure 5.3b). Cells treated with a combination of MEKi and PI3Ki (50 nM MEKi and 1 μM PI3Ki) do however differentiate into one cluster by PC2, which consist of phosphatidylinositol peak at 780 cm^{-1} (green box on Figure 5.3c). MDA-MB-231 cells were then treated with Paclitaxel as control since chemotherapy drugs should not affect the metabolism of cells, but instead induce cellular apoptosis (Figure 5.3d). One key step during apoptosis is DNA fragmentation, thus PC1 discriminated between cells treated with or without Paclitaxel (Figure 5.3e) with mainly DNA/RNA peak at 800 cm^{-1} (green box, Figure 5.3f). Cells were also treated with Paclitaxel combined with MEKi (50 nM MEKi and 50 nM paclitaxel); however, PCA was not able to distinguish the group. We hypothesized the effect of apoptosis is more dominant than the subtle biochemical and metabolic changes from MEKi, thus the combined treatment group was clustered with Paclitaxel treated groups.

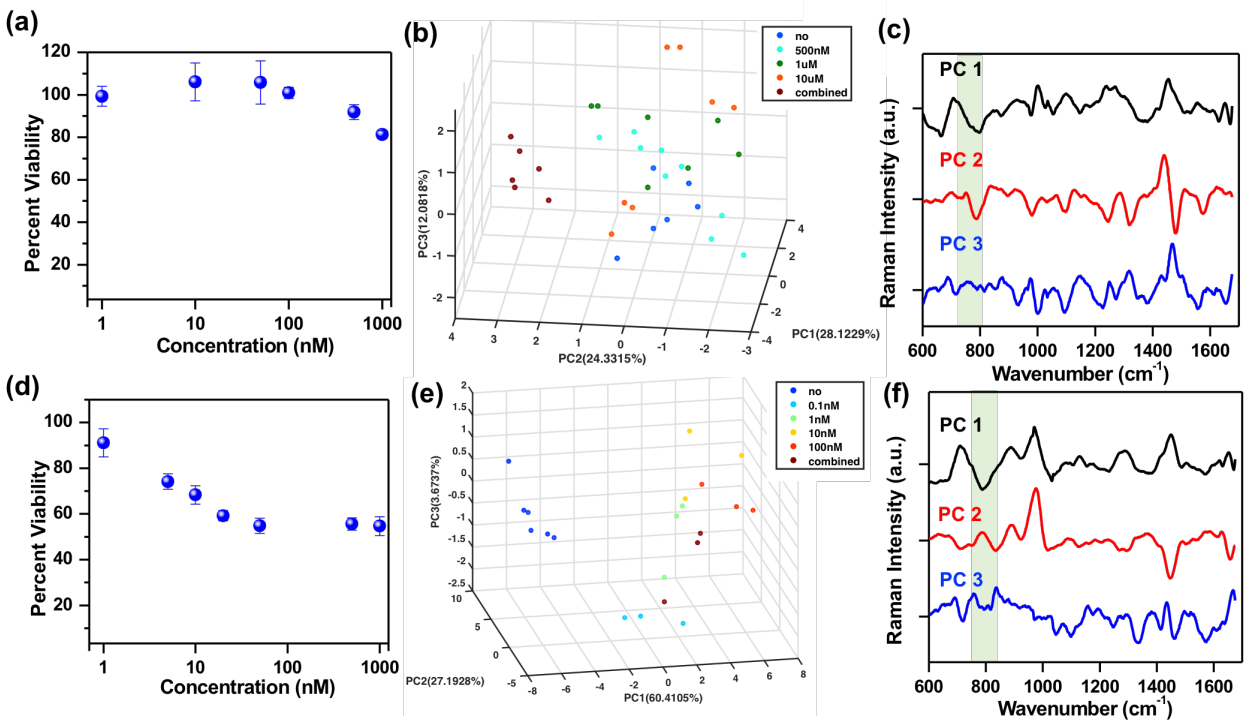

Figure 5.3 (a) MTT assay (b) PCA (c) PCs of MDA-MB-231 cells treated with PI3Ki. (d) MTT assay (e) PCA (f) PCs of MDA-MB-231 cells treated with Paclitaxel. Treatment was performed for 72 hours.

5.5 Conclusion

We have shown the use of Raman spectroscopy to rapidly and inexpensively detect metabolic and biochemical changes after triple negative breast cancer cells (MDA-MB-231) were treated with small molecule drug, MEK inhibitor (MEKi). Cells treated with high MEKi showed decreases in both phosphotidylcholine and phosphatidylinositol peaks, indicating response to the treatment since inhibition in MAPK/MEK leads to decrease in choline transporter. To further differentiate changes in metabolism and biomolecular content post-treatment, principal component analysis (PCA) was performed. PC scores discriminated cells treated with various MEKi concentrations and showed clusters in individual boundaries. The results demonstrated the ability of Raman spectroscopy to monitor treatment responses to small molecule drugs. We envision the

platform will eventually be translated to study patient derived samples and ultimately applied to a broad spectrum of disease and treatments.

Chapter 6

CONCLUSIONS AND FUTUREOUTLOOK

6.1 Conclusions

I have designed, synthesized and utilized gold nanostars (AuNS) for combination cancer therapy and molecular imaging. The NIR plasmon resonance of AuNS allows deep tissue light penetration in our *in vivo* studies making them flexible and versatile for biological use. Further, the geometry of AuNS, spherical core with multiple sharp protrusions can generate strong electromagnetic fields that is favorable for photothermal efficiencies. Moreover, Raman hot stops can be generated between neighboring AuNS to achieve ultra-sensitive surface enhanced Raman spectroscopy.

In chapter 2, we combined hyperthermia generated by AuNS and trigger-drug release from low temperature sensitive liposomes to induce apoptosis in triple negative breast cancer, MDA-MB-231. The synergistic effect showed efficient and effective therapeutic outcome. Hyperthermia facilitated cytotoxicity of chemotherapeutic agents, thus the combination therapy resulted in 58% cell death at doxorubicin concentration of 2 μg/ml in a drug-resisting cell line.

In chapter 3, we showed the ability of AuNS to track surface receptors and cancer specific biomarkers through surface enhanced Raman spectroscopy *in vitro*, *in vivo* and *ex vivo*. First, 2-dimensional SERS cellular map of EGFR and PD-L1 were visualized with high spatiotemporal resolution. *In vivo* longitudinal Raman analysis demonstrated the systematically delivery and accumulation of AuNS in breast cancer tumors. Raman signals corresponding to both PD-L1 and EGFR appeared and intensified at six-hour post-injection, indicating successful detection of both receptors. In addition, both Raman peaks decreased by 30% when targeted receptors were pre-

blocked, showing the sensitivity and specificity of our platform in distinguishing tumors with varied expression of PD-L1 and EGFR. *Ex vivo* Raman maps of the tumor section revealed AuNS localization in well-vascularized areas. Quantifying Raman signals allowed assessment of biomarkers with near cellular resolution.

In chapter 4, we engineered AuNS for multimodal PET and SERS imaging to simultaneously detect both PD-L1 and CD8. The biocompatibility of AuNS was studied using serum metabolite level, complete blood count, and H&E staining. PET imaging showed 3-dimensional, whole body imaging of mice, allowing identification of melanoma tumors. SERS spectra provided molecular information of the tumor and assessment of PD-L1 and CD8 levels. Raman intensities decreased by 40-50% when targeted receptors were blocked with antibodies, again, showing the sensitivity and specificity of our platform in distinguishing tumors with varied expression of PD-L1 and CD8. We not only examined the diagnostic capability of the designed AuNS, we also demonstrated their ability to monitor immunotherapy treatment responses. Mice treated with CD137 and PD-L1 therapy showed an elevation in CD8+ T cells infiltration, which was successfully observed by PET/SERS. We validated our findings with both flow cytometry and immunohistochemistry.

In chapter 5, labeled free Raman spectroscopy was performed on MDA-MB-231 cells treated with small molecular inhibitor, Trametinib. Raman footprints revealed the changes in both phosphatidylcholine and phosphatidylinositol due to the inhibition of MEK/ERK pathway. Principle component analysis of cell treated with different Trametinib concentrations were discriminated and showed clustering. PCA allowed us to understand the changes in cell metabolism using Raman signatures.

6.2 Future Outlook

Significant future work is motivated and promised by the results presented in this dissertation. While AuNS have been shown to be of great prospects in cancer therapeutics and imaging, further toxicity and clearance pathways of AuNS should be studied to investigate their clinical translation potential. Understanding dosage dependent and long-term toxicity of AuNS will help to better understand the biocompatibility and safety of AuNS. In addition, I have only shown clearance of AuNS *in vivo* up to 15 days. The fate of AuNS after mononuclear phagocyte system uptake is unclear, thus long-term clearance (months to years) of AuNS should be investigated. The limitation for our platforms remains the delivery of light/laser and/or AuNS to the diseased area. The blood-brain barrier does not allow entry of AuNS, thus brain cancer patients may not benefit from this nanoparticle-based technique. Light delivery to tumor lesions for intestinal or stomach cancer can also be challenging, thus limiting the feasibility of light-based imaging or therapy techniques. Advanced surgical endoscopic that can potentially be combined with laser or optical fibers might be able to overcome such limitations, but further research will be needed.

Next, the *in vitro* photothermal-chemotherapy shown in this dissertation should be studied in *in vivo* settings as the efficiency of co-delivery of both AuNS and LTSLs with intravenous injection is unclear. To further improve the platform, instead of gold nanostructures and liposomes being separate entities, gold-coated liposome hybrids will help to improve therapeutic results. AuNS-mediated hyperthermia combined with other therapeutic modalities should be investigated. Small molecule drugs can be potentially encapsulated in low temperature sensitive liposomes for light-controlled triggered drug release. In addition, heat therapy and certain chemotherapies have shown to promote cancer immunity, thus combining AuNS photothermal therapy with cancer

vaccine or checkpoint blockage therapy can potentially result in long-term, memory T cell anti-tumor effects.

Future work for AuNS-based SERS or multimodal PET/SERS imaging include applying the platform to different tumor types, such as head and neck cancers, prostate cancers and pancreatic cancers. SERS imaging of non-superficial tumors can be achieved through minimally invasive optical probe to both deliver laser radiation and collect Raman scattering data. Thus, AuNS-mediated SERS or PET/SERS technique is not limited to a particular type of cancer. The challenges of a nanoparticle-based system is the accumulation in liver and spleen (mononuclear phagocyte system). Thus, the limitation of the platform would be detecting primary tumor or metastasis at the MPS system. To circumvent this issue, different surface modification techniques of AuNS can be used. For example, using different molecular weight polyethylene (PEG) to coat the surface or using higher PEG density. Next, one should evaluate the detection sensitivity and specificity of the imaging platform in mice bearing orthotropic tumor models or patient-derived tumor models to better show the potential of clinical translation. Due to the narrow bandwidth of Raman peaks, additional immuno-markers or cancer-specific receptors (third or even fourth target) can be detected simultaneously. Lastly, to achieve extended imaging study (more than 3 days), long half-life radionuclide, ^{89}Zr and ^{67}Ga (3.3 days) should be explored.

Label-free Raman spectroscopy utilized to monitor treatment responses is not limited to small molecule inhibitors. Both immunotherapy and radiation therapy can alter the content of extracellular matrix in the tumor stroma, which should be observable through Raman signatures. SERS substrates can also be designed to increase signal-to-noise ratio of Raman peaks without the use of Raman labels. SERS also allows the use of lower laser power during spectral acquisition without destruction of samples.

All our platforms are not disease specific. For example, both Rheumatoid arthritis (RA) and peripheral arterial disease (PAD) have shown similar enhanced permeability effects (leaky vasculature and capillaries) and thus passive uptake of nanoparticles. Heat therapy combined with thermosensitive liposome-mediated drug delivery (such as methotrexate) has great potential in treating RA. PET/SRES model can be used to target/image M2-like macrophages in RA to predict disease progression. Another inflammatory disease that can potentially benefit from our AuNS-mediated imaging and therapy platform is atherosclerosis. Lesioned vessel walls show enhanced permeability and neovessels of the vasa vasorum are generally leaky. By targeting the scavenger receptor of M2-like macrophages, atherosclerosis plaques can be identified with imaging and photothermal therapy can potentially shrink the plaque burden. Here, we show their application in cancer therapy and imaging, but we strongly encourage exploration of application of this technique in other disease models.

APPENDIX A

A.1 Doxorubicin Encapsulated Low Temperature Sensitive Liposomes

Materials: Lipids, membrane filter, membrane supports are purchase from Avanti Polar Lipid. Doxorubicin is purchase from Fisher Scientific (BP25161). PD-10 column is purchase from GE Healthcare Life Science (can be purchased from Fisher, 45-000-148).

1. Dissolve lipids in chloroform and remove organic solvent by desiccator

   10 mg of lipids: 90:10:4 (DPPC:MSPC:DSPE-PEG2000) in 2ml
2. Lipid film hydration
   - Hydrate with 2 ml of 300mM, pH 4.0 citrate buffer
     - Mix by vortex then mix by rotovap at 55 ^{0}C for 1 hour
   - Break down to smaller size by
     - Five freeze-thaw cycles using liquid nitrogen and 55 ^{0}C water bath.
     - Extrude at 60 ^{0}C – through 2 stacked 0.2um (for both 2ml) then through 2 stacked 0.1 um (remember to use membrane support at both side)
3. DOX solution
   - Use DOX:lipid = 0.05:1 (weight) ratio
   - Prepare Dox stock solution at 2 mg/ml with sterile water
   - Preheat rotovap to 37^{0}C
4. Direct Adjustment Method to pH = 7.5-7.6
   - Adjust the liposome solution to pH 7.5-7.6
   - Preheat liposome solution to 37^{0}C
   - Add Dox solution to liposome solution - shaking for 1hr at 37 ^{0}C.
5. Purification – removing free doxorubicin
   - Use PD-10 column
     - Equilibrate with sterile 25mM HEPES buffer saline for 4 times
     - Load 2.5 ml of sample (if sample less than 2.5ml, load the sample first (when the sample all go into the column, then add x amount of buffer to get 2.5ml)
     - After loading 2.5ml, add 3.5ml of buffer; Start collection when add 3.5ml of buffer

A.2 Doxorubicin Encapsulated None Temperature Sensitive Liposomes (NTSLs)

Materials: Lipids, membrane filter, membrane supports are purchase from Avanti Polar Lipid. Doxorubicin is purchase from Fisher Scientific (BP25161). PD-10 column is purchase from GE Healthcare Life Science (can be purchased from Fisher, 45-000-148).

6. Dissolve lipids in chloroform and remove organic solvent by desiccator

   10 mg of lipids: 75:50:3 (HSPC:CHOL:DSPE-PEG2000) in 2ml

7. Lipid film hydration
   - Hydrate with 2 ml of 300mM, pH 4.0 citrate buffer
     - Mix by vortex then mix by rotovap at 65 ^{0}C for 1 hour
   - Break down to smaller size by
     - Five freeze-thaw cycles using liquid nitrogen and 65 ^{0}C water bath.
     - Extrude at 65 ^{0}C – through 2 stacked 0.2um (for both 2ml) then through 2 stacked 0.1 um. (remember to use membrane support at both side)
8. DOX solution
   - Use DOX:lipid = 0.05:1 (weight) ratio
   - Prepare Dox stock solution at 2 mg/ml with sterile water
   - Preheat rotovap to 60^{0}C
9. Direct Adjustment Method to pH = 7.5-7.6
   - Adjust the liposome solution to pH 7.5-7.6
   - Preheat liposome solution to 60^{0}C
   - Add Dox solution to liposome solution - shaking for 1hr at 60 ^{0}C.
10. Purification – removing free doxorubicin
    - Use PD-10 column
      - Equilibrate with sterile 25mM HEPES buffer saline for 4 times
      - Load 2.5 ml of sample (if sample less than 2.5ml, load the sample first (when the sample all go into the column, then add x amount of buffer to get 2.5ml)
      - After loading 2.5ml, add 3.5ml of buffer; Start collection when add 3.5ml of buffer

A.3 MTT Assay

Materials: MTT salt (ThermoFisher, M5494), DMSO (Sigma, D2650), 96 well plate (Greiner Bio-One, 655090)

1. Prepare MTT solution
   - Weight out 5 mg MTT salt, add 1 ml of sterile 1x PBS (12 mM MTT)
   - Pipette up and down to mix, vortex or sonicate
   - Each 5 mg of MTT can provide sufficient reagent for 100 tests (10 µl per well)
   - Protect MTT from light at store at 4 ^{0}C. Once prepared, the solution should be used within a month
2. Label cells with MTT
   - For each test/well, prepare 100 µl of cDMEM + 10 µl of 12 mM MTT solution
   - After treatment is done, remove old media, and add 110 µl of MTT/cDMEM solution
   - Incubate at 37 ^{0}C for 2-4 hours depending on cell confluency. High confluency, 2 hours should be enough.
   - Once MTT labeling is done, remove 85 µl of media
   - Add 50 µl of DMSO to each well, mix thoroughly with pipette
   - Incubate 10 minutes at 37 ^{0}C
3. Reading
   - Make sure to pop any bubble for accurate reading
   - Read absorbance at 540 nm

A.4 Animal Tissue Preparation for ICP-MS

Materials Needed:
Scintillation vials, volumetric flasks, Trace-metal grade HCl (Fisher, A508-P500), Trace-metal grade HNO_3 (Fisher, A509-P500), two 2 L plastic bottles, PVDF 0.45 μm syringe filters (Fisher 50-550-494), 10 mL plastic syringes, BD 21 G needles (Fisher, 14-821-13N)

** Control blanks: samples that contain no tissue samples but go through the same sample preparation. Prepare 2-3 control blancks

1. Tissues should be collected and immediately frozen at -80 ºC (in 15 ml centrifuge tubes)
2. If you have access to a lyophilizer (Wilson and Guelcher's lab both has one), then lyophilize the tissue before proceeding to next step. This will remove water from the tissue and it will be easier for sample preparation.
    - Wrap a kimwipe on the 15 ml centrifuge with a robber band.
    - Place the cap on the centrifuge tube with kimwipe(not screwed right, just simply push it on)
3. Weigh scintillation vials before and with tissue and record the weight of tissue. Make sure to label your vials properly – We will do two readings for accuracy.
4. You only need 300-500 uL of 75% aqua regia per vial. So prepare enough aqua regia, using 3 parts of trace-metal grade HCl and 1 part trace-metal grade HNO_3 (volume ratio would be 4:1 HCl:HNO_3). The trace-metal grade is necessary since ICP-MS is very sensitive to any metal concentrations.
    - Prepare 75% aqua regia: simply assume the aqua regia you have is 100% and dilute with Mili-Q water.
    - Use our lab Mili-Q water
5. Now add 1-2 mL aqua regia to each vial. Since livers are a bit larger, you can add more (enough 75% AR to cover the tissue samples)
6. Let the tissue stand for ~72 hrs in aqua regia for complete dissolution. But check next day in case aqua regia has evaporated and more needs to be added to the vials.
7. Before covering the scintillation vials, remove paper/cardboard/aluminum piece from the white plastic cover. If it can easily removed – if not, it should be fine.
8. After 48-72 hrs, boil off the aqua regia with gentle heating. Be very careful, leave some liquid at the bottom of each vial or tissue will burn and turn brown.

9. Weight out 15 ml centrifuge tube and tare
10. Add 5 ml of 2% AR to the glass vials, wash the wall and transfer the samples to 15 ml centrifuge tube by putting a needle on a syringe to extract the samples from the glass vials and then removing the needle/replacing with a filter and filter the sample into a 15 ml centrifuge tube.
11. Add 4 ml of 2% AR to the glass vials, wash the wall. Repeat 10 with a new filter.
12. Put the 15ml centrifuge tube back to the scale, and add 2% AR until 10 mg (assuming water/tissue density = 1 mg/ml, so it will be 10 ml volume total).
13. Some tissues have higher gold accumulation: liver, spleen and may be tumor. These samples need to be diluted again. I diluted tumor samples by 10X (1 mL of original 10 mL diluted to 10 mL). All dilutions should be made with 2 % aqua regia.
14. Blanks (2% AR) between tumors and high reading samples: order…brain, lung, heart, stomach, tumor, blank, spleen, blank, kidney, liver, blank
15. Rosanne will prepare the gold standards

A.5 Nanostar Synthesis for PET/SERS

Materials: HEPES (Sigma, H4034), Gold (III) chloride trihydrate (Sigma, 520918), pMBA (TCI America), DTNB (TCI America), OPSS-PEG-NHS ester (JenKem Technology), anti-PD-L1 (BE0101), anti-CD8 (BE0004-1)
**Assuming 300 ml AuNS reaction, which will be enough for 8 mice (total = 600 ml AuNS, 300 ml pMBA/anti-PD-L1, 300 ml for DTNB/anti-CD8)

Day 1

1. AuNS synthesis

- 18 mL of Milli-Q water + 12 mL of HEPES → 50 mL centrifuge tube
- Shake in a yo-yo motion gently 30x
- Prepare 20 mM $HAuCl_4$ solution (turn off light)
    - 200 µL stock (100 mM) + 800 µL Milli-Q water → 1 mL vial
- Add 300 µL of 20 mM $HAuCl_4$ solution to HEPE solution
- Shake again in a yo-yo motion gently 50x
- Leave it at room temperature for 75 minutes
- Check UV-Vis (should be in 760-800 nm).

2. OPEE-PEG-NHS Ester linker and antibody reaction

- We are utilizing a
    - Antibody:OPSS-PEG-NHS Ester ~ 1:500 molar ratio assuming antibody MW = 150k g/mol and linker MW = 2300 g/mol
    - Volume ratio for antibody:OPSS-PEG-NHS = 9:1
    - Reaction buffer:100 mM sodium bicarbonate buffer at pH 8.5
- Thus, make ~ 460 ul reaction
    - 414 ul of 1 mg/ml antibody
        - dilute antibody with 100 mM sodium bicarbonate buffer
    - 46 ul of 80 mg/ml OPSS-PEG-NHS
        - dissolve OPSS-PEG-NHS powder in 100 mM sodium bicarbonate buffer
- Remember, OPSS-PEG-NHS Ester can hydrolyze very fast, so only add sodium bicarbonate buffer to the powder when the antibody is ready for reaction!! Mix OPSS-PEG-NHS Ester very fast and add to antibody immediately when ready.
- React at 4 ^{0}C for 24 hr on rotator

Day 2

1. **Prepare Raman tag**

   DTNB MW: 396.65 g/mol; pMBA MW: 154.18 g/mol

   - Prepare 10 mM pMBA and 10 mM DTNB
   - Aliquot some pMBA and DTNB and weight out outside of glovebox
   - Dissolve pMBA and DTNB in EtOH
   - Vortex
   - Dilute to 10 mM (might need serial dilution)

2. **Raman tag – AuNS reaction**

   - Add 30 µL of 10 mM DTNB or pMBA to 300 mL batch of AuNS, gently stir at 4ºC for 15 mins
   - After reaction is done, check UV-Vis (Expect a 4 – 6 nm shift)
   - Split into multiple 50 mL centrifuge tube (50 mL each), 6000 rpm for 20 minutes
   - Remove supernatant, resuspend in ~ 15 ml miliQ water
   - Check UV-Vis again

3. **Antibody – AuNS reaction**

   - Dilute AuNS solution to Extinction 12 for antibody reaction
   - For every 3.75 mL of AuNS @ extinction 12, add 50.4 µL of OPSS-PEG-antibody
   - Reaction at 4 ^{0}C for 24 hr on rotator
   - Check UV-Vis when reaction is done. Expect 20-25 nm shift (dilute AuNS 60x when chcking UV-Vis)

Day 3

1. **Prepare OPSS-PEG-NHS and DOTA**

   - NOTA MW: 655.4 g/mol // Linker MW: 2300 g/mol
   - Molar ratio = Linker : NOTA = 1 : 1 // Volume ratio = Linker : NOTA = 1 : 4
   - Reaction buffer:100 mM sodium bicarbonate buffer at pH 8.5
   - For every 1 mg of DOTA, dissolve it in 120 µL of 100 mM $NaHCO_3$ buffer
   - Thus:

     DOTA: every reaction, take 8 mg of DOTA, 960 µL of 100 mM $NaHCO_3$OPSS-PEG-NHS linker: take an aliquot (should be large amount, ~ 35 mg) of OPSS-PEG-NHS dissolve in of 100 mM $NaHCO_3$

    - 35 mg dissolved in 240 µL (a bit access of linker)
- Adjust DOTA pH to 8.4 with 0.5 M sodium carbonate (Na_2CO_3)

  ** make sure DOTA pH is adjusted and ready before dissolving linker in sodium carbonate buffer
- Leave it on rotator at 4 ºC for 8 – 10 hrs.

2. **DOTA- AuNS Reaction**
    - Confirm the 20-25 nm shift after antibody- AuNS reaction
    - Split AuNS solution into 15 ml centrifuge tube
    - Dilute the volume by 2 fold with miliQ water, so the pellet and supernatant separate well. For example, split 15 ml of Ext 12 AuNS to three15 ml centrifuge tube, so 5 ml of AuNS/tube, dilute with extra 5 ml miliQ water.
    - Centrifuge: 4000 rpm for 10 mins
    - Remove supernatant, resuspend in 5 ml trace grade water
    - Check UV-Vis and dilute to Ext 12
    - For every 3.75 mL of AuNS @ extinction 12, add 134.4 µL of linker-DOTA.
    - Leave it on rotator at 4 ºC for 12 hrs/overnight

Day 4 (Day of Cu64 Chelation = Wednesday)

- Check UV-Vis of fully functionalized AuNS (should see 3-5 nm shift)
- Dilute the volume 2 fold with trace grade water , so the pellet and supernatant separate well
- Centrifuge: 4000 rpm for 10 mins; Remove supernatant, resuspend in ~ 1 ml trace grade water
- Check UV-Vis (120x dilution of AuNS), Calculate AuNS concentration. The target is 5.5 mg/mL. Use formula: $9.38\frac{\text{mg}}{\text{mL}} \times \frac{\mathbf{x} \times 120}{1.64 \times 60} = \_\_\_\_\ \text{mg/mL}$ x = extinction from UV-Vis
- If final concentration is not 5.5 mg/m, dilute with trace grade water
- Goal is to have ~ 0.8 mCi per 250 ul AuNS = approximately 1.2 mg/mouse

A.6 YUMM 2.1 and YUMM 10.1 Cell preparation for Injection

Materials: Media: DMEM/F-12, HEPES (11330-032) + 10% FBS (Sigma, F8067) + 1% Penn/Strap + 1% MEM non-essential amino acid (Sigma, M7145). 1XPBS, TrypLE (notice, not Trypsin), nDMEM and cDMEM. Needle for injection (Fisher, 22-257-136)

** Cells should be at 50-70% confluent. If the cells are not at the right confluency, do not proceed, split again.

** remember to shave the mice a day before cell injection

1. Prewarm: nDMEM, 1x PBS, TrypLE, for ~1 hr at 37 ^{0}C
2. Remove old media with aspirator
3. Add 10 ml 1xPBS to wash the cell; remove with aspirator
4. Add 7 ml TrypLE, incubate at 37 ^{0}C for 3 minutes
5. Check under microscope to see make sure the cells have been successfully disassociated
6. Add 7 ml nDMEM to quickly wash every flask (be fast!)
7. Collect all the cell solutions im 50 ml centrifuge tubes
8. Centrifuge the cell at 2000 rpm for 2 min, remove supernatant
9. Resuspend cell pellet in 1xPBS (concentrated, only few ml)
10. Mix well, pass through cell strainer
11. Remove 100 uL, dilute 100x fold with 1xPBS, count with scepter
12. Dilute the cell to desired concentration (mice should be injected with 100-200 ul of cell)
    a. For example, 1 million cells/mouse -> dilute to 10 million cells/ml etc
13. Place the cells on ice. Cells will be viable for 1 hour
14. Remember to inverse the Eppendorf tubes to mix before withdrawing with syringes

A.7 Label Free Raman Mapping Cell Preparation

Materials: Trametinib (Selleck Chemical, NC0592237), Alpelisib (50-136-3003, Selleck Chemical), Taxol (Invitrogen, P3456), CaF2 Disk (Crystran, CAFP20-2R), Fixative solution (ThermoFisher, FB002)

1. Seeding cells
   - seeded on 6 well plate at ~ approximately 60% confluence.
   - Let the cells attach (~ overnight) before adding the drug
2. Drug incubation
   - Once the cells have attached on the plate, different concentrations of MEKi ,PI3Ki, taxol, or any combination in cDMEM were added to cells (2 ml).
   - drugs might need to be prepared in serial dilution
   - Incubate for 72 hour
3. Seeding Cells on CaF2 Disk
   - Auto-clave CaF2 disks
   - Coat CaF2 disks with ~ 0.5 ml of poly-l-lysine for 15 minutes, remove poly-l-lysine
     - I would suggest to place CaF2 disks on 6 well plates
   - Remove old media and add 2 ml of 1xPBS to wash
   - Add ~ 0.5 ml of trypsin to disassociate the cells, incubate at 37 ^{0}C for 3-4 minutes
   - Add 2 ml of cDMDM to quench reaction and wash the cells
   - Centrifuged detached cells at 200 g for 7 min
   - Remove supernatant, depending on the vability of cells, you might resuspend the cells in different amount of cDMEM. You want to seed ~ 50% of cells on CaF2. Make sure the cells are well mixed, so you will have single cells for mapping.
   - Seeding volume should be 400 ul, drop the cells on CaF2 disk
   - Move the CaF2 disk back to incubator - Be very careful!!
4. Fix cells
   - After seeding, wait for overnight so the cells can re-attach.
   - Remove media and wash with 1xPBS three times (~ 2 ml)
   - Gently dip CaF2 disk in in 4% formaldehyde (methanol-free)
   - Fix the cell at room temperature for 10 minutes
   - After fixing, washed the cells with 1xPBS three times

- Dried at 4^0C

5. Raman Mapping
   - Before Raman mapping, move the CaF disk to room temperature to be completely dry
   - Use 100x objective to visualize the cell
   - Find 2-4 neighboring single cells for rectangular map. Make sure not to select rounded cells that look died
   - Raman mapping at 2 μm by 2 μm resolution with a 785 nm laser with 1200 lines/mm grating with 10 s acquisition time.
   - Mapping should take 6-20 hours depending on how big the map is
6. Data Analysis
   - Use Renishaw software to remove cosmic ray (with nearest neighbor method)
   - Background subtraction: Savitzsky and Golay filter (order of 5 and coefficient value of 61). And modified polyfit method using a 7^{th} order polynomial with a threshold of 0.0005.

For Mass Spectroscopy – follow the same procedure for Step 1 and 2

At least have 1-2x 6 well plates full of cells

3. After treatment, wash with 2 ml 1xPBS per well, add 0.5 ml of trypsin of de-attach cells, incubate at 37 ^{0}C for 3-4 minutes, add 2 ml of cDMEEM to quench reaction
4. Centrifuge at 200 g for 7 min
5. Remove supernatant, resuspend cells in 1xPBS
6. Transfer the cells into a 15 ml centrifuge tube
   - Remember to record the weight of centrifuge tube
7. Place in lyophilizer to remove any solvent (few hours should be enough)
8. Obtain the weight of cell

REFERENCES

1. Kreuter, J., Nanoparticles-a historical perspective. *Int. J. Pharm.* **2007,** *331* (1), 1-10.

2. Daldrup-Link, H. E., Ten things you might not know about iron oxide nanoparticles. *Radiology* **2017,** *284* (3), 616-629.

3. Singh, P.; Pandit, S.; Mokkapati, V. R. S. S.; Garg, A.; Ravikumar, V.; Mijakovic, I., Gold nanoparticles in diagnostics and therapeutics for human cancer. *Int. J. Mol. Sci.* **2018,** *19* (7), 1979.

4. Hanahan, D.; Weinberg, R. A., Hallmarks of cancer: the next generation. *Cell* **2011,** *144* (5), 646-74.

5. McCain, J., The MAPK (ERK) Pathway: Investigational Combinations for the Treatment Of BRAF-Mutated Metastatic Melanoma. *P T.* **2013,** *38* (2), 96-108.

6. Lane, D. P., p53, guardian of the genome. *Nature* **1992,** *358* (6381), 15-16.

7. Hu, M.; Chen, J.; Li, Z. Y.; Au, L.; Hartland, G. V.; Li, X.; Marquez, M.; Xia, Y., Gold nanostructures: engineering their plasmonic properties for biomedical applications. *Chem. Soc. Rev.* **2006,** *35* (11), 1084-94.

8. Indrasekara, A. S.; Paladini, B. J.; Naczynski, D. J.; Starovoytov, V.; Moghe, P. V.; Fabris, L., Dimeric gold nanoparticle assemblies as tags for SERS-based cancer detection. *Adv. Healthc. Mater.* **2013,** *2* (10), 1370-6.

9. Huschka, R.; Neumann, O.; Barhoumi, A.; Halas, N. J., Visualizing light-triggered release of molecules inside living cells. *Nano Lett.* **2010,** *10* (10), 4117-4122.

10. Webb, J. A.; Bardhan, R., Emerging Advances in Nanomedicine with Engineered Gold Nanostructures. *Nanoscale* **2014,** *6* (5), 2502-30.

11. Huang, X.; El-Sayed, M. A., Plasmonic photo-thermal therapy (PPTT). *Alexandria Med. J.* **2011,** *47* (1), 1-9.

12. Topete, A.; Alatorre-Meda, M.; Iglesias, P.; Villar-Alvarez, E. M.; Barbosa, S.; Costoya, J. A.; Taboada, P.; Mosquera, V., Fluorescent drug-loaded, polymeric-based, branched gold nanoshells for localized multimodal therapy and imaging of tumoral cells. *ACS Nano* **2014,** *8* (3), 2725-2738.

13. Mahan, M. M.; Doiron, A. L., Gold Nanoparticles as X-Ray, CT, and Multimodal Imaging Contrast Agents: Formulation, Targeting, and Methodology. *J. Nanomater.* **2018,** *2018*, 15.

14. Meir, R.; Shamalov, K.; Sadan, T.; Motiei, M.; Yaari, G.; Cohen, C. J.; Popovtzer, R., Fast image-guided stratification using anti-programmed death ligand 1 gold nanoparticles for cancer immunotherapy. *ACS Nano* **2017**.

15. Meir, R.; Shamalov, K.; Betzer, O.; Motiei, M.; Horovitz-Fried, M.; Yehuda, R.; Popovtzer, A.; Popovtzer, R.; Cohen, C. J., Nanomedicine for cancer immunotherapy: tracking cancer-specific T-cells in vivo with gold nanoparticles and CT imaging. *ACS Nano* **2015,** *9* (6), 6363-6372.

16. Xie, H.; Wang, Z. J.; Bao, A.; Goins, B.; Phillips, W. T., In vivo PET imaging and biodistribution of radiolabeled gold nanoshells in rats with tumor xenografts. *Int. J. Pharm.* **2010,** *395* (1-2), 324-30.

17. Zhao, Y.; Sultan, D.; Detering, L.; Cho, S.; Sun, G.; Pierce, R.; Wooley, K. L.; Liu, Y., Copper-64-alloyed gold nanoparticles for cancer imaging: improved radiolabel stability and diagnostic accuracy. *Angew. Chem. Int. Ed. Engl.* **2014,** *53* (1), 156-9.

18. Lee, S. B.; Lee, S.-W.; Jeong, S. Y.; Yoon, G.; Cho, S. J.; Kim, S. K.; Lee, I.-K.; Ahn, B.-C.; Lee, J.; Jeon, Y. H., Engineering of radioiodine-labeled gold core–shell nanoparticles as efficient nuclear medicine imaging agents for trafficking of dendritic cells. *ACS Appl. Mater. Interfaces* **2017,** *9* (10), 8480-8489.

19. Bhatnagar, P.; Li, Z.; Choi, Y.; Guo, J.; Li, F.; Lee, D. Y.; Figliola, M.; Huls, H.; Lee, D. A.; Zal, T.; Li, K. C.; Cooper, L. J., Imaging of genetically engineered T cells by PET using gold nanoparticles complexed to Copper-64. *Integr. Biol.* **2013,** *5* (1), 231-8.

20. Day, E. S.; Thompson, P. A.; Zhang, L.; Lewinski, N. A.; Ahmed, N.; Drezek, R. A.; Blaney, S. M.; West, J. L., Nanoshell-mediated photothermal therapy improves survival in a murine glioma model. *J. Neurooncol.* **2011,** *104* (1), 55-63.

21. Shao, J.; Griffin, R. J.; Galanzha, E. I.; Kim, J. W.; Koonce, N.; Webber, J.; Mustafa, T.; Biris, A. S.; Nedosekin, D. A.; Zharov, V. P., Photothermal nanodrugs: potential of TNF-gold nanospheres for cancer theranostics. *Sci. Rep.* **2013,** *3*, 1293.

22. Shen, S.; Tang, H.; Zhang, X.; Ren, J.; Pang, Z.; Wang, D.; Gao, H.; Qian, Y.; Jiang, X.; Yang, W., Targeting mesoporous silica-encapsulated gold nanorods for chemo-photothermal therapy with near-infrared radiation. *Biomaterials* **2013,** *34* (12), 3150-8.

23. Brown, S. D.; Nativo, P.; Smith, J.-A.; Stirling, D.; Edwards, P. R.; Venugopal, B.; Flint, D. J.; Plumb, J. A.; Graham, D.; Wheate, N. J., Gold Nanoparticles for the Improved Anticancer Drug Delivery of the Active Component of Oxaliplatin. *J. Am. Chem. Soc.* **2010,** *132* (13), 4678-4684.

24. Lee, J.-S.; Green, J. J.; Love, K. T.; Sunshine, J.; Langer, R.; Anderson, D. G., Gold, Poly(β-amino ester) nanoparticles for small interfering RNA delivery. *Nano Lett.* **2009,** *9* (6), 2402-2406.

25. Webb, J. A.; Erwin, W. R.; Zarick, H. F.; Aufrecht, J.; Manning, H. W.; Lang, M. J.; Pint, C. L.; Bardhan, R., Geometry-Dependent Plasmonic Tunability and Photothermal Characteristics of Multibranched Gold Nanoantennas. *J. Phys. Chem. C* **2014,** *118* (7), 3696-3707.

26. Mahmood, J.; Shukla, H.; Soman, S.; Samanta, S.; Singh, P.; Kamlapurkar, S.; Saeed, A.; Amin, N.; Vujaskovic, Z., Immunotherapy, radiotherapy, and hyperthermia: A combined therapeutic approach in pancreatic cancer treatment. *Cancers* **2018,** *10* (12), 469.

27. Falk, M. H.; Issels, R. D., Hyperthermia in oncology. *Int. J. Hyperthermia* **2009,** *17* (1), 1-18.

28. Song, C. W.; Park, H. J.; Lee, C. K.; Griffin, R., Implications of increased tumor blood flow and oxygenation caused by mild temperature hyperthermia in tumor treatment. *Int. J. Hyperthermia* **2005,** *21* (8), 761-7.

29. Jain, R. K., Normalization of tumor vasculature: an emerging concept in ntiangiogenic therapy. *Science* **2005,** *307* (5706), 58-62.

30. Takahashi, I.; Emi, Y.; Hasuda, S.; Kakeji, Y.; Maehara, Y.; Sugimachi, K., Clinical application of hyperthermia combined with anticancer drugs for the treatment of solid tumors. *Surgery* **2002,** *131* (1), S78-S84.

31. Datta, N. R.; Ordonez, S. G.; Gaipl, U. S.; Paulides, M. M.; Crezee, H.; Gellermann, J.; Marder, D.; Puric, E.; Bodis, S., Local hyperthermia combined with radiotherapy and-/or chemotherapy: recent advances and promises for the future. *Cancer Treat. Rev.* **2015,** *41* (9), 742-53.

32. Toraya-Brown, S.; Fiering, S., Local tumour hyperthermia as immunotherapy for metastatic cancer. *Int. J. Hyperthermia* **2014,** *30* (8), 531-9.

33. Yagawa, Y.; Tanigawa, K.; Kobayashi, Y.; Yamamoto, M., Cancer immunity and therapy using hyperthermia with immunotherapy, radiotherapy, chemotherapy, and surgery. *J. of Cancer Metastasis Treat.* **2017,** *3* (10), 218.

34. Liu, Y.; Maccarini, P.; Palmer, G. M.; Etienne, W.; Zhao, Y.; Lee, C. T.; Ma, X.; Inman, B. A.; Vo-Dinh, T., Synergistic immuno photothermal nanotherapy (SYMPHONY) for the treatment of unresectable and metastatic cancers. *Sci. Rep.* **2017,** *7* (1), 8606.

35. Kong, G.; Anyarambhatla, G.; Petros, W. P.; Braun, R. D.; Colvin, O. M.; Needham, D.; Dewhirst, M. W., Efficacy of liposomes and hyperthermia in a human tumor xenograft model: importance of triggered drug release. *Cancer research* **2000,** *60* (24), 6950-6957.

36. Landon, C. D.; Park, J. Y.; Needham, D.; Dewhirst, M. W., Nanoscale drug delivery and hyperthermia: the materials design and preclinical and clinical testing of low temperature-sensitive liposomes used in combination with mild hyperthermia in the treatment of local cancer. *Open Nanomed. J.* **2011,** *3*, 38-64.

37. Wei, H.; Hossein Abtahi, S. M.; Vikesland, P. J., Plasmonic colorimetric and SERS sensors for environmental analysis. *Environ. Sci. Nano* **2015,** *2* (2), 120-135.

38. Xie, Y.; Xu, L.; Wang, Y.; Shao, J.; Wang, L.; Wang, H.; Qian, H.; Yao, W., Label-free detection of the foodborne pathogens of Enterobacteriaceae by surface-enhanced Raman spectroscopy. *Anal. Methods* **2013,** *5* (4), 946-952.

39. Jiang, X.; Jiang, Z.; Xu, T.; Su, S.; Zhong, Y.; Peng, F.; Su, Y.; He, Y., Surface-enhanced Raman scattering-based sensing in vitro: facile and label-free detection of apoptotic cells at the single-cell level. *Anal. Chem.* **2013,** *85* (5), 2809-16.

40. Xu, M.; Ma, X.; Wei, T.; Lu, Z. X.; Ren, B., In situ imaging of live-cell extracellular pH during cell apoptosis with surface-enhanced Raman spectroscopy. *Anal. Chem.* **2018**.

41. Cao, Y.; Li, D. W.; Zhao, L. J.; Liu, X. Y.; Cao, X. M.; Long, Y. T., Highly selective detection of carbon monoxide in living cells by palladacycle carbonylation-based surface enhanced Raman spectroscopy nanosensors. *Anal. Chem.* **2015,** *87* (19), 9696-701.

42. Kuku, G.; Altunbek, M.; Culha, M., Surface-enhanced Raman scattering for label-free living single cell analysis. *Anal. Chem.* **2017,** *89* (21), 11160-11166.

43. Nima, Z. A.; Mahmood, M.; Xu, Y.; Mustafa, T.; Watanabe, F.; Nedosekin, D. A.; Juratli, M. A.; Fahmi, T.; Galanzha, E. I.; Nolan, J. P.; Basnakian, A. G.; Zharov, V. P.; Biris, A. S., Circulating tumor cell identification by functionalized silver-gold nanorods with multicolor, super-enhanced SERS and photothermal resonances. *Sci. Rep.* **2014,** *4*, 4752.

44. Karabeber, H.; Huang, R.; Iacono, P.; Samii, J. M.; Pitter, K.; Holland, E. C.; Kircher, M. F., Guiding brain tumor resection using surface-enhanced Raman scattering nanoparticles and a hand-held Raman scanner. *ACS Nano* **2014,** *8* (10), 9755-9766.

45. Palucka, K.; Banchereau, J., Dendritic-cell-based therapeutic cancer vaccines. *Immunity* **2013,** *39* (1), 38-48.

46. Weber, J.; Haberkorn, U.; Mier, W., Cancer stratification by molecular imaging. *Int. J. Mol. Sci* **2015,** *16* (3), 4918-46.

47. Vaneycken, I.; D'Huyvetter, M.; Hernot, S.; De Vos, J.; Xavier, C.; Devoogdt, N.; Caveliers, V.; Lahoutte, T., Immuno-imaging using nanobodies. *Curr. Opin. Biotechnol.* **2011,** *22* (6), 877-81.

48. Dreaden, E. C.; Mwakwari, S. C.; Sodji, Q. H.; Oyelere, A. K.; El-Sayed, M. A., Tamoxifen-poly(ethylene glycol)-thiol gold nanoparticle conjugates: enhanced potency and selective delivery for breast cancer treatment. *Bioconjugate Chem.* **2009,** *20* (12), 2247-2253.

49. Patra, C. R.; Bhattacharya, R.; Mukherjee, P., Fabrication and functional characterization of goldnanoconjugates for potential application in ovarian cancer. *J. Mater. Chem.* **2010,** *20* (3), 547-554.

50. Hosta, L.; Pla-Roca, M.; Arbiol, J.; López-Iglesias, C.; Samitier, J.; Cruz, L. J.; Kogan, M. J.; Albericio, F., Conjugation of Kahalalide F with gold nanoparticles to enhance in vitro antitumoral activity. *Bioconjugate Chem.* **2009,** *20* (1), 138-146.

51. Wang, F.; Wang, Y.-C.; Dou, S.; Xiong, M.-H.; Sun, T.-M.; Wang, J., Doxorubicin-tethered responsive gold nanoparticles facilitate intracellular drug delivery for overcoming multidrug resistance in cancer cells. *ACS Nano* **2011,** *5* (5), 3679-3692.

52. Huschka, R.; Barhoumi, A.; Liu, Q.; Roth, J. A.; Ji, L.; Halas, N. J., Gene silencing by gold nanoshell-mediated delivery and laser-triggered release of antisense oligonucleotide and siRNA. *ACS Nano* **2012,** *6* (9), 7681-7691.

53. Barhoumi, A.; Huschka, R.; Bardhan, R.; Knight, M. W.; Halas, N. J., Light-induced release of DNA from plasmon-resonant nanoparticles: Towards light-controlled gene therapy. *Chem. Phys. Lett.* **2009,** *482* (4-6), 171-179.

54. Yavuz, M. S.; Cheng, Y.; Chen, J.; Cobley, C. M.; Zhang, Q.; Rycenga, M.; Xie, J.; Kim, C.; Song, K. H.; Schwartz, A. G.; Wang, L. V.; Xia, Y., Gold nanocages covered by smart polymers for controlled release with near-infrared light. *Nat. Mater.* **2009,** *8* (12), 935-9.

55. Agarwal, A.; Mackey, M. A.; El-Sayed, M. A.; Bellamkonda, R. V., Remote triggered release of doxorubicin in tumors by synergistic application of thermosensitive liposomes and gold nanorods. *ACS Nano* **2011,** *5* (6), 4919-4926.

56. Patel, S. K.; Janjic, J. M., Macrophage targeted theranostics as personalized nanomedicine strategies for inflammatory diseases. *Theranostics* **2015,** *5* (2), 150-72.

57. Kim, H. J.; Lee, S. M.; Park, K. H.; Mun, C. H.; Park, Y. B.; Yoo, K. H., Drug-loaded gold/iron/gold plasmonic nanoparticles for magnetic targeted chemo-photothermal treatment of rheumatoid arthritis. *Biomaterials* **2015,** *61*, 95-102.

58. Manzoor, A. A.; Lindner, L. H.; Landon, C. D.; Park, J. Y.; Simnick, A. J.; Dreher, M. R.; Das, S.; Hanna, G.; Park, W.; Chilkoti, A.; Koning, G. A.; ten Hagen, T. L.; Needham, D.; Dewhirst, M. W., Overcoming limitations in nanoparticle drug delivery: triggered, intravascular release to improve drug penetration into tumors. *Cancer research* **2012,** *72* (21), 5566-75.

59. Kneidl, B.; Peller, M.; Winter, G.; Lindner, L. H.; Hossann, M., Thermosensitive liposomal drug delivery systems: state of the art review. *Int. J. Nanomed.* **2014,** *9*, 4387-98.

60. Li, L.; ten Hagen, T. L.; Hossann, M.; Suss, R.; van Rhoon, G. C.; Eggermont, A. M.; Haemmerich, D.; Koning, G. A., Mild hyperthermia triggered doxorubicin release from optimized stealth thermosensitive liposomes improves intratumoral drug delivery and efficacy. *J. Control. Release* **2013,** *168* (2), 142-50.

61. Contreras-Cáceres, R.; Pacifico, J.; Pastoriza-Santos, I.; Pérez-Juste, J.; Fernández-Barbero, A.; Liz-Marzán, L. M., Au@pNIPAM thermosensitive nanostructures: control over ahell cross-linking, overall dimensions, and core growth. *Adv. Funct. Mater.* **2009,** *19* (19), 3070-3076.

62. Fernandez-Lopez, C.; Polavarapu, L.; Solis, D. M.; Taboada, J. M.; Obelleiro, F.; Contreras-Caceres, R.; Pastoriza-Santos, I.; Perez-Juste, J., Gold nanorod–pNIPAM hybrids with reversible plasmon coupling: synthesis, modeling, and SERS properties. *ACS Appl. Mater. Interfaces* **2015,** *7* (23), 12530-8.

63. Webb, J. A.; Aufrecht, J.; Hungerford, C.; Bardhan, R., Ultrasensitive analyte detection with plasmonic paper dipsticks and swabs integrated with branched nanoantennas. *J. Mater. Chem. C* **2014,** *2* (48), 10446-10454.

64. Wang, A. Z.; Langer, R.; Farokhzad, O. C., Nanoparticle delivery of cancer drugs. *Annual review of medicine* **2012,** *63*, 185-98.

65. Petros, R. A.; DeSimone, J. M., Strategies in the design of nanoparticles for therapeutic applications. *Nat. Rev. Drug Discovery* **2010,** *9* (8), 615-27.

66. Davis, M. E.; Chen, Z. G.; Shin, D. M., Nanoparticle therapeutics: an emerging treatment modality for cancer. *Nat. Rev. Drug Discovery* **2008,** *7* (9), 771-82.

67. Bertrand, N.; Wu, J.; Xu, X.; Kamaly, N.; Farokhzad, O. C., Cancer nanotechnology: the impact of passive and active targeting in the era of modern cancer biology. *Adv. Drug Deliv. Rev.* **2014,** *66*, 2-25.

68. Landon, C. D.; Park, J.-Y.; Needham, D.; Dewhirst, M. W., Nanoscale drug delivery and hyperthermia: the materials design and preclinical and clinical testing of low temperature-sensitive liposomes used in combination with mild hyperthermia in the treatment of local cancer. *Open Nanomed. J.* **2011,** *3*, 38.

69. Needham, D.; Park, J.-Y.; Wright, A. M.; Tong, J., Materials characterization of the low temperature sensitive liposome (LTSL): effects of the lipid composition (lysolipid and DSPE–PEG2000) on the thermal transition and release of doxorubicin. *Faraday Discuss.* **2013,** *161*, 515-534.

70. Mitra, S.; Gaur, U.; Ghosh, P. C.; Maitra, A. N., Tumour targeted delivery of encapsulated dextran–doxorubicin conjugate using chitosan nanoparticles as carrier. *J. Control. Release* **2001,** *74* (1–3), 317-323.

71. Chang, H. I.; Yeh, M. K., Clinical development of liposome-based drugs: formulation, characterization, and therapeutic efficacy. *Int. J. Nanomed.* **2012,** *7*, 49-60.

72. Kouloulias, V. E.; Dardoufas, C. E.; Kouvaris, J. R.; Gennatas, C. S.; Polyzos, A. K.; Gogas, H. J.; Sandilos, P. H.; Uzunoglu, N. K.; Malas, E. G.; Vlahos, L. J., Liposomal doxorubicin in conjunction with reirradiation and local hyperthermia treatment in recurrent breast cancer: a phase I/II trial. *Clin. Cancer Res.* **2002,** *8* (2), 374-382.

73. Wust, P.; Hildebrandt, B.; Sreenivasa, G.; Rau, B.; Gellermann, J.; Riess, H.; Felix, R.; Schlag, P. M., Hyperthermia in combined treatment of cancer. *Lancet Oncol.* **2002,** *3* (8), 487-497.

74. Rhim, H.; Dodd III, G. D.; Chintapalli, K. N.; Wood, B. J.; Dupuy, D. E.; Hvizda, J. L.; Sewell, P. E.; Goldberg, S. N., Radiofrequency thermal ablation of abdominal tumors: lessons learned from complications. *Radiographics* **2004,** *24* (1), 41-52.

75. Xiaoyong, Y.; Jianjun, D.; Youjun, L. In *Advances in hyperthermia technology*, Engineering in Medicine and Biology Society, 2005. IEEE-EMBS 2005. 27th Annual International Conference of the, Shanghai, 17-18 Jan. 2006; Shanghai, 2005; pp 6766-6769.

76. Habash, R. W.; Bansal, R.; Krewski, D.; Alhafid, H. T., Thermal therapy, part 2: hyperthermia techniques. *CRC Crit. Rev. Bioeng.* **2006,** *34* (6), 491–542.

77. Wu, C.-P.; Hsieh, C.-H.; Wu, Y.-S., The emergence of drug transporter-mediated multidrug resistance to cancer chemotherapy. *Mol. Pharmaceutics* **2011,** *8* (6), 1996-2011.

78. Andre, F.; Zielinski, C. C., Optimal strategies for the treatment of metastatic triple-negative breast cancer with currently approved agents. *Annals of oncology : official journal of the European Society for Medical Oncology / ESMO* **2012,** *23 Suppl 6*, vi46-51.

79. O'Reilly, E. A.; Gubbins, L.; Sharma, S.; Tully, R.; Guang, M. H.; Weiner-Gorzel, K.; McCaffrey, J.; Harrison, M.; Furlong, F.; Kell, M.; McCann, A., The fate of chemoresistance in triple negative breast cancer (TNBC). *BBA clinical* **2015,** *3*, 257-75.

80. Wang, L.; Lin, X.; Wang, J.; Hu, Z.; Ji, Y.; Hou, S.; Zhao, Y.; Wu, X.; Chen, C., Novel insights into combating cancer chemotherapy resistance using a plasmonic nanocarrier: enhancing drug sensitiveness and accumulation simultaneously with localized mild photothermal stimulus of femtosecond pulsed laser. *Adv. Funct. Mater.* **2014,** *24* (27), 4229-4239.

81. Dong, X.; Mumper, R. J., Nanomedicinal strategies to treat multidrug-resistant tumors: current progress. *Nanomedicine* **2010,** *5* (4), 597-615.

82. Souslova, T.; Averill-Bates, D. A., Multidrug-resistant hela cells overexpressing MRP1 exhibit sensitivity to cell killing by hyperthermia: interactions with etoposide. *Int. J. Radiat. Oncol., Biol., Phys.* **2004,** *60* (5), 1538-51.

83. Klostergaard, J.; Leroux, M. E.; Auzenne, E.; Khodadadian, M.; Spohn, W.; Wu, J. Y.; Donato, N. J., Hyperthermia engages the intrinsic apoptotic pathway by enhancing upstream caspase activation to overcome apoptotic resistance in MCF-7 breast adenocarcinoma cells. *J. Cell. Biochem.* **2006,** *98* (2), 356-69.

84. Wrzal, P. K.; Bettaieb, A.; Averill-Bates, D. A., Molecular mechanisms of apoptosis activation by heat shock in multidrug-resistant Chinese hamster cells. *Radiat. Res.* **2008,** *170* (4), 498-511.

85. Manson, J.; Kumar, D.; Meenan, B. J.; Dixon, D., Polyethylene glycol functionalized gold nanoparticles: the influence of capping density on stability in various media. *Gold Bull.* **2011,** *44* (2), 99-105.

86. Rahme, K.; Chen, L.; Hobbs, R. G.; Morris, M. A.; O'Driscoll, C.; Holmes, J. D., PEGylated gold nanoparticles: polymer quantification as a function of PEG lengths and nanoparticle dimensions. *RSC Adv.* **2013,** *3* (17), 6085.

87. Szoka, F.; Olson, F.; Heath, T.; Vail, W.; Mayhew, E.; Papahadjopoulos, D., Preparation of unilamellar liposomes of intermediate size (0.1–0.2 μm) by a combination of reverse phase evaporation and extrusion through polycarbonate membranes. *Biochim. Biophys. Acta, Biomembr.* **1980,** *601*, 559-571.

88. Akbarzadeh, A.; Rezaei-Sadabady, R.; Davaran, S.; Joo, S. W.; Zarghami, N.; Hanifehpour, Y.; Samiei, M.; Kouhi, M.; Nejati-Koshki, K., Liposome: classification, preparation, and applications. *Nanoscale Res. Lett.* **2013,** *8* (1), 1-9.

89. Szoka, F.; Papahadjopoulos, D., Procedure for preparation of liposomes with large internal aqueous space and high capture by reverse-phase evaporation. *Proc. Natl. Acad. Sci. U.S.A.* **1978,** *75* (9), 4194-4198.

90. Yarmolenko, P. S.; Zhao, Y.; Landon, C.; Spasojevic, I.; Yuan, F.; Needham, D.; Viglianti, B. L.; Dewhirst, M. W., Comparative effects of thermosensitive doxorubicin-containing liposomes and hyperthermia in human and murine tumours. *Int. J. Hyperthermia* **2010,** *26* (5), 485-98.

91. Al-Jamal, W. T.; Al-Ahmady, Z. S.; Kostarelos, K., Pharmacokinetics & tissue distribution of temperature-sensitive liposomal doxorubicin in tumor-bearing mice triggered with mild hyperthermia. *Biomaterials* **2012,** *33* (18), 4608-17.

92. Park, S. M.; Kim, M. S.; Park, S. J.; Park, E. S.; Choi, K. S.; Kim, Y. S.; Kim, H. R., Novel temperature-triggered liposome with high stability: formulation, in vitro evaluation, and in vivo study combined with high-intensity focused ultrasound (HIFU). *J. Control. Release* **2013,** *170* (3), 373-9.

93. Ta, T.; Convertine, A. J.; Reyes, C. R.; Stayton, P. S.; Porter, T. M., Thermosensitive liposomes modified with poly (N-isopropylacrylamide-co-propylacrylic acid) copolymers for triggered release of doxorubicin. *Biomacromolecules* **2010,** *11* (8), 1915-1920.

94. Mayer, L. D.; Bally, M. B.; Cullis, P. R., Uptake of adriamycin into large unilamellar vesicles in response to a pH gradient. *Biochim. Biophys. Acta, Biomembr.* **1986,** *857* (1), 123-126.

95. Li, X.; Hirsh, D. J.; Cabral-Lilly, D.; Zirkel, A.; Gruner, S. M.; Janoff, A. S.; Perkins, W. R., Doxorubicin physical state in solution and inside liposomes loaded via a pH gradient. *Biochim. Biophys. Acta, Biomembr.* **1998,** *1415* (1), 23-40.

96. Mayer, L. D.; Cullis, P. R.; Bally, M. B., The use of transmembrane pH gradient-driven drug encapsulation in the pharmacodynamic evaluation of liposomal doxorubicin. *J. Liposome Res.* **1994,** *4* (1), 529-553.

97. Li, L.; ten Hagen, T. L.; Schipper, D.; Wijnberg, T. M.; van Rhoon, G. C.; Eggermont, A. M.; Lindner, L. H.; Koning, G. A., Triggered content release from optimized stealth thermosensitive liposomes using mild hyperthermia. *J. Controlled Release* **2010,** *143* (2), 274-9.

98. Jaque, D.; Martinez Maestro, L.; del Rosal, B.; Haro-Gonzalez, P.; Benayas, A.; Plaza, J. L.; Martin Rodriguez, E.; Garcia Sole, J., Nanoparticles for photothermal therapies. *Nanoscale* **2014,** *6* (16), 9494-530.

99. Hao, F.; Nehl, C. L.; Hafner, J. H.; Nordlander, P., Plasmon resonances of a gold nanostar. *Nano Lett.* **2007,** *7* (3), 729-732.

100. Pallavicini, P.; Basile, S.; Chirico, G.; Dacarro, G.; D'Alfonso, L.; Dona, A.; Patrini, M.; Falqui, A.; Sironi, L.; Taglietti, A., Monolayers of gold nanostars with two near-IR LSPRs capable of additive photothermal response. *Chem. Commun.* **2015,** *51* (65), 12928-12930.

101. Shipman, C., Evaluation of 4-(2-hydroxyethyl)-1-piperazineëthanesulfonic acid (HEPES) as a tissue culture buffer. *Proc. Soc. Exp. Biol. Med.* **1969,** *130* (1), 305-310.

102. Xie, J.; Lee, J. Y.; Wang, D. I. C., Seedless, surfactantless, high-yield synthesis of branched gold nanocrystals in HEPES buffer solution. *Chem. Mater.* **2007,** *19* (11), 2823-2830.

103. Frohlich, E., The role of surface charge in cellular uptake and cytotoxicity of medical nanoparticles. *Int. J. Nanomed.* **2012,** *7*, 5577-91.

104. Gamucci, O.; Bertero, A.; Gagliardi, M.; Bardi, G., Biomedical nanoparticles: overview of their surface immune-compatibility. *Coatings* **2014,** *4* (1), 139-159.

105. Alkilany, A. M.; Murphy, C. J., Toxicity and cellular uptake of gold nanoparticles: what we have learned so far? *J. Nanopart. Res.* **2010,** *12* (7), 2313-2333.

106. Verma, A.; Stellacci, F., Effect of surface properties on nanoparticle-cell interactions. *Small* **2010,** *6* (1), 12-21.

107. Blanco, E.; Shen, H.; Ferrari, M., Principles of nanoparticle design for overcoming biological barriers to drug delivery. *Nat. Nanotechnol.* **2015,** *33* (9), 941-51.

108. Merg, A. D.; Slocik, J.; Blaber, M. G.; Schatz, G. C.; Naik, R.; Rosi, N. L., Adjusting the metrics of 1-D helical gold nanoparticle superstructures using multivalent peptide conjugates. *Langmuir* **2015,** *31* (34), 9492-9501.

109. Yan, J.; Pan, Y.; Cheetham, A. G.; Lin, Y.-A.; Wang, W.; Cui, H.; Liu, C.-J., One-step fabrication of self-assembled peptide thin films with highly dispersed noble metal nanoparticles. *Langmuir* **2013,** *29* (52), 16051-16057.

110. Peddi, P. F.; Ellis, M. J.; Ma, C., Molecular basis of triple negative breast cancer and implications for therapy. *Int. J. Breast Cancer* **2012,** *2012*, 217185.

111. Abramson, V. G.; Lehmann, B. D.; Ballinger, T. J.; Pietenpol, J. A., Subtyping of triple-negative breast cancer: implications for therapy. *Cancer* **2015,** *121* (1), 8-16.

112. Isakoff, S. J., Triple-negative breast cancer: role of specific chemotherapy agents. *Cancer J.* **2010,** *16* (1), 53.

113. Chithrani, B. D.; Ghazani, A. A.; Chan, W. C. W., Determining the size and shape dependence of gold nanoparticle uptake into mammalian cells. *Nano Lett.* **2006,** *6* (4), 662-668.

114. Levy, R.; Shaheen, U.; Cesbron, Y.; See, V., Gold nanoparticles delivery in mammalian live cells: a critical review. *Nano reviews* **2010,** *1*.

115. Mohan, P.; Rapoport, N., Doxorubicin as a molecular nanotheranostic agent: effect of doxorubicin encapsulation in micelles or nanoemulsions on the ultrasound-mediated intracellular delivery and nuclear trafficking. *Mol. Pharmaceutics* **2010,** *7* (6), 1959-1973.

116. Tagami, T.; Foltz, W. D.; Ernsting, M. J.; Lee, C. M.; Tannock, I. F.; May, J. P.; Li, S. D., MRI monitoring of intratumoral drug delivery and prediction of the therapeutic effect with a multifunctional thermosensitive liposome. *Biomaterials* **2011,** *32* (27), 6570-8.

117. Al-Ahmady, Z. S.; Scudamore, C. L.; Kostarelos, K., Triggered doxorubicin release in solid tumors from thermosensitive liposome-peptide hybrids: Critical parameters and therapeutic efficacy. *Int. J. Cancer* **2015,** *137* (3), 731-43.

118. Gaber, M. H.; Wu, N. Z.; Hong, K.; Huang, S. K.; Dewhirst, M. W.; Papahadjopoulos, D., Thermosensitive liposomes: Extravasation and release of contents in tumor microvascular networks. *Int. J. Radiat. Oncol., Biol., Phys.* **1996,** *36* (5), 1177-1187.

119. Gewirtz, D., A critical evaluation of the mechanisms of action proposed for the antitumor effects of the anthracycline antibiotics adriamycin and daunorubicin. *Biochem. Pharmacol.* **1999,** *57* (7), 727-741.

120. Thorn, C. F.; Oshiro, C.; Marsh, S.; Hernandez-Boussard, T.; McLeod, H.; Klein, T. E.; Altman, R. B., Doxorubicin pathways: pharmacodynamics and adverse effects. *Pharmacogenetics and genomics* **2011,** *21* (7), 440-6.

121. Ahmed, K.; Zaidi, S. F., Treating cancer with heat: hyperthermia as promising strategy to enhance apoptosis. *J. Pak. Med. Assoc.* **2013,** *63* (4), 504-508.

122. Markman, J. L.; Rekechenetskiy, A.; Holler, E.; Ljubimova, J. Y., Nanomedicine therapeutic approaches to overcome cancer drug resistance. *Adv. Drug Deliv. Rev.* **2013,** *65* (13-14), 1866-79.

123. Wu, C.; Yu, C.; Chu, M., A gold nanoshell with a silica inner shell synthesized using liposome templates for doxorubicin loading and near-infrared photothermal therapy. *Int. J. Nanomed.* **2011,** *6*, 807-13.

124. Wang, X.; Han, Q.; Yu, N.; Li, J.; Yang, L.; Yang, R.; Wang, C., Aptamer-conjugated graphene oxide-gold nanocomposites for targeted chemo-photothermal therapy of cancer cells. *J. Mater. Chem. B* **2015,** *3* (19), 4036-4042.

125. Melamed, J. R.; Edelstein, R. S.; Day, E. S., Elucidating the fundamental mechanisms of cell death triggered by photothermal therapy. *ACS Nano* **2015,** *9* (1), 6-11.

126. Rock, K. L.; Kono, H., The inflammatory response to cell death. *Annu. Rev. Pathol.: Mech. Dis.* **2008,** *3*, 99-126.

127. Reagan-Shaw, S.; Nihal, M.; Ahmad, N., Dose translation from animal to human studies revisited. *FASEB J.* **2008,** *22* (3), 659-61.

128. Guidance for industry: estimating the maximum safe starting dose in initial clinical trials for therapeutics in adult healthy volunteers. http://www.fda.gov/downloads/Drugs/Guidances/UCM078932.pdf (accessed 23 March).

129. Gurney, H., Dose calculation of anticancer drugs: a review of the current practice and introduction of an alternative. *J. Clin. Oncol.* **1996,** *14* (9), 2590-2611.

130. Beatty, G. L.; Gladney, W. L., Immune escape mechanisms as a guide for cancer immunotherapy. *Clin. Cancer Res.* **2015,** *21* (4), 687-692.

131. Chen, L.; Flies, D. B., Molecular mechanisms of T cell co-stimulation and co-inhibition. *Nat. Rev. Immunol.* **2013,** *13* (4), 227-242.

132. Gajewski, T. F.; Schreiber, H.; Fu, Y.-X., Innate and adaptive immune cells in the tumor microenvironment. *Nat. Immunol.* **2013,** *14* (10), 1014-1022.

133. Bertucci, F.; Goncalves, A., Immunotherapy in breast cancer: the emerging role of PD-1 and PD-L1. *Curr. Oncol. Rep.* **2017,** *19* (10), 64.

134. Iacovelli, R.; Nole, F.; Verri, E.; Renne, G.; Paglino, C.; Santoni, M.; Cossu Rocca, M.; Giglione, P.; Aurilio, G.; Cullura, D.; Cascinu, S.; Porta, C., Prognostic role of PD-L1 expression in renal cell carcinoma. A systematic review and meta-analysis. *Target Oncol.* **2016,** *11* (2), 143-8.

135. Scheel, A. H.; Ansen, S.; Schultheis, A. M.; Scheffler, M.; Fischer, R. N.; Michels, S.; Hellmich, M.; George, J.; Zander, T.; Brockmann, M.; Stoelben, E.; Groen, H.; Timens, W.; Perner, S.; von Bergwelt-Baildon, M.; Buttner, R.; Wolf, J., PD-L1 expression in non-small cell lung cancer: correlations with genetic alterations. *Oncoimmunology* **2016,** *5* (5), e1131379.

136. Sunshine, J. C.; Nguyen, P. L.; Kaunitz, G. J.; Cottrell, T. R.; Berry, S.; Esandrio, J.; Xu, H.; Ogurtsova, A.; Bleich, K. B.; Cornish, T. C.; Lipson, E. J.; Anders, R. A.; Taube, J. M., PD-L1 expression in melanoma: a quantitative immunohistochemical antibody comparison. *Clin. Cancer Res.* **2017,** *23* (16), 4938-4944.

137. Pardoll, D. M., The blockade of immune checkpoints in cancer immunotherapy. *Nat. Rev. Cancer* **2012,** *12* (4), 252-264.

138. Postow, M. A.; Callahan, M. K.; Wolchok, J. D., Immune checkpoint blockade in cancer therapy. *J. Clin. Oncol.* **2015,** *33* (17), 1974-1982.

139. Läubli, H.; Balmelli, C.; Bossard, M.; Pfister, O.; Glatz, K.; Zippelius, A., Acute heart failure due to autoimmune myocarditis under pembrolizumab treatment for metastatic melanoma. *J. Immunother. Cancer* **2015,** *3* (1), 11.

140. Tarhini, A. A.; Zahoor, H.; Yearley, J. H.; Gibson, C.; Rahman, Z.; Dubner, R.; Rao, U. N.; Sander, C.; Kirkwood, J. M., Tumor associated PD-L1 expression pattern in microscopically tumor positive sentinel lymph nodes in patients with melanoma. *J. Transl. Med.* **2015,** *13* (1), 319.

141. Diggs, L. P.; Hsueh, E. C., Utility of PD-L1 immunohistochemistry assays for predicting PD-1/PD-L1 inhibitor response. *Biomark. Res.* **2017,** *5* (1), 12.

142. Brody, R.; Zhang, Y.; Ballas, M.; Siddiqui, M. K.; Gupta, P.; Barker, C.; Midha, A.; Walker, J., PD-L1 expression in advanced NSCLC: insights into risk stratification and treatment selection from a systematic literature review. *Lung Cancer* **2017,** *112*, 200-215.

143. Ghebeh, H.; Lehe, C.; Barhoush, E.; Al-Romaih, K.; Tulbah, A.; Al-Alwan, M.; Hendrayani, S.-F.; Manogaran, P.; Alaiya, A.; Al-Tweigeri, T.; Aboussekhra, A.; Dermime, S., Doxorubicin downregulates cell surface B7-H1 expression and upregulates its nuclear expression

in breast cancer cells: role of B7-H1 as an anti-apoptotic molecule. *Breast Cancer Res.* **2010,** *12* (4), R48.

144. Deng, L.; Liang, H.; Burnette, B.; Beckett, M.; Darga, T.; Weichselbaum, R. R.; Fu, Y. X., Irradiation and anti-PD-L1 treatment synergistically promote antitumor immunity in mice. *J. Clin. Invest.* **2014,** *124* (2), 687-95.

145. Mittendorf, E. A.; Philips, A. V.; Meric-Bernstam, F.; Qiao, N.; Wu, Y.; Harrington, S.; Su, X.; Wang, Y.; Gonzalez-Angulo, A. M.; Akcakanat, A.; Chawla, A.; Curran, M.; Hwu, P.; Sharma, P.; Litton, J. K.; Molldrem, J. J.; Alatrash, G., PD-L1 Expression in triple-negative breast cancer. *Cancer Immunol. Res.* **2014,** *2* (4), 361-370.

146. Masuda, H.; Zhang, D.; Bartholomeusz, C.; Doihara, H.; Hortobagyi, G. N.; Ueno, N. T., Role of epidermal growth factor receptor in breast cancer. *Breast Cancer Res. Treat.* **2012,** *136* (2), 331-45.

147. Tang, Y.; Fang, W.; Zhang, Y.; Hong, S.; Kang, S.; Yan, Y.; Chen, N.; Zhan, J.; He, X.; Qin, T., The association between PD-L1 and EGFR status and the prognostic value of PD-L1 in advanced non-small cell lung cancer patients treated with EGFR-TKIs. *Oncotarget* **2015,** *6* (16), 14209.

148. Li, C. W.; Lim, S. O.; Xia, W.; Lee, H. H.; Chan, L. C.; Kuo, C. W.; Khoo, K. H.; Chang, S. S.; Cha, J. H.; Kim, T.; Hsu, J. L.; Wu, Y.; Hsu, J. M.; Yamaguchi, H.; Ding, Q.; Wang, Y.; Yao, J.; Lee, C. C.; Wu, H. J.; Sahin, A. A.; Allison, J. P.; Yu, D.; Hortobagyi, G. N.; Hung, M. C., Glycosylation and stabilization of programmed death ligand-1 suppresses T-cell activity. *Nat. Commun.* **2016,** *7*, 12632.

149. Chen, N.; Fang, W.; Zhan, J.; Hong, S.; Tang, Y.; Kang, S.; Zhang, Y.; He, X.; Zhou, T.; Qin, T.; Huang, Y.; Yi, X.; Zhang, L., Upregulation of PD-L1 by EGFR activation mediates the immune escape in EGFR-driven NSCLC: implication for optional immune targeted therapy for NSCLC patients with EGFR mutation. *J. Thorac. Oncol.* **2015,** *10* (6), 910-23.

150. Lane, L. A.; Qian, X.; Nie, S., SERS nanoparticles in medicine: from label-free detection to spectroscopic tagging. *Chem. Rev.* **2015,** *115* (19), 10489-529.

151. Pallaoro, A.; Hoonejani, M. R.; Braun, G. B.; Meinhart, C. D.; Moskovits, M., Rapid identification by surface-enhanced Raman spectroscopy of cancer cells at low concentrations flowing in a microfluidic channel. *ACS Nano* **2015,** *9* (4), 4328-4336.

152. Tian, L.; Morrissey, J. J.; Kattumenu, R.; Gandra, N.; Kharasch, E. D.; Singamaneni, S., Bioplasmonic paper as a platform for detection of kidney cancer biomarkers. *Anal. Chem.* **2012,** *84* (22), 9928-9934.

153. Maiti, K. K.; Dinish, U. S.; Samanta, A.; Vendrell, M.; Soh, K.-S.; Park, S.-J.; Olivo, M.; Chang, Y.-T., Multiplex targeted in vivo cancer detection using sensitive near-infrared SERS nanotags. *Nano Today* **2012,** *7* (2), 85-93.

154. Zavaleta, C. L.; Smith, B. R.; Walton, I.; Doering, W.; Davis, G.; Shojaei, B.; Natan, M. J.; Gambhir, S. S., Multiplexed imaging of surface enhanced Raman scattering nanotags in living mice using noninvasive Raman spectroscopy. *Proc. Natl. Acad. Sci. U S A* **2009,** *106* (32), 13511-13516.

155. Dinish, U. S.; Balasundaram, G.; Chang, Y. T.; Olivo, M., Actively targeted in vivo multiplex detection of intrinsic cancer biomarkers using biocompatible SERS nanotags. *Sci .Rep.* **2014,** *4*, 4075.

156. Kircher, M. F.; de la Zerda, A.; Jokerst, J. V.; Zavaleta, C. L.; Kempen, P. J.; Mittra, E.; Pitter, K.; Huang, R.; Campos, C.; Habte, F.; Sinclair, R.; Brennan, C. W.; Mellinghoff, I. K.; Holland, E. C.; Gambhir, S. S., A brain tumor molecular imaging strategy using a new triple-modality MRI-photoacoustic-Raman nanoparticle. *Nat. Med.* **2012,** *18* (5), 829-34.

157. Jermyn, M.; Mok, K.; Mercier, J.; Desroches, J.; Pichette, J.; Saint-Arnaud, K.; Bernstein, L.; Guiot, M.-C.; Petrecca, K.; Leblond, F., Intraoperative brain cancer detection with Raman spectroscopy in humans. *Sci. Transl. Med.* **2015,** *7* (274), 274ra19-274ra19.

158. Nguyen, J. Q.; Gowani, Z. S.; O'Connor, M.; Pence, I. J.; Nguyen, T. Q.; Holt, G. E.; Schwartz, H. S.; Halpern, J. L.; Mahadevan-Jansen, A., Intraoperative Raman spectroscopy of soft tissue sarcomas. *Lasers Surg. Med.* **2016,** *48* (8), 774-781.

159. Kang, H.; Jeong, S.; Park, Y.; Yim, J.; Jun, B.-H.; Kyeong, S.; Yang, J.-K.; Kim, G.; Hong, S.; Lee, L. P.; Kim, J.-H.; Lee, H.-Y.; Jeong, D. H.; Lee, Y.-S., Near-infrared SERS nanoprobes with plasmonic Au/Ag hollow-shell assemblies for in vivo multiplex detection. *Adv. Funct. Mater.* **2013,** *23* (30), 3719-3727.

160. von Maltzahn, G.; Centrone, A.; Park, J. H.; Ramanathan, R.; Sailor, M. J.; Hatton, T. A.; Bhatia, S. N., SERS-coded gold nanorods as a multifunctional platform for densely multiplexed near-infrared imaging and photothermal heating. *Adv. Mater.* **2009,** *21* (31), 3175-3180.

161. Li, J.-L.; Wang, L.; Liu, X.-Y.; Zhang, Z.-P.; Guo, H.-C.; Liu, W.-M.; Tang, S.-H., In vitro cancer cell imaging and therapy using transferrin-conjugated gold nanoparticles. *Cancer Lett.* **2009,** *274*, 319-326.

162. Melancon, M. P.; Lu, W.; Yang, Z.; Zhang, R.; Cheng, Z.; Elliot, A. M.; Stafford, J.; Olson, T.; Zhang, J. Z.; Li, C., In vitro and in vivo targeting of hollow gold nanoshells directed at epidermal growth factor receptor for photothermal ablation therapy. *Mol. Cancer Ther.* **2008,** *7*, 1730-1739.

163. Shukla, R.; Chanda, N.; Zambre, A.; Upendran, A.; Katti, K.; Kulkarni, R. R.; Nune, S. K.; Casteel, S. W.; Smith, C. J.; Vimal, J.; Boote, E.; Robertson, J. D.; Kan, P.; Engelbrecht, H.; Watkinson, L. D.; Carmack, T. L.; Lever, J. R.; Cutler, C. S.; Caldwell, C.; Kannan, R.; Katti, K. V., Laminin receptor specific therapeutic gold nanoparticles (198AuNP-EGCg) show efficacy in treating prostate cancer. *Proc. Natl. Acad. Sci. USA* **2012,** *109*, 12426-12431.

164. Gorry, P. A., General least-squares smoothing and differentiation by the convolution (Savitzky-Golay) method. *Anal. Chem.* **1990,** *62*, 570-573.

165. Luo, J.; Ying, K.; Bai, J., Savitzky–golay smoothing and differentiation filter for even number data. *Signal Process.* **2005,** *85*, 1429-1434.

166. Savitzky, A.; Golay, M. J. E., Smoothing and differentiation of data by simplified least squares procedures. *Anal. Chem.* **1964,** *36*, 1627-1639.

167. Lieber, C. A.; Mahadevan-Jansen, A., Automated method for subtraction of fluorescence from biological Raman spectra. *Appl. Spectrosc.* **2003,** *57*, 1363-1367.

168. Ou, Y. C.; Webb, J. A.; Faley, S.; Shae, D.; Talbert, E. M.; Lin, S.; Cutright, C. C.; Wilson, J. T.; Bellan, L. M.; Bardhan, R., Gold nanoantenna-mediated photothermal drug delivery from thermosensitive liposomes in breast cancer. *ACS Omega* **2016,** *1* (2), 234-243.

169. Webb, J. A.; Ou, Y. C.; Faley, S.; Paul, E. P.; Hittinger, J. P.; Cutright, C. C.; Lin, E. C.; Bellan, L. M.; Bardhan, R., Theranostic gold nanoantennas for simultaneous multiplexed raman imaging of immunomarkers and photothermal therapy. *ACS Omega* **2017,** *2* (7), 3583-3594.

170. Petros, R. A.; DeSimone, J. M., Strategies in the design of nanoparticles for therapeutic applications. *Nat. Rev. Drug Discov.* **2010,** *9* (8), 615-627.

171. Mitra, S.; Gaur, U.; Ghosh, P.; Maitra, A., Tumour targeted delivery of encapsulated dextran–doxorubicin conjugate using chitosan nanoparticles as carrier. *J. Control. Release* **2001,** *74* (1), 317-323.

172. Wang, Y.; Polavarapu, L.; Liz-Marzán, L. M., Reduced graphene oxide-supported gold nanostars for improved SERS sensing and drug delivery. *ACS Appl. Mater. Interfaces* **2014,** *6* (24), 21798-21805.

173. Xu, P.; Jeon, S.-H.; Mack, N. H.; Doorn, S. K.; Williams, D. J.; Han, X.; Wang, H.-L., Field-assisted synthesis of SERS-active silver nanoparticles using conducting polymers. *Nanoscale* **2010,** *2*, 1436-1440.

174. Wang, C.; Xu, J.; Wang, J.; Rong, Z.; Li, P.; Xiao, R.; Wang, S., Polyethylenimine-interlayered silver-shell magnetic-core microspheres as multifunctional SERS substrates. *J. Mater. Chem. C* **2015,** *3*, 8684-8693.

175. Movasaghi, Z.; Rehman, S.; Rehman, I. U., Raman spectroscopy of biological tissues. *Appl. Spectrosc. Rev.* **2007,** *42*, 493-541.

176. Liu, Y.; Ashton, J. R.; Moding, E. J.; Yuan, H.; Register, J. K.; Fales, A. M.; Choi, J.; Whitley, M. J.; Zhao, X.; Qi, Y.; Ma, Y.; Vaidyanathan, G.; Zalutsky, M. R.; Kirsch, D. G.; Badea, C. T.; Vo-Dinh, T., A plasmonic gold nanostar theranostic probe for in vivo tumor imaging and photothermal therapy. *Theranostics* **2015,** *5* (9), 946-60.

177. O'Brien, C. M.; Herington, J. L.; Brown, N.; Pence, I. J.; Paria, B. C.; Slaughter, J. C.; Reese, J.; Mahadevan-Jansen, A., In vivo Raman spectral analysis of impaired cervical remodeling in a mouse model of delayed parturition. *Sci. Rep.* **2017,** *7* (1), 6835.

178. Pence, I. J.; Beaulieu, D. B.; Horst, S. N.; Bi, X.; Herline, A. J.; Schwartz, D. A.; Mahadevan-Jansen, A., Clinical characterization of in vivo inflammatory bowel disease with Raman spectroscopy. *Biomed. Opt. Express* **2017,** *8* (2), 524-535.

179. Bardhan, R.; Chen, W.; Bartels, M.; Perez-Torres, C.; Botero, M. F.; McAninch, R. W.; Contreras, A.; Schiff, R.; Pautler, R. G.; Halas, N. J.; Joshi, A., Tracking of multimodal therapeutic nanocomplexes targeting breast cancer in vivo. *Nano Lett.* **2010,** *10* (12), 4920-4928.

180. Chen, W.; Ayala-Orozco, C.; Biswal, N. C.; Perez-Torres, C.; Bartels, M.; Bardhan, R.; Stinnet, G.; Liu, X.-D.; Ji, B.; Deorukhkar, A., Targeting pancreatic cancer with magneto-fluorescent theranostic gold nanoshells. *Nanomedicine* **2014,** *9* (8), 1209-1222.

181. Heskamp, S.; Hobo, W.; Molkenboer-Kuenen, J. D.; Olive, D.; Oyen, W. J.; Dolstra, H.; Boerman, O. C., Noninvasive imaging of tumor PD-L1 expression using radiolabeled anti-PD-L1 antibodies. *Cancer research* **2015,** *75* (14), 2928-36.

182. Tavare, R.; Escuin-Ordinas, H.; Mok, S.; McCracken, M. N.; Zettlitz, K. A.; Salazar, F. B.; Witte, O. N.; Ribas, A.; Wu, A. M., An effective immuno-PET imaging method to monitor CD8-dependent responses to immunotherapy. *Cancer research* **2016,** *76* (1), 73-82.

183. Kobayashi, H.; Watanabe, R.; Choyke, P. L., Improving conventional enhanced permeability and retention (EPR) effects; shat is the appropriate target? *Theranostics* **2013,** *4* (1), 81-9.

184. Miao, L.; Huang, L., Exploring the tumor microenvironment with nanoparticles. In *Nanotechnology-Based Precision Tools for the Detection and Treatment of Cancer*, Mirkin, C. A.; Meade, T. J.; Petrosko, S. H.; Stegh, A. H., Eds. Springer International Publishing: Cham, 2015; pp 193-226.

185. England, C. G.; Gobin, A. M.; Frieboes, H. B., Evaluation of uptake and distribution of gold nanoparticles in solid tumors. *Eur. Phys. J. Plus* **2015,** *130* (11).

186. Khlebtsov, N.; Dykman, L., Biodistribution and toxicity of engineered gold nanoparticles: a review of in vitro and in vivo studies. *Chem. Soc. Rev.* **2011,** *40* (3), 1647-71.

187. Sonavane, G.; Tomoda, K.; Makino, K., Biodistribution of colloidal gold nanoparticles after intravenous administration: effect of particle Size. *Colloids Surf. B Biointerfaces* **2008,** *66* (2), 274-80.

188. De Jong, W. H.; Hagens, W. I.; Krystek, P.; Burger, M. C.; Sips, A. J.; Geertsma, R. E., Particle size-dependent organ distribution of gold nanoparticles after intravenous administration. *Biomaterials* **2008,** *29* (12), 1912-9.

189. Gustafson, H. H.; Holt-Casper, D.; Grainger, D. W.; Ghandehari, H., Nanoparticle uptake: the phagocyte problem. *Nano Today* **2015,** *10* (4), 487-510.

190. Blanco, E.; Shen, H.; Ferrari, M., Principles of nanoparticle design for overcoming biological barriers to drug delivery. *Nat. Biotechnol.* **2015,** *33* (9), 941-51.

191. Oh, N.; Park, J.-H., Surface chemistry of gold nanoparticles mediates their exocytosis in macrophages. *ACS Nano* **2014,** *8* (6), 6232-6241.

192. Liu, J.; Yu, M.; Zhou, C.; Zheng, J., Renal clearable inorganic nanoparticles: a new frontier of bionanotechnology. *Mater. Today* **2013,** *16* (12), 477-486.

193. Choi, H. S.; Liu, W.; Misra, P.; Tanaka, E.; Zimmer, J. P.; Itty Ipe, B.; Bawendi, M. G.; Frangioni, J. V., Renal clearance of quantum dots. *Nat. Biotechnol.* **2007,** *25* (10), 1165-70.

194. Davis, M. E.; Chen, Z. G.; Shin, D. M., Nanoparticle therapeutics: an emerging treatment modality for cancer. *Nat. Rev. Drug Discov.* **2008,** *7* (9), 771-82.

195. Choi, C. H. J.; Zuckerman, J. E.; Webster, P.; Davis, M. E., Targeting kidney mesangium by nanoparticles of defined size. *Proc. Natl. Acad. Sci. U S A* **2011,** *108* (16), 6656-6661.

196. Huang, X.; Li, L.; Liu, T.; Hao, N.; Liu, H.; Chen, D.; Tang, F., The shape effect of mesoporous silica nanoparticles on biodistribution, clearance, and biocompatibility in vivo. *ACS Nano* **2011,** *5* (7), 5390-5399.

197. Toy, R.; Peiris, P. M.; Ghaghada, K. B.; Karathanasis, E., Shaping cancer nanomedicine: the effect of particle shape on the in vivo journey of nanoparticles. *Nanomedicine* **2014,** *9* (1), 121-34.

198. Arnida; Janat-Amsbury, M. M.; Ray, A.; Peterson, C. M.; Ghandehari, H., Geometry and surface characteristics of gold nanoparticles influence their biodistribution and uptake by macrophages. *Eur. J. Pharm. Biopharm.* **2011,** *77* (3), 417-23.

199. Wiegand, S.; Heinen, T.; Ramaswamy, A.; Sesterhenn, A. M.; Bergemann, C.; Werner, J. A.; Lubbe, A. S., Evaluation of the tolerance and distribution of intravenously applied ferrofluid particles of 250 and 500 nm size in an animal model. *J. Drug Target.* **2009,** *17* (3), 194-9.

200. Gatti, A. M.; Rivasi, F., Biocompatibility of micro-and nanoparticles. Part I: in liver and kidney. *Biomaterials* **2002,** *23* (11), 2381-2387.

201. Kang, B.; Kukreja, A.; Song, D.; Huh, Y.-M.; Haam, S., Strategies for using nanoprobes to perceive and treat cancer activity: a review. *J. Bio. Eng.* **2017,** *11(13)*, 1-12.

202. Rejman, J.; Oberle, V.; Zuhorn, I. S.; Hoekstra, D., Size-dependent internalization of particles via the pathways of clathrin-and caveolae-mediated endocytosis. *Biochem. J.* **2004,** *377*, 159-169.

203. Wang, A. Z.; Langer, R.; Farokhzad, O. C., Nanoparticle Delivery of Cancer Drugs. *Annu. Rev. Med.* **2012,** *63*, 185-198.

204. Sadauskas, E.; Wallin, H.; Stoltenberg, M.; Vogel, U.; Doering, P.; Larsen, A.; Danscher, G., Kupffer cells are central in the removal of nanoparticles from the organism. *Part. Fibre. Toxicol.* **2007,** *4*, 10.

205. Jong, W. H. D.; Burger, M. C.; Verheijen, M. A.; Geertsma, R. E., Detection of the presence of gold nanoparticles in organs by transmission electron microscopy. *Materials* **2010,** *3* (9), 4681-4694.

206. MacParland, S. A.; Tsoi, K. M.; Ouyang, B.; Ma, X.-Z.; Manuel, J.; Fawaz, A.; Ostrowski, M. A.; Alman, B. A.; Zilman, A.; Chan, W. C. W.; McGilvray, I. D., Phenotype determines nanoparticle uptake by human macrophages from liver and blood. *ACS Nano* **2017,** *11* (3), 2428-2443.

207. Tsoi, K. M.; MacParland, S. A.; Ma, X. Z.; Spetzler, V. N.; Echeverri, J.; Ouyang, B.; Fadel, S. M.; Sykes, E. A.; Goldaracena, N.; Kaths, J. M.; Conneely, J. B.; Alman, B. A.; Selzner, M.; Ostrowski, M. A.; Adeyi, O. A.; Zilman, A.; McGilvray, I. D.; Chan, W. C., Mechanism of hard-nanomaterial clearance by the liver. *Nat. Mater.* **2016,** *15* (11), 1212-1221.

208. Dykman, L. A.; Khlebtsov, N. G., Immunological properties of gold nanoparticles. *Chem. Sci.* **2017,** *8* (3), 1719-1735.

209. Huo, S.; Ma, H.; Huang, K.; Liu, J.; Wei, T.; Jin, S.; Zhang, J.; He, S.; Liang, X. J., Superior penetration and retention behavior of 50 nm gold nanoparticles in tumors. *Cancer research* **2013,** *73* (1), 319-30.

210. Yang, C.; Tian, A.; Li, Z., Reversible cardiac hypertrophy induced by PEG-coated gold nanoparticles in mice. *Sci. Rep.* **2016,** *6*, 20203.

211. Barua, S.; Mitragotri, S., Challenges associated with penetration of nanoparticles across cell and tissue barriers: a review of current status and future prospects. *Nano Today* **2014,** *9* (2), 223-243.

212. Zhang, P.; Chiu, Y.-C.; Tostanoski, L. H.; Jewell, C. M., Polyelectrolyte multilayers assembled entirely from immune signals on gold nanoparticle templates promote sntigen-specific T Cell response. *ACS Nano* **2015,** *9* (6), 6465-6477.

213. Tumeh, P. C.; Harview, C. L.; Yearley, J. H.; Shintaku, I. P.; Taylor, E. J.; Robert, L.; Chmielowski, B.; Spasic, M.; Henry, G.; Ciobanu, V.; West, A. N.; Carmona, M.; Kivork, C.; Seja, E.; Cherry, G.; Gutierrez, A. J.; Grogan, T. R.; Mateus, C.; Tomasic, G.; Glaspy, J. A.; Emerson, R. O.; Robins, H.; Pierce, R. H.; Elashoff, D. A.; Robert, C.; Ribas, A., PD-1 blockade induces responses by inhibiting adaptive immune resistance. *Nature* **2014,** *515* (7528), 568-71.

214. Jenkins, R. W.; Barbie, D. A.; Flaherty, K. T., Mechanisms of resistance to immune checkpoint inhibitors. *Br. J. Cancer* **2018,** *118* (1), 9-16.

215. Vonderheide, R. H.; Domchek, S. M.; Clark, A. S., Immunotherapy for breast cancer: what are we missing? *Clin. Cancer Res.* **2017,** *23* (11), 2640-2646.

216. Califano, R.; Lal, R.; Lewanski, C.; Nicolson, M. C.; Ottensmeier, C. H.; Popat, S.; Hodgson, M.; Postmus, P. E., Patient selection for anti-PD-1/PD-L1 therapy in advanced non-small-cell lung cancer: implications for clinical practice. *Future Oncol.* **2018,** *14* (23), 2415-2431.

217. McLaughlin, J.; Han, G.; Schalper, K. A.; Carvajal-Hausdorf, D.; Pelekanou, V.; Rehman, J.; Velcheti, V.; Herbst, R.; LoRusso, P.; Rimm, D. L., Quantitative assessment of the heterogeneity of PD-L1 expression in non-amall-cell lung cancer. *JAMA Oncol.* **2016,** *2* (1), 46-54.

218. Gniadek, T. J.; Li, Q. K.; Tully, E.; Chatterjee, S.; Nimmagadda, S.; Gabrielson, E., Heterogeneous expression of PD-L1 in pulmonary squamous cell carcinoma and adenocarcinoma: implications for assessment by small biopsy. *Mod. Pathol.* **2017,** *30* (4), 530-538.

219. Munari, E.; Zamboni, G.; Marconi, M.; Sommaggio, M.; Brunelli, M.; Martignoni, G.; Netto, G. J.; Moretta, F.; Mingari, M. C.; Salgarello, M., PD-L1 expression heterogeneity in non-small cell lung cancer: evaluation of small biopsies reliability. *Oncotarget* **2017,** *8* (52), 90123.

220. Guldbrandsen, K. F.; Hendel, H. W.; Langer, S. W.; Fischer, B. M., Nuclear molecular imaging strategies in immune checkpoint inhibitor therapy. *Diagnostics* **2017,** *7* (2).

221. Nishino, M.; Ramaiya, N. H.; Hatabu, H.; Hodi, F. S., Monitoring immune-checkpoint blockade: response evaluation and biomarker development. *Nat. Rev. Clin. Oncol.* **2017,** *14* (11), 655-668.

222. Broos, K.; Lecocq, Q.; Raes, G.; Devoogdt, N.; Keyaerts, M.; Breckpot, K., Noninvasive imaging of the PD-1:PD-L1 immune checkpoint: embracing nuclear medicine for the benefit of personalized immunotherapy. *Theranostics* **2018,** *8* (13), 3559-3570.

223. Hadrup, S.; Donia, M.; Thor Straten, P., Effector CD4 and CD8 T cells and their role in the tumor microenvironment. *Cancer Microenviron.* **2013,** *6* (2), 123-33.

224. Durgeau, A.; Virk, Y.; Corgnac, S.; Mami-Chouaib, F., Recent advances in targeting CD8 T-cell immunity for more effective cancer immunotherapy. *Front. Immunol.* **2018,** *9*, 14-14.

225. Reiser, J.; Banerjee, A., Effector, memory, and dysfunctional CD8+ T cell fates in the antitumor immune response. *J. Immunol. Res.* **2016,** *2016*, 14.

226. Huang, A. C.; Postow, M. A.; Orlowski, R. J.; Mick, R.; Bengsch, B.; Sasikanth Manne; Xu, W.; Harmon, S.; Giles, J. R.; Wenz, B.; Adamow, M.; Kuk, D.; Panageas, K. S.; Carrera, C.; Wong, P.; Quagliarello, F.; Wubbenhorst, B.; D'Andrea, K.; Pauken, K. E.; Herati, R. S.; Staupe, R. P.; Schenkel, J. M.; McGettigan, S.; Kothari, S.; George, S. M.; Vonderheide, R. H.; Amaravadi, R. K.; Karakousis, G. C.; Schuchter, L. M.; Xu, X.; Nathanson, K. L.; Wolchok, J. D.; Gangadhar, T. C.; Wherry, E. J., T-cell invigoration to tumour burden ratio associated with anti-PD-1 response. *Nature* **2017,** *545*, 60-65.

227. Moreno, B. H.; Zaretsky, J. M.; Garcia-Diaz, A.; Tsoi, J.; Parisi, G.; Robert, L.; Meeth, K.; Ndoye, A.; Bosenberg, M.; T.Weeraratna, A.; Graeber, T. G.; Comin-Anduix, B.; Hu-Lieskovan, S.; Ribas, A., Response to Programmed Cell Death-1 Blockade in a Murine Melanoma Syngeneic Model Requires Costimulation, CD4, and CD8 T Cells. *Cancer Immunol. Res.* **2016,** *4*, 845-857.

228. Ou, Y. C.; Webb, J. A.; O'Brien, C. M.; Pence, I. J.; Lin, E. C.; Paul, E. P.; Cole, D.; Ou, S. H.; Lapierre-Landry, M.; DeLapp, R. C.; Lippmann, E. S.; Mahadevan-Jansen, A.; Bardhan, R., Diagnosis of immunomarkers in vivo via multiplexed surface enhanced Raman spectroscopy with gold nanostars. *Nanoscale* **2018,** *10* (27), 13092-13105.

229. Liu, J.; Blake, S. J.; Yong, M. C. R.; Harjunpää, H.; Ngiow, S. F.; Takeda, K.; Arabella Young; O'Donnell, J. S.; Allen, S.; Smyth, M. J.; Teng, M. W. L., Improved Efficacy of Neoadjuvant Compared to Adjuvant Immunotherapy to Eradicate Metastatic Disease. *Cancer Discov.* **2016,** *6*, 1382-1399.

230. Yonezawa, A.; Dutt, S.; Chester, C.; Kim, J.; Kohrt, H. E., Boosting Cancer Immunotherapy with Anti-CD137 Antibody Therapy. *Clin. Cancer Res.* **2015,** *21*, 3113-3120.

231. Kobayashi, H.; Watanabe, R.; Choyke, P. L., Improving conventional enhanced permeability and retention (EPR) dffects; what is the appropriate target? *Theranostics* **2013,** *4* (1), 81-9.

232. Farist, F.; Thornileyt, M.; Wickramasinghet, Y.; Houstont, R.; Rolfet, P.; Livers, N.; Spencer, A., Non-invasive in vivo near-infrared optical measurement of the penetration depth in the neonatal head. *Clin. Phys. Physiol. Meas.* **1991,** *12*, 353-358.

233. Henderson, T. A.; Morries, L. D., Near-infrared photonic energy penetration: can infrared phototherapy effectively reach the human brain? *Neuropsychiatric Disease Treat.* **2015,** *11*, 2191-2208.

234. Ku, G.; Wang, L. V., Deeply penetrating photoacoustic tomography in biological tissues enhanced with an optical contrast agent. *Optics Letters* **2005,** *30*, 507-509.

235. Meeth, K.; Wang, J. X.; Micevic, G.; Damsky, W.; Bosenberg, M. W., The YUMM lines: a series of congenic mouse melanoma cell lines with defined genetic alterations. *Pigment Cell Melanoma Res.* **2016,** *29* (5), 590-7.

236. Wang, J.; Bai, R.; Yang, R.; Liu, J.; Tang, J.; Liu, Y.; Li, J.; Chai, Z.; Chen, C., Size- and surface chemistry-dependent pharmacokinetics and tumor accumulation of engineered gold nanoparticles after intravenous administration. *Metallomics* **2015,** *7* (3), 516-24.

237. Yang, L.; Kuang, H.; Zhang, W.; Aguilar, Z. P.; Wei, H.; Xu, H., Comparisons of the biodistribution and toxicological examinations after repeated intravenous administration of silver and gold nanoparticles in mice. *Sci. Rep.* **2017,** *7* (1), 3303.

238. Lieber, C. A.; Majumder, S. K.; Ellis, D. L.; Billheimer, D. D.; Mahadevan-Jansen, A., In vivo nonmelanoma skin cancer diagnosis using Raman microspectroscopy. *Lasers Surg. Med.* **2008,** *40* (7), 461-7.

239. Makkouk, A.; Chester, C.; Kohrt, H. E., Rationale for anti-CD137 cancer immunotherapy. *Eur. J. Cancer* **2016,** *54*, 112-119.

240. Perez-Ruiz, E.; Etxeberria, I.; Rodriguez-Ruiz, M. E.; Melero, I., Anti-CD137 and PD-1/PD-L1 antibodies en route toward clinical synergy. *Clin. Cancer Res.* **2017,** *23* (18), 5326-5328.

241. Kang, H.; Jeong, S.; Koh, Y.; Geun Cha, M.; Yang, J.-K.; Kyeong, S.; Kim, J.; Kwak, S.-Y.; Chang, H.-J.; Lee, H.; Jeong, C.; Kim, J.-H.; Jun, B.-H.; Kim, Y.-K.; Hong Jeong, D.; Lee, Y.-S., Corrigendum: direct identification of on-bead peptides using surface-enhanced raman spectroscopic barcoding system for high-throughput bioanalysis. *Sci. Rep.* **2015,** *5* (1).

242. Kong, K.; Kendall, C.; Stone, N.; Notingher, I., Raman spectroscopy for medical diagnostics--From in-vitro biofluid assays to in-vivo cancer detection. *Adv. Drug. Deliv. Rev.* **2015,** *89*, 121-34.

243. Jokinen, E.; Koivunen, J. P., MEK and PI3K inhibition in solid tumors: rationale and evidence to date. *Ther. Adv. Med. Oncol.* **2015,** *7* (3), 170-180.

244. Cheng, Y.; Tian, H., Current development status of MEK inhibitors. *Molecules* **2017,** *22* (10).

245. Kuske, M.; Westphal, D.; Wehner, R.; Schmitz, M.; Beissert, S.; Praetorius, C.; Meier, F., Immunomodulatory effects of BRAF and MEK inhibitors: Implications for Melanoma therapy. *Pharmacol. Res.* **2018,** *136*, 151-159.

246. Chiou, V. L.; Burotto, M., Pseudoprogression and immune-related response in solid tumors. *J. Clin. Oncol.* **2015,** *33* (31), 3541-3543.

247. Hobro, A. J.; Kumagai, Y.; Akira, S.; Smith, N. I., Raman spectroscopy as a tool for label-free lymphocyte cell line discrimination. *Analyst* **2016,** *141* (12), 3756-64.

248. Ichimura, T.; Chiu, L. D.; Fujita, K.; Machiyama, H.; Yamaguchi, T.; Watanabe, T. M.; Fujita, H., Non-label immune cell state prediction using Raman spectroscopy. *Sci. Rep.* **2016,** *6*, 37562.

249. Talari, A. C. S.; Evans, C. A.; Holen, I.; Coleman, R. E.; Rehman, I. U., Raman spectroscopic analysis differentiates between breast cancer cell lines. *J. Raman Spectrosc.* **2015,** *46* (5), 421-427.

250. Kann, B.; Offerhaus, H. L.; Windbergs, M.; Otto, C., Raman microscopy for cellular investigations--From single cell imaging to drug carrier uptake visualization. *Adv. Drug Deliv. Rev.* **2015,** *89*, 71-90.

251. Okada, M.; Smith, N. I.; Palonpon, A. F.; Endo, H.; Kawata, S.; Sodeoka, M.; Fujita, K., Label-free Raman observation of cytochrome c dynamics during apoptosis. *Proc. Natl. Acad. Sci. U S A* **2012,** *109* (1), 28-32.

252. Hollon, T.; Lewis, S.; Freudiger, C. W.; Sunney Xie, X.; Orringer, D. A., Improving the accuracy of brain tumor surgery via Raman-based technology. *Neurosurg. Focus* **2016,** *40* (3), E9.